# Beryllium-Uranium System[1]

R. W. Buzzard

The phase diagram of the system beryllium-uranium was constructed from data obtained by thermal analysis, metallographic examination and X-ray diffraction. The system is characterized by one intermetallic compound, $UBe_{13}$, melting at about 2,000° C, a eutectic having a composition of approximately 0.12 weight percent of beryllium, occurring between uranium and $UBe_{13}$, at 1,090° C, and a monotectic occurring at 1,550° C and 60-weight-percent of beryllium. The solid solubility of beryllium in uranium is slight; no solid solubility of uranium in beryllium was detected. The transformation temperatures of uranium are not affected by additions of beryllium.

## 1. Introduction

The literature contains very little data on the beryllium-uranium system. This lack of information can be ascribed to the technical difficulties resulting from the high vapor pressure of beryllium and the large difference in the densities of the two components. A tentative phase diagram of the beryllium-uranium system was presented in the literature review by Buzzard and Cleaves.[2] The diagram shows one compound, approximating $UBe_9$ in composition and two eutectics, one at 1,060° C between gamma uranium and $UBe_9$, and the other at 1,200° to 1,250° C between beryllium and U $Be_9$.

In order to have available a more accurate diagram of the beryllium-uranium system, work was initiated at the National Bureau of Standards at the request of the Atomic Energy Commission. A series of beryllium-uranium alloys was prepared with compositions ranging from 0- to 100-percent beryllium and analyzed metallographically, by X-ray diffraction, and by thermal analysis.

## 2. Preparation of Alloys

### 2.1. Stock materials, apparatus, and procedures

The stock materials consisting of extruded beryllium and uranium were obtained from the Atomic Energy Commission. The alloys were prepared in a specially constructed, high-frequency induction furnace, in which the charges could be melted and the ingots poured in an atmosphere of purified helium. This was accomplished by enclosing the beryllia crucible and mold assemblies in a silica tube and by using bottom-pour crucibles. Details of the construction are shown schematically in figure 1. It is important that the beryllia be fired at approximately 1,900° C and be of high purity. The pouring temperatures were determined by sighting through the "sight" tube on the bottom of the stopper with an optical pyrometer. The stopper was essentially a closed end beryllia tube.

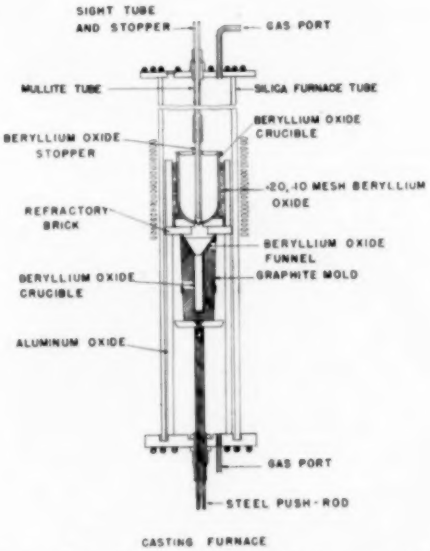


FIGURE 1. *Controlled atmosphere, high frequency induction furnace.*

### 2.2. Segregation

The density of the beryllium-uranium compound was considerably greater than the beryllium-rich liquid phase, thereby creating a tendency for the compound to collect at the bottom of the crucible or mold as it precipitated from the cooling liquid. This settling-out tendency was not so pronounced in the uranium-rich phase. It was possible to prepare beryllium-rich alloys reasonably free of segregation by pouring the ingots with the power on full into a cold mold of small cross section. The large supply of power, immediately before pouring, caused a vigorous stirring action, which kept the compound uniformly distributed.

The distribution of uranium in the ingots in the "as cast condition" was checked both by chemical analysis (table 1) and microradiographic examination (figs. 2 and 3). Chemical analysis of the ingots

[1] Investigation sponsored by the Atomic Energy Commission at the National Bureau of Standards.

[2] R. W. Buzzard and H. E. Cleaves; Issue No. 1, p. 26-27, Journal Metallurgy and Ceramics (TID 65), July 1948.

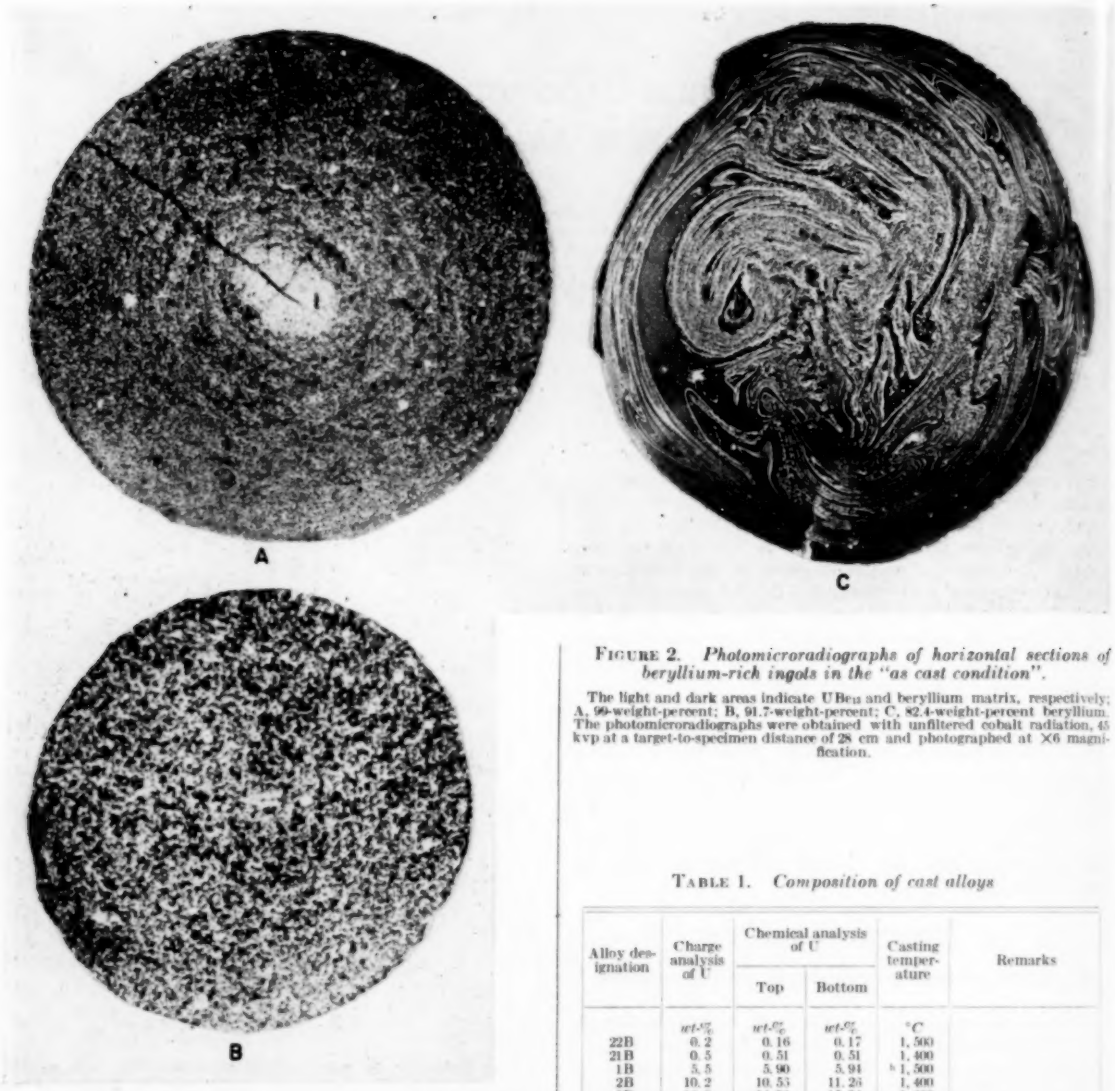


FIGURE 2. *Photomicroradiographs of horizontal sections of beryllium-rich ingots in the "as cast condition".*

The light and dark areas indicate $UBe_{13}$ and beryllium matrix, respectively; A, 99-weight-percent; B, 91.7-weight-percent; C, 82.4-weight-percent beryllium. The photomicroradiographs were obtained with unfiltered cobalt radiation, 45 kvp at a target-to-specimen distance of 28 cm and photographed at ×6 magnification.

showed satisfactory uniformity of composition from top to bottom, with the exception that the ingot in the 50-weight-percent range had a deviation of 5 percent over its length. The variation from top to bottom in the other ingots was within 1 percent, and the ingots having compositions in the high-uranium and high-beryllium fields showed little deviation in composition from top to bottom. The microradiographs showed good distribution of the compound in the beryllium-rich ingots, with the exception of the 99-weight-percent beryllium ingot. The swirl distribution of the compound shown in the photomicroradiograph (fig. 2, A) is caused by the pouring action and is apparent in this ingot because of the low concentration of the compound.

TABLE 1. *Composition of cast alloys*

| Alloy designation | Charge analysis of U | Chemical analysis of U | | Casting temperature | Remarks |
|---|---|---|---|---|---|
| | | Top | Bottom | | |
| | *wt-%* | *wt-%* | *wt-%* | *°C* | |
| 22B | 0.2 | 0.16 | 0.17 | 1,500 | |
| 21B | 0.5 | 0.51 | 0.51 | 1,400 | |
| 1B | 5.5 | 5.90 | 5.94 | [b] 1,500 | |
| 2B | 10.2 | 10.55 | 11.26 | 1,400 | |
| 3B | 14.8 | 14.94 | 15.34 | 1,400 | |
| 16B | 19.0 | 19.45 | 20.25 | [b] 1,425 | |
| 5B | 30.0 | 30.50 | 30.17 | [b] 1,900 | |
| 6B | 40.0 | 43.03 | 42.29 | [b] 1,850 | |
| 7B | 50.0 | 44.02 | 49.68 | [b] 1,910 | |
| 8B | 65.0 | 64.56 | 65.21 | [b] 2,020 | Did not pour at 1,950° C. |
| 17B | 73.5 | 73.06 | 73.86 | [b] 2,000 | |
| 9B | 75.6 | 76.43 | 75.9 | [b] 1,900 | 1,900° C too low for good casting. |
| 18B | 77.0 | 77.54 | 76.70 | [b] 2,030 | |
| 15 | 85.0 | 85.22 | 85.32 | [b] 1,920 | |
| 10B | 95.0 | [a] 94.85<br>[b] 94.07 | [a] 94.57<br>[b] 93.70 | [b] 1,925 | |
| 11B | 99.0 | [a] 98.72<br>[b] 98.70 | [a] 99.22<br>[b] 98.60 | [b] 1,650 | |
| 12B | 99.8 | [a] 99.80<br>[b] 99.84 | [a] 99.63<br>[b] 99.82 | 1,400 | |
| 14B | 99.95 | [a] 99.85<br>[b] 99.91 | [a] 99.86<br>[b] 99.91 | 1,400 | |
| 13B | 99.6 | [a] 99.89<br>[b] 99.94 | [a] 99.85<br>[b] 99.93 | 1,410 | |

[a] Wet chemical analysis for U.
[b] Graphite heater around crucible.
[b] Spectrographic analysis of Be, U by difference.

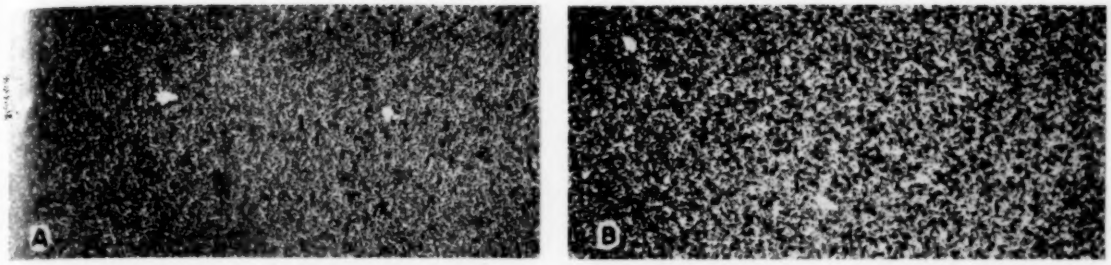


FIGURE 3. *Photomicroradiographs of vertical sections of beryllium-rich ingots in the "as cast condition".*

A, 82.4-weight-percent and B, 91.7-weight-percent beryllium ×6 magnification.

## 3. Thermal-Analysis Apparatus and Procedure

The solid-phase arrests were determined by time-temperature analysis, using a modification of the apparatus described by Teitel and Cohen.[3] The accessory apparatus included a Brown Air-o-line program controller to maintain uniform heating and cooling rates. A furnace atmosphere of purified argon was used in order to minimize the evaporation of beryllium. Arrests with this equipment could be determined with an accuracy of ±2 deg C.

For regions involving a liquid phase, the high-frequency induction furnace used to prepare the cast alloys was modified for thermal analysis by substituting a tapered crucible for the bottom-pour-casting crucible. A beryllia plug was inserted in the stopper tube to a height such that temperature observations were made at the center of the melt, using a high precision optical pyrometer. The cooling rates were controlled by manually reducing the power of the convertor at a uniform rate in a manner that cooling rates of the order 0.5 to 2.0 deg/min were obtained through the thermal arrests. The solidus and solid-phase arrests of the beryllium-rich alloys were determined in this furnace, using platinum-rhodium thermocouples enclosed in high-fired-alumina protection tubes and inserted through the sight tubes. The tip of the couple was seated on the top of the beryllia plug. The convertor control was modified so that the power could be reduced mechanically with an electric motor operating through a gear box. The time-temperature curves were recorded on a Brown electronic recorder.

## 4. Results

### 4.1. Beryllium-uranium compound

Metallographic examination showed all of the cast alloys (table 1) to consist of two phases. One phase increased in amount from either the uranium or beryllium end of the system until at approximately 35-weight-percent beryllium, the alloy appeared to be composed almost entirely of this phase (fig. 4, E, F). Alloys in this range were hard and very brittle. It was found that this phase could be readily isolated from a uranium matrix by electrolytically dissolving the uranium in a 10-percent chromic-acid solution. The separated phase was identified as the intermetallic compound $UBe_{13}$ having a cubic structure, as reported by Baenziger and Rundle.[4] Precision determination of the lattice constant gave a value of $a=2\times5.1849$. ±0.0001 Å at 27° C.

In order to check the stoichiometric formula, $UBe_{13}$, a density determination and chemical analysis were made. The values obtained were 4.420±0.002 g/cm³ at 26° C and 32.15 ±0.05-weight-percent beryllium as compared to the computed values of 4.373 g/cm³ and 33.0-weight-percent beryllium. The actual and computed values are in sufficient agreement to conclude that the formula is $UBe_{13}$ and not $UBe_9$ as previously reported. The thermal-analysis results indicate that the melting point of $UBe_{13}$ was approximately 2,000° C.

### 4.2. Beryllium-rich alloys

Data (table 2) from the time-temperature cooling curves obtained for the beryllium-rich alloys show a monotectic at 60-weight-percent beryllium and 1,550° C (fig. 5). The liquidus and liquid solubility temperatures above 1,600° C were influenced by the vapor phase of the beryllium, and the accuracy is not greater than ±25 deg C. The maximum temperature indicated for the $UBe_{13}$ composition is a selected value based on an evaluation of the thermal data, casting temperatures, and extrapolation of the liquidus curve. The solidus (1,280° C ±3°) coincided with the melting point of beryllium at 1,283° C. A pronounced arrest occurred below the solidus at 1,250° C ±10°, which can be ascribed either to impurities or an allotropic transformation in the beryllium phase, although the strong arrests observed at this point indicate a possibility of the latter. Previous investigators [2, 5, 6, 7] have observed similar double points in the melting-point determinations of beryllium and have concluded impurities to be the cause, but lacking conclusive proof as to the cause of the observed double arrest, the line is dotted on the diagram.

[3] R. J. Teitel and Morris Cohen, Trans. Am. Inst. Mining Met. Engrs. **185** 285-296 (1949).

[4] N. C. Baenziger and R. E. Rundle, United States Atomic Energy Commission, AECD-2506 (April 8, 1949).

[5] G. Oesterheld, Z. anorg. u allgem. Chem. **97** 1-6 (1916).

[6] L. Losano, Alluminio **8** 67 (1939).

[7] H. A. Sloman, J. Inst. Metals **49** 365 (1932).

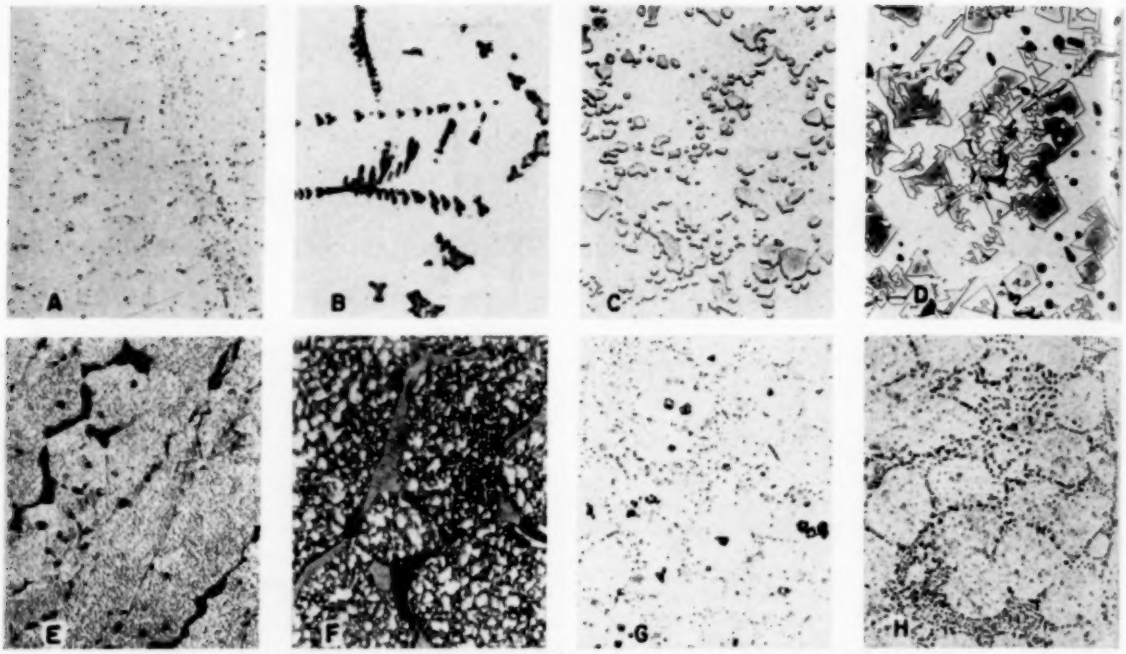


FIGURE 4. *Typical microstructures of beryllium-uranium alloys in the "as cast condition".*

Etchant 5 percent HF, A, B, C, D, E, G, and H at ×100, F at ×500. A, 99.49-weight-percent beryllium; B, 98.86-weight-percent beryllium; C, 80.15-weight-percent beryllium; D, 69.7-weight-percent beryllium, dark constituent, $UBe_{13}$, in light matrix of beryllium; E and F, 35.1-weight-percent beryllium, dark areas at low magnification are shown at high magnification to be beryllium (pale grey) and the mottled background is $UBe_{13}$; G, 0.17-weight-percent beryllium, small angular areas, sharply outlined, are $UBe_{13}$ particles; H, 0.09-weight-percent beryllium. The uranium-$UBe_{13}$ eutectic is shown in an uranium matrix.

TABLE 2. *Summary of thermal data obtained for beryllium-rich alloys*

| Be | Thermal arrests [a] | | | | |
|---|---|---|---|---|---|
| | Miscibility of $L_1+L_2$ | Liquidus | $L_1+\delta \rightarrow L_2+\delta$ | Solidus | $\epsilon+\delta \rightarrow \eta+\delta$ |
| wt-% | °C | °C | °C | °C | °C |
| 100 | ..... | [b] 1,282<br>1,283 | ..... | ..... | [b] 1,263 |
| 99.5 | ..... | [b] 1,283<br>1,286 | ..... | ..... | [b] 1,264 |
| 99.0 | ..... | [c] 1,284 | ..... | ..... | [c] 1,233 |
| 98.5 | ..... | 1,289 | ..... | ..... | ..... |
| 98.0 | ..... | 1,286 | ..... | 1,282 | 1,223 |
| 96.5 | ..... | 1,294 | ..... | 1,283 | 1,234 |
| 95.0 | ..... | 1,289 | ..... | [c] 1,281<br>1,283 | [c] 1,241<br>1,228 |
| 93.5 | ..... | 1,285 | ..... | ..... | ..... |
| 92.5 | ..... | 1,299 | ..... | 1,282 | ..... |
| 91.0 | ..... | 1,297 | ..... | 1,271 | ..... |
| 90.0 | ..... | 1,303 | ..... | [c] 1,280<br>1,284 | [c] 1,238<br>1,239 |
| 87.5 | ..... | 1,309 | ..... | ..... | ..... |
| 85.0 | ..... | 1,309 | ..... | [c] 1,286 | [c] 1,240 |
| 82.5 | ..... | 1,548 | ..... | ..... | ..... |
| 80.0 | 1,588 | 1,548 | ..... | 1,280 | ..... |
| 77.5 | 1,682 | 1,551 | ..... | ..... | ..... |
| 75.0 | 1,832 | 1,550 | ..... | ..... | ..... |
| 72.5 | 1,808 | 1,550 | ..... | ..... | [c] 1,239 |
| 70.0 | 1,874 | 1,562 | ..... | ..... | ..... |
| 67.5 | 1,808 | ..... | ..... | ..... | ..... |
| 65.0 | 1,748 | 1,550 | ..... | [b] 1,284 | [b] 1,267 |
| 64.0 | ..... | ..... | ..... | ..... | ..... |
| 61.0 | 1,642 | ..... | 1,547 | ..... | ..... |
| 60.0 | 1,551 | ..... | 1,550 | [c] 1,282 | [c] 1,253 |
| 57.5 | ..... | 1,787 | 1,548 | ..... | ..... |
| 55.0 | ..... | 1,820 | 1,556 | ..... | ..... |
| 50.0 | ..... | 1,885 | 1,554 | ..... | ..... |
| 45.0 | ..... | 1,882 | 1,552 | [c] 1,270 | [c] 1,237 |
| 40.0 | ..... | 1,843 | ..... | ..... | ..... |
| 35.0 | ..... | 1,858 | ..... | ..... | ..... |

[a] All points not otherwise indicated were determined in high-frequency induction furnace, using an optical pyrometer.
[b] Points determined in resistance furnace.
[c] Points determined in high-frequency furnace with thermocouple.

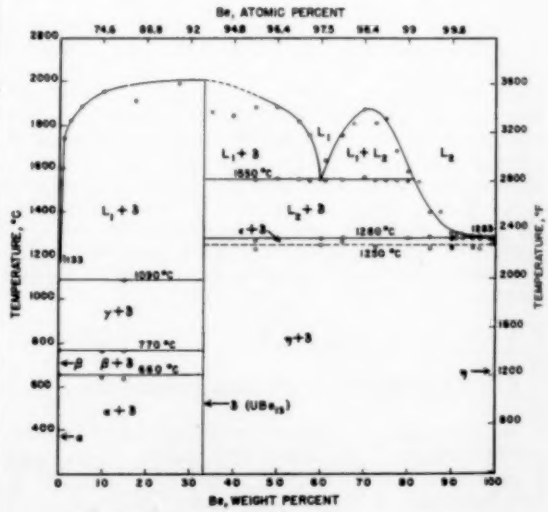


FIGURE 5. *Beryllium-uranium phase diagram.*

Metallographic examination showed that the cast structures of the alloys in the composition range 3 to 100-weight-percent beryllium consisted of particles of $UBe_{13}$ embedded in a beryllium matrix. Homogenizing treatments up to 1,225° C produced no change in the structures. The compound appeared in an angular form (figs. 4, A, B, D) over the entire composition range, with the exception of a narrow range between 92- to 80-weight-percent beryllium, in which the compound was observed to have a globular form (fig. 4, C). All evidence indicated the solubility of uranium in beryllium was very limited and was not detected in this investigation.

### 4.3. Uranium-rich alloys

The cooling curves (table 3) obtained for the uranium-rich alloys indicate a eutectic at approximately 0.12-weight-percent beryllium and 1,090° C. Arrests were obtained at 770° and 660° C that correspond to the two allotropic transformation temperatures, indicating little or no solid solution of beryllium in alpha or beta uranium (fig. 6).

TABLE 3. *Summary of thermal data obtained for the uranium-rich alloys*

| Be | Thermal arrests [a] | | | |
|---|---|---|---|---|
| | Liquidus | Solidus | $\gamma-\beta$ | $\beta-\alpha$ |
| wt-% | °C | °C | °C | °C |
| 0.000 [b] | [b] 1,134 | ..... | [b] 768 | [b] 657 |
| .027 | [b] 1,128 | [b] 1,116 | 772 | [b] 660 |
| .043 | [b] 1,117 | [b] 1,108 | [b] 770 | [b] 657 |
| .079 | [b] 1,100 | [b] 1,080 | [b] 770 | [b] 658 |
| .0955 | 1,095 | ..... | ..... | ..... |
| .107 | [b] 1,119 | [b] 1,085 | [b] 766 | [b] 652 |
| .113 | [b] 1,109 | [b] 1,086 | [b] 768 | [b] 655 |
| .15 | ..... | ..... | [b] 769 | [b] 655 |
| .177 | ..... | [b] 1,091 | [b] 766 | [b] 654 |
| .2 | 1,183 | ..... | ..... | ..... |
| .5 | 1,543 | ..... | ..... | ..... |
| 1.0 | 1,743 | ..... | ..... | ..... |
| 2.5 | 1,827 | ..... | ..... | ..... |
| 5.0 | 1,887 | ..... | ..... | ..... |
| 10.0 | 1,952 | ..... | [b] 765 | ..... |
| 15.0 | 1,910 | [b] 1,090 | [b] 761 | ..... |
| 20.0 | 1,910 | ..... | ..... | ..... |
| 27.5 | 1,993 | ..... | ..... | ..... |

[a] All points not otherwise indicated were determined in high-frequency induction furnace, using an optical pyrometer.
[b] Points determined in resistance furnace.

Metallographic examination showed that alloys in the vicinity of the uranium-$UBe_{13}$ eutectic, as indicated by thermal analysis, contained a definite eutectic structure (figs. 4, G, H). Homogenization near the solidus spherodized the U $Be_{13}$. X-ray analysis of alloys quenched from 1,075° C in the range 0.027 to 0.079-weight-percent beryllium, placed the solid solubility of beryllium in gamma uranium between 0.042 to 0.079-weight-percent at 1,075° C.

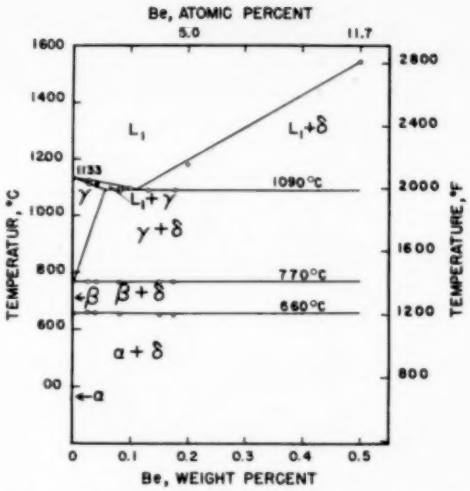


FIGURE 6. *Uranium-rich section of beryllium-uranium phase diagram.*

## 5. Summary

The phase diagram of beryllium and uranium was constructed from data obtained by thermal analysis, metallographic examination, and X-ray diffraction (figs. 5 and 6). The beryllium-uranium system is characterized by one intermetallic compound, $UBe_{13}$, having a melting point of approximately 2,000° C. A eutectic, having a composition of approximately 0.12-weight-percent beryllium, occurs between uranium and $UBe_{13}$ at 1,090° C. A monotectic occurs at 1,550° C and 60-weight-percent beryllium.

A slight solubility of beryllium in gamma-uranium is indicated, but no solubility of uranium in beryllium was detected. The transformation temperatures of uranium were unaffected by additions of beryllium.

---

The author expresses his appreciation to John H. Darr, J. T. Sterling, and S. J. Rosenberg for their assistance in developing the thermal data; to R. A. Lindberg for the preparation of the beryllia refractories; to H. C. Vacher, Ellen A. Buzzard, and Robert Liss for the X-ray and metallographic analysis; to Martha S. Richmond for the chemical analysis; and to Martha M. Darr for the spectrographic analysis.

WASHINGTON, October 1, 1952.

rnal of Research of the National Bureau of Standards Vol. 50, No. 2, February 1953 Research Paper 2390

# Pulsed Light System for Multiple-Cell Ultracentrifuge Rotor

M. Wales, P. G. Sulzer, and L. C. Williams

A system for photographing any spot on a moving rotor is described. A pulsed light, triggered by a signal obtained from a small alternator on the rotor shaft, is used. By shifting the phase of the light, any desired location on the rotor may be kept in view. This system is used to record data from an ultracentrifuge having four symmetrically placed cells on the rotor. A scaler-counter circuit is included for speed measurement.

## 1. Introduction

In certain types of ultracentrifuge measurements it is desirable to investigate more than one sample at once. Beams [1] has devised a method for making many sedimentation velocity measurements simultaneously, in order to carry out the Gofman test for lipoprotein on a large number of samples. Sedimentation equilibrium measurements often require a long waiting period for the attainment of equilibrium.[2] It would, therefore, be advantageous to carry out measurements on as many solutions as possible at the same time, especially when an extrapolation to infinite dilution must be made.[3] The present paper gives an account of an arrangement that enables four symmetrically placed cells, all containing solutions, to be photographed separately, using the Svedberg [4] equilibrium machine.

## 2. Principle of Operation

The rotor of late models of this ultracentrifuge has four holes to accommodate three solution cells and a reference cell as shown in figure 1. The three solution cells are unequally spaced, radially, in order to separate the scale images photographed through each one. This arrangement has two disadvantages: (1) the column of solution is so short that the regions of optical uncertainty near the bottom of the cell and the meniscus comprise a rather large fraction of the cell, and (2) great care must be used in filling the cells when maximum column length is desired, in order to obtain visible menisci. Furthermore, it has been suspected for some time that the use of a separate reference cell, where part of the scale is photographed through air to give reference lines,[4] is unnecessary. Reference lines photographed through the quartz windows in the upper (unfilled) part of a solution cell gave reproducible reference readings. Therefore, four longer, symmetrically placed solution cells were constructed,[5] with the cell inserts [4] of type 316 stainless steel and the barrels of dural. Dural inserts had given corrosion troubles in aqueous solution and could not be permanently plated. Other types of stainless steel corroded in aqueous salt solutions.

The four cells could be photographed separately by interrupting the light source in such a way as to illuminate the same cell at each flash, while all other cells would be dark. This could be accomplished, in principle, in several ways: (1) mechanically, by gearing a rotating disk with a window in it to the drive-shaft of the motor, and providing suitable means for phase change, (2) electrically, either by driving a rotating disk with a motor synchronized to the centrifuge shaft, or by pulsing a gaseous discharge tube in synchronism. The first method was not tried because of the difficulty of obtaining access to the centrifuge shaft without extensive changes in the design of the machine. However, electrical synchronization appeared promising, because the manufacturer had installed a small coil and magnet alternator on the end of the shaft. This was intended to be used in connection with a pulse-shaping circuit, oscilloscope, and oscillator to measure the speed of rotation. It was found to be simpler and less expensive to feed the output into a scaler circuit with a

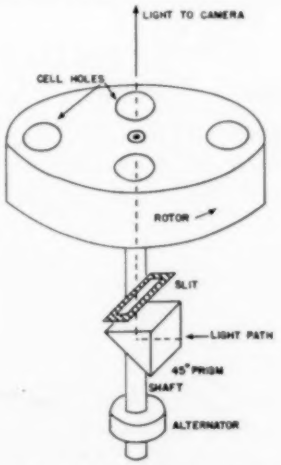


FIGURE 1. *Diagram of ultracentrifuge rotor showing path of light.*

[1] J. W. Beams, private communication.
[2] M. Wales, J. Applied Phys. **22**, 735 (1951).
[3] M. Wales, F. T. Adler, and K. E. Van Holde, J. Phys. Colloid Chem. **55**, 145 (1951).
[4] T. Svedberg and K. O. Pedersen, The ultracentrifuge (Oxford Press, Cambridge, England, 1940).
[5] Constructed by R. E. Ward and associates, NBS Shops Division, according to a design originated by E. Hanson, University of Wisconsin.

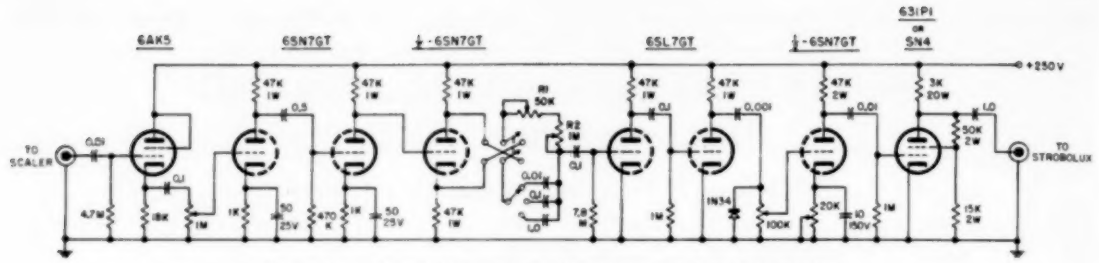


FIGURE 2. *Circuit diagram, coupling of scaler output to Strobolux.*

scale of 64, driving a register, and to count the speed directly. This arrangement was checked for internal consistency by means of an applied 60-cycle pulse (a-c line), the time interval being measured by a synchronous automatic timer, also driven from the line. The circuit was also checked against standard frequencies available at the National Bureau of Standards.

From the 1:8 and 1:16 stages of the scaler, provision was made to tap off the output through a cathode-follower circuit and amplifier, to drive a small synchronous motor. Unfortunately, the wave form obtained was so irregular that the motor would not run in synchronism except at a 1:1 frequency ratio, with the scaler out of the circuit. This made it inadvisable to use the motor because the speed range of the centrifuge is 30 to 300 rps, and the motor could be run only at 30 to 80 rps.

The final arrangement, which proved to be successful, is shown in figure 2. A Stroboluxpulsed light-source assembly was driven with the amplified signal from the centrifuge shaft, via the scaler circuit at a frequency ratio of 1:8 (or 1:16 if desired). Provision for shifting the phase of the signal by $\pm 180°$ was made in order to illuminate any desired cell.

Cells were distinguished by means of identifying dots painted on the far ends of the windows, away from the column of solution. The cell image was centered in the field of view in the camera by means of the potentiometers $R_1$ and $R_2$, which were brought back to the vicinity of the camera. The images were remarkably stable and remained well centered for as long as 15 min without adjustment.

Light from the Strobolux was concentrated on the entrance window of the centrifuge optical system by means of a truncated cone of kraft paper covered on the inside with smooth aluminum foil. This material is commonly used for insulation and is readily available. A thin frosted-glass diffuser was necessary for uniform illumination of the scale. A filter, designed originally to isolate the mercury green line, was also used in order to obtain nearly monochromatic light. Under these conditions exposures of 3 to 4 min were required to obtain good scale photographs on CTC Kodaline plates.

It is expected that this arrangement will materially increase the utility of the equilibrium ultracentrifuge.

WASHINGTON, December 1, 1952.

rnal of Research of the National Bureau of Standards Vol. 50, No. 2, February 1953 Research Paper 2391

# Damping of Elastically Supported Element in a Vacuum Tube

S. Levy, E. V. Hobbs, W. D. Kroll, and L. Mordfin

It is shown that it is possible to damp the motion of an element in a vacuum tube by making the tube part of a two-degree-of-freedom system. The equations of motion of this system are presented. The optimum values of the parameters are determined on SEAC, the National Bureau of Standards electronic automatic computer, for a particular set of design requirements. In carrying out this computation, SEAC is used not only to compute the displacements of the system for given values of the parameters, but also to choose that set of parameters for which the performance is optimum. A description is given of a tube mount built in accordance with the computations and of the degree of damping achieved.

## 1. Introduction

In the development of the Ramberg vacuum-tube accelerometer,[1] the problem arose of eliminating excessive electrical output in the neighborhood of the resonant frequency. One solution of this problem was to include an electrical filter in the output of the accelerometer to electrically remove the effects of resonance of the mechanical system. As long as the resonant amplitude was in the linear range, such a filter was adequate. In some applications, however, large resonant amplitudes, beyond the range of linearity between mechanical displacement and electrical output, might be present, and for these it was considered desirable to damp the mechanical vibration directly.

The damping system described herein was especially designed to give good damping for the Ramberg vacuum-tube accelerometer. The design requirements were those for an accelerometer, namely, constant displacement amplitude and phase shift changing linearly with frequency, for frequencies from zero up to the natural frequency. The methods presented for achieving these design requirements are general and can be used where other types of damping are required

## 2. Mechanical System

A diagrammatic sketch of the mechanical system used to damp response of an elastically supported element in a vacuum tube is shown in figure 1 (a).

A difficulty in damping the motion of elements of a vacuum tube by dampers attached to the tube base is that the elements are usually so light that their motion causes negligibly small motion of the tube base. To increase the motion of the tube base, and thus the absorption of energy from a particular vibrating element, the auxiliary mass $m$ is used in the design shown in figure 1 (a). This mass is supported on a spring $k$ so chosen that the natural frequency of the mass, with the tube base clamped, is the same as the natural frequency of the element to be damped. Under these circumstances, the response of the tube element and the mass, $m$, to motion of the tube base is the same. The mass $m$ is large enough to force appreciable motion of the tube base, with a resultant damping of the motion of both $m$ and the tube element by damper $c$.

The springs $K$ support the tube from the outside case.

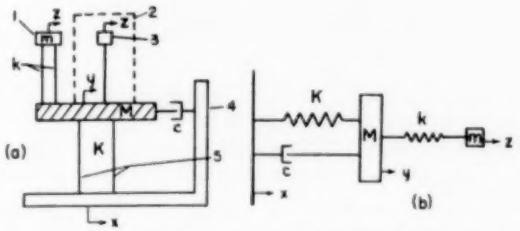


FIGURE 1. *a, Schematic diagram of mechanical arrangement for damping response of an elastically supported element in a vacuum tube; b, equivalent two-degree-of-freedom mechanical system.*

1, Auxiliary external mass elastically supported on cantilever springs; 2, tube envelope; 3, elastically supported element; 4, case; 5, cantilever springs mounting tube in case.

## 3. Equations of Motion

For purposes of analysis, the mechanical system of figure 1 (a) is idealized to that of figure 1 (b). The displacement $(z-y)$ of mass $m$ (and therefore of the tube element) to motions $x$ of the case will now be determined.

Writing the equations of equilibrium for masses $m$ and $M$ gives

$$m(d^2z/dt^2)+k(z-y)=0. \tag{1}$$

$$M(d^2y/dt^2)+K(y-x)+k(y-z)+c(dy/dt)-c(dx/dt)=0. \tag{2}$$

These equations are solved on the assumption that the disturbance at the case is of constant amplitude $a$ and radian frequency $\omega$

$$x=a \sin \omega t. \tag{3}$$

[1]Walter Ramberg, Vacuum tube acceleration pickup, J. Research NBS 37, 391 (December 1946) RP1754. The measurement of acceleration with a vacuum tube, Trans. Am. Inst. Elec. Engrs. 66 (1947). Samuel Levy, Recent developments in the Ramberg vacuum tube accelerometer, Proc. Soc. Exp. Stress Analysis, IX, No. 1 (1951).

The following substitutions are made:

$$k/m=\theta^2; \quad K/M=\Omega^2; \quad c/M=\gamma; \quad m/M=\rho. \quad (4)$$

After solving eq (1) and (2), it is found that the acceleration of the mass $m$ is

$$k(z-y)/m=\theta^2(z-y)=a\omega^2(A \sin \omega t+B \cos \omega t), \quad (5)$$

where

$$A=\frac{\theta^2\Omega^2(\omega^4-\omega^2\theta^2-\omega^2\Omega^2-\omega^2\rho\theta^2+\Omega^2\theta^2)-\theta^2\omega^2\gamma^2(\omega^2-\theta^2)}{\omega^2\gamma^2(\omega^2-\theta^2)^2+(\omega^4-\omega^2\theta^2-\omega^2\Omega^2-\omega^2\rho\theta^2+\Omega^2\theta^2)^2},$$

$$B=\frac{\omega\gamma\theta^2\Omega^2(\omega^2-\theta^2)+\gamma\omega\theta^2(\omega^4-\omega^2\theta^2-\omega^2\Omega^2-\omega^2\rho\theta^2+\Omega^2\theta^2)}{\omega^2\gamma^2(\omega^2-\theta^2)^2+(\omega^4-\omega^2\theta^2-\omega^2\Omega^2-\omega^2\rho\theta^2+\Omega^2\theta^2)^2}.$$

The ratio of the maximum acceleration $\theta^2(z-y)_{max}$ of the mass $m$ to the maximum acceleration $a\omega^2$ of the case is

$$\text{Response ratio, } R=\sqrt{A^2+B^2}. \quad (6)$$

The phase shift of the amplitude $(z-y)$ with respect to the motion $x$ of the base is seen from eq (5) to be

$$\phi=\tan^{-1}(B/A). \quad (7)$$

## 4. Application of SEAC

It is desired to determine the values of $\rho=m/M$, $\Omega=K/M$, and $\gamma=c/M$ for which the response ratio, eq (6), has a constant value near unity for values of the driving frequency $\omega$ between 0 and $\theta$. This was done by preparing a code for SEAC,[2] which required it to carry out automatically the following successive steps:

(1) For values of $\omega/\theta=0.1$, $\Omega/\theta=0.1$, $\gamma/\theta=1.0$, and $\rho=0.6$ compute the values of $A$ and $B$, eq (5), and from them the response ratio, $R$, eq (6). Store $R$ temporarily.

(2) Increase the value of $\omega/\theta$ successively to 0.3, 0.5, 0.7, and 0.9, repeating step (1) for each new value.

(3) Determine the maximum, $R_{max}$, of $R_{0.1}$, $R_{0.3}$, . . . $R_{0.9}$ and store temporarily.

(4) Compute a criterion $C$ of flat response from $C=R_{0.1}+0.3R_{0.3}+0.1R_{0.5}+.03R_{max}-1.43$ and store temporarily.

(5) Increase $\Omega/\theta$ in steps of 0.1 from 0.1 to 1.6, $\gamma/\theta$ in steps of 0.1 from 1.0 to 2.0, and $\rho$ in steps of 0.2 from 0.6 to 2.0, and repeat steps (1) to (4) saving the results for the best five cases (those where the absolute value of $C$ is smallest).

(6) Print the results for the five best cases.

The best values were

$$\Omega/\theta=0.1, \quad \rho=1.8, \quad \text{and } \gamma/\theta=1.9. \quad (8)$$

The curve of response ratio versus frequency ratio corresponding to these values is shown in figure 2.

[2] SEAC, the National Bureau of Standards Eastern Automatic Computer, NBS Technical News Bulletin **34**, p. 9, (Sept. 1950).

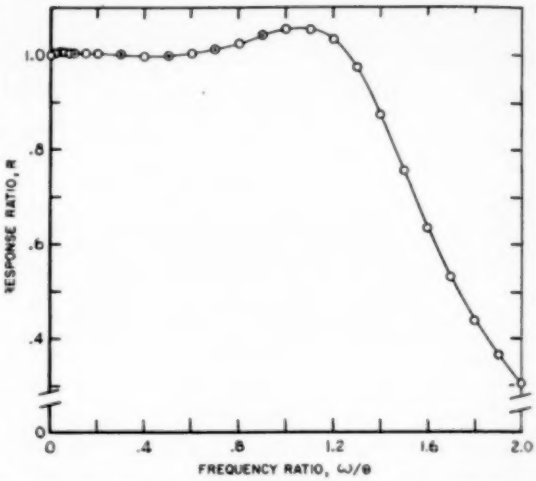


FIGURE 2. *Response curve for optimum values of design variables.*
($\gamma/\theta=1.9$; $\rho=1.8$; $\Omega/\theta=0.1$)
●, Computed on SEAC; ○, computed by hand.

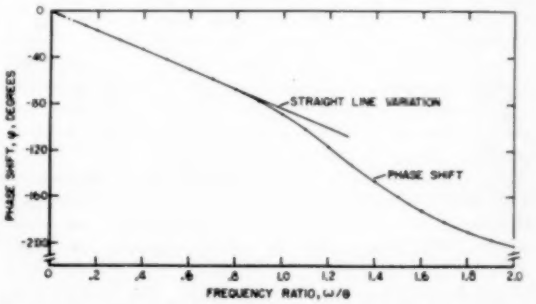


FIGURE 3. *Phase shift for optimum values of design variables.*
($\gamma/\theta=1.9$; $\rho=1.8$; $\Omega/\theta=0.1$)

The response ratio is within 1 percent of 1.00 for values of $\omega/\theta$ less than 0.67. It is within 6 percent of 1.00 for $\omega/\theta$ less than 1.34. The phase shift for this case was computed from eq (7) and is plotted in figure 3. The departure from a straight line is negligible for $\omega/\theta$ less than 0.75. It should be noted that the additional points computed by hand for figure 2 fit in perfectly with those computed on SEAC.

An important operation of SEAC for this problem was that it not only computed the responses but also, with the aid of the criterion $C$, chose the parameters for which the response curve was flattest. In this way, the plotting by hand and the visual comparison which might otherwise have been needed were avoided.

In the coding of this problem for SEAC, no effort was made to include the linearity of the phase shift as part of the criterion $C$. This could have been done, with only minor changes in the coding, if it had been found necessary.

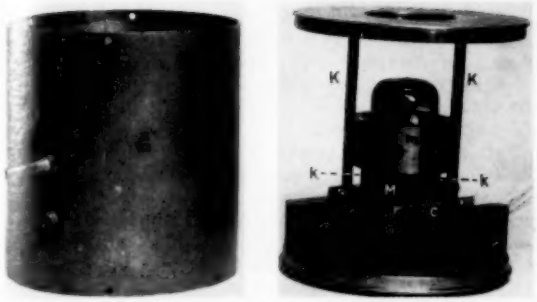


FIGURE 4. *Ramberg vacuum tube accelerometer as part of a two-degree-of-freedom system having optimum parameters for damping resonant amplitudes and giving the accelerometer a flat frequency-response curve.*

## 5. Damper Design

A damper designed as indicated in eq (8) was constructed and is shown in figure 4 with the outer case $G$ removed. The masses $m$ and $M$, the springs $k$ and $K$, and the damper $c$ are labeled on the figure. The element of the Ramberg vacuum-tube accelerometer for which damping was desired had a natural frequency $\theta = 2\pi(161)$ rad/sec. The tube, together with the necessary base attachments, had a mass $M = 0.000285$ lb-sec$^2$/in. Using the optimum parameters given in eq (8), the elements in figure 1 were designed to have the following values:

$$m = \rho M = 1.8(0.000285) = 0.000513 \text{ lb-sec}^2/\text{in}.$$

$$k = m\theta^2 = (0.000513)4\pi^2(161)^2 = 526 \text{ lb/in}. \quad (9)$$

$$c = \gamma M = 1.9\theta M = 1.9(2\pi)(161)(0.000285) = 0.548 \text{ lb-sec/in}.$$

$$K = M\Omega^2 = M(0.1\theta)^2 = (0.000285)4\pi^2(16.1)^2 = 2.92 \text{ lb/in}.$$

## 6. Electrical Output at Natural Frequency

To determine whether the damper was successful in limiting electrical output at the natural frequency the tube was subjected to a sudden change in acceleration. Such a change in acceleration should excite vibration at the natural frequency. Since the electrical output of the Ramberg vacuum-tube accelerometer is a direct measure of the displacement of the elastically supported element, the effect of the case on the vibration of the tube element could be conveniently determined by recording the accelerometer output. The desired sudden change in acceleration was obtained by mounting the tube at the end of a cantilever beam $A$, figure 5, whose tip was deflected sideways by a force, $W$, of several times the weight of the mounted tube, $T$. Cutting the support wire, $S$, caused the desired sudden change in acceleration.

The results of this test are shown in figure 6. It is evident from comparison of figures 6 (a), with the

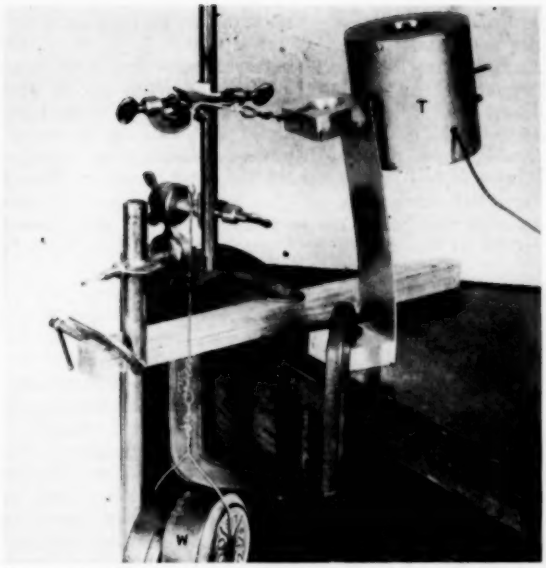


FIGURE 5. *Test set-up for determining the degree of damping of natural frequency achieved by making tube part of a two-degree-of-freedom system.*

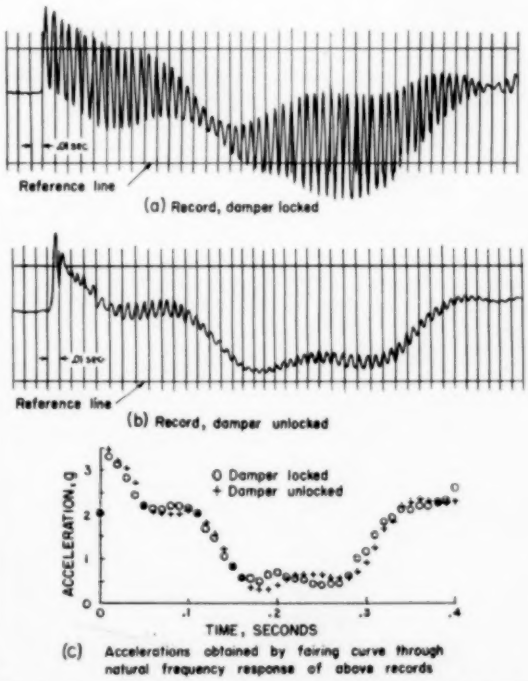


FIGURE 6. *Records of acceleration obtained in tests to determine effectiveness of damper in reducing response at 161 c/s natural frequency of tube.*

damper locked to prevent relative motion between the tube and the cantilever tip, and 6 (b) with the damper unlocked that a marked reduction in natural frequency electrical output results from use of the damper. In figure 6 (c) it is seen that the acceleration-time history obtained by fairing a curve through the natural frequency response in figures 6 (a) and 6 (b) gives nearly identical results. This is expected since none of the output in figure 6 (a) exceeds the linear range of about 6 *g* for the 161 c/s model of the Ramberg vacuum-tube accelerometer.

## 7. Accelerometer Performance

Preliminary tests have been completed to determine the extent to which the performance of the accelerometer is in agreement with the computed curves, figures 2 and 3. In these tests, the accelerometer was driven by an electromechanical shaker at frequencies from 10 to 200 c/s, and the output of the accelerometer was viewed on an oscilloscope. It was observed that large amplitude electrical output at the natural frequency was present. This has been tentatively ascribed to nonlinearity. Other damping fluids and dash-pot designs will be considered in an effort to eliminate t' is difficulty.

## 8. Conclusions

The following conclusions can be drawn from this investigation:

(1) The vibration of an element in a vacuum tube due to external disturbances can be damped by making the tube a part of a two-degree-of-freedom mechanical system having suitable constants.

(2) The National Bureau of Standards electroni automatic computing machine, SEAC, is an excellen means for computing the displacements of dynami systems, particularly where it is desired to comput the displacements for many different values of th mechanical parameters.

(3) SEAC can be conveniently used as a substitut for hand plotting of results and visual inspection of curves in selecting optimum parameters of a system by having SEAC compute, in addition to a solution of the problem, a criterion of quality and having it select the solution for which the criterion is best.

(4) Further work is indicated to investigate the cause of and to eliminate the large amplitude electrical output of the accelerometer when driven at its natural frequency.

---

The authors acknowledge the assistance of members of the Engineering Mechanics Section of the National Bureau of Standards, particularly that of the late A. E. McPherson. They also take this opportunity to acknowledge the major contribution of Ida Rhodes of the Bureau's Computation Section in coding the dynamic analysis for SEAC and in helping formulate the analysis so that SEAC could be used to best advantage.

The work was carried out in the Engineering Mechanics Section, National Bureau of Standards, under the sponsorship of the Office of Basic Instrumentation with the financial assistance of the Office of Naval Research, Office of Air Research and Atomic Energy Commission.

WASHINGTON, July 17, 1952.

rnal of Research of the National Bureau of Standards Vol. 50, No. 2, February 1953 Research Paper 2392

# Calorimetric Determination of the Half-Life of Polonium

D. C. Ginnings, Anne F. Ball, and D. T. Vier [1]

The heats of radioactivity of four samples of polonium have been measured with a Bunsen ice calorimeter over a period of about seven months. With samples ranging in initial powers from 0.17 to 1.4 watts, the half-life values calculated from these measurements were found to agree within 0.1 percent, or the equivalent of 0.0003 watt, whichever was the larger. The results with the sample with the largest power gave a half-life value of 138.39 days, with an uncertainty of 0.1 percent (0.14 day). This is in agreement with the value of 138.3 days (±0.1 percent) reported by Beamer and Easton, who used a different calorimetric method.

## 1. Introduction

Of all published determinations of the half-life of polonium, probably the most accurate is that by Beamer and Easton [1],[2] who used a calorimetric method and observed a sample for as long as 97 days. Their method consisted in measuring the temperature difference between a container with the sample of polonium and an identical container that was empty. Both containers were surrounded by an isothermal jacket, and the relation between temperature difference and power was determined by means of electric calibration experiments. The value of the half-life was found to be 138.3 days (±0.1%). A Bunsen ice calorimeter is also suitable for measuring radioactive power (and half-life) of radioactive materials. Because this method is entirely different from that used by Beamer and Easton, and because much larger samples of polonium were available, it seemed worth while to measure the half-life of several samples that were suitable for measurements with the ice calorimeter.

The Bunsen ice calorimeter seems ideally suited for several reasons to the measurement of the heat evolved by curie or multicurie quantities of alpha, weak beta, and with modification [2], other radioactive materials. First, the heat leak is small (perhaps 0.0002 w). Second, the calorimeter requires very little attention during the measurements, usually a few minutes every hour or two for ice-bath replenishment. Third, no electrical or temperature measuring instruments are required because the measurement of heat requires only weighing of mercury. Fourth, the calibration factor of the ice calorimeter is a fundamental physical constant, which has been determined to about 0.01 percent by electrical calibration experiments [3].

On the other hand, the ice calorimeter in its present application has an inherent variation, or error, which is comparable with its heat leak. While this does not limit the precision of experiments involving about 1-w power, it would limit the precision of measurements of much smaller powers. Other ice calorimeters designed specifically for small radioactive powers [2] have proved sensitive to as little as 0.00003 w. An improved ice calorimeter has been in use at the National Bureau of Standards for some time in the measurement of heat capacities at high temperatures [3]. Although this calorimeter was not intended for measurements of radioactive power, it seemed suitable for measurements on certain samples of polonium (alpha emitter) furnished by the Los Alamos Scientific Laboratory, which initially developed powers in the range of 0.17 to 1.4 w. By measuring the decay of radioactive power of a sample of polonium over time intervals comparable with its half-life, values were obtained of its half-life.

## 2. Experimental Details

The ice calorimeter used in these experiments is shown in figure 1. It is the same calorimeter previously described [3]. An ice mantle (I) was frozen around the central calorimeter well (A) on a system of copper vanes (F) designed to increase the area of contact of the central well with the ice. The sample was suspended in the bottom of this well by a small wire that was pushed over against one side of the well by the gate G. The heat developed in the sample melted some of the ice, thereby decreasing the volume of the ice-water system and causing mercury to be forced into the calorimeter from beaker B. A small flow upward of dry helium in the calorimeter well was maintained to prevent condensation of water vapor from the room in the calorimeter and also to increase thermal contact between the sample and the calorimeter.

The polonium samples were sealed in glass or metal containers, which were enclosed in brass outer containers made to fit closely to the central well of the ice calorimeter. Because the radiation from polonium is essentially all of the alpha type, the containers were completely effective in converting all the radioactive energy into heat within the container. A sample was lowered into the calorimeter (with the two platinum shields above it, as described elsewhere [4]), and about 10 or 15 min was allowed for it to come to essentially a steady temperature, the valve V being open. Then the mercury meniscus was adjusted to the upper part of the scale, C, by partly evacuating reservoir R. Valve V was immediately closed, thereby causing the meniscus at C to start to move downward due to the heat input to the calorimeter. The time wa

[1] Los Alamos Scientific Laboratory, University of California.
[2] Figures in brackets indicate the literature references at the end of this paper.

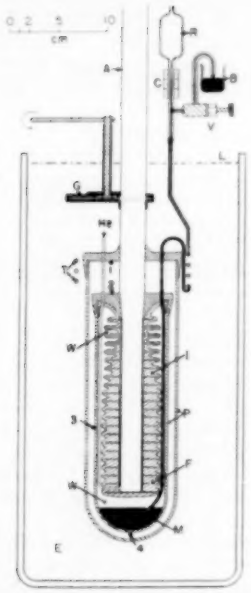

FIGURE 1. *Schematic diagram of ice calorimeter.*

A, calorimeter well; B, beaker containing mercury; C, glass capillary; E, ice bath; F, copper vanes; G, gate; I, ice mantle; M, mercury; P, Pyrex containers; R, mercury reservoir; T, mercury "tempering" coil; V, needle valve; W, water; 1, 2, 3, and 4, thermocouple junctions.

recorded when the meniscus passed an arbitrary zero on this scale, the beaker of mercury (B) was replaced by a weighed beaker of mercury, and valve V opened again. At the end of an experiment, the valve was closed again and the time recorded when the meniscus again passed its zero. The difference in the weights of the beaker gave the weight of mercury sucked into the calorimeter in a measured time. A small correction (perhaps 1 joule) was made for heat leak. The corrected mass of mercury was converted to energy by use of the calibration factor of the ice calorimeter as previously determined [3], 270.46 abs j/g of mercury for the "ideal" calorimeter or 270.47 abs j/g for the actual calorimeter used. From the duration of the experiment (difference in times at which the mercury meniscus passed the arbitrary zero), the energy was converted into average power.

The values of power calculated in the manner described would be correct if the sample and all other parts in thermal contact with the calorimeter did not change temperature during the experiment. However, as heat is put into the calorimeter, the thickness of the water layer between the ice and the central well with its vanes increases, and as there is flow of heat across this water layer, the temperature drop across this water layer must increase. As a result, the temperatures of the central well and vanes, and the sample with its container, all increase slightly during an experiment, so that part of the heat produced by the sample does not melt ice. This amount of heat depends on the power of the sample, the heat capacities of the various parts, and on the thickness of the water layer at the beginning of the experiment. The analysis of the correction for this heat is given as follows.

Consider a system (such as the radioactive sample plus metal calorimeter well with vanes) separated from ice by a layer of water. Consider also that the thermal contact between sample and calorimeter does not change during an experiment. Let

$Q$ = the total amount of heat (joules) that has been introduced into the ice calorimeter at any particular time,

$P$ = the power (j/sec) developed by the sample,

$H$ = the heat capacity (j/deg C) of the system (sample plus calorimeter well with vanes),

$A$ = the effective area of contact of the system with ice, $cm^2$,

$K$ = the thermal conductivity of water at 0° C, 0.0052 w $cm^{-1}deg^{-1}$,

$m$ = the average thickness of the water layer, cm,

$F$ = the heat of fusion of ice, 333 j/g.

Then the grams of ice melted $= Q/F = Q/333$.

The volume of water between the ice and the vanes is the same as the volume of ice melted because any void created by the difference in density of ice and water is filled almost instantaneously by water outside the mantle passing through and around the cracks in the ice mantle. Hence, the volume of water layer formed = (specific volume of ice) $(Q/333)$ $= (1.09)\ (Q/333) = 0.0033Q$; $m = 0.0033(Q/A)$; and the temperature difference across the water film $= Pm/(0.0052)A = (0.0033/0.0052)(PQ/A^2) = 0.63(PQ/A^2)$. Thus the heat stored in the system after $Q$ joules have been introduced (assuming no temperature gradient in the metal system) $= (0.63H)\ (PQ/A^2)$, and the heat stored in the water after $Q$ joules have been introduced (assume linear temperature gradient across the film) $= (4.18)\ (0.0033Q)\ (0.63/2)\ (PQ/A^2) = 0.0043\ (PQ^2/A^2)$, and the total heat stored $= (P/A^2)$ $(0.63HQ + 0.0043Q^2)$. If we start an experiment with $Q_1$ joules of heat already put into the calorimeter and a steady state of heat flow from the sample to the ice mantle, and end the experiment with $Q_2$ joules of heat in the calorimeter, and the same steady state of heat flow, then the difference in heat stored $= (P/A^2)[0.63H(Q_2 - Q_1) + 0.0043(Q_2^2 - Q_1^2)]$.

The relative error, $E$, is

$$E = \frac{P}{A^2(Q_2 - Q_1)}\ [0.63H(Q_2 - Q_1) + 0.0043(Q_2^2 - Q_1^2)],\ \text{or}$$

$$E = \frac{P}{A^2}\ [0.63H + 0.0043(Q_2 + Q_1)].$$

If $E$ is plotted against $(Q_2 + Q_1)$, the slope of the resulting straight line is

$$\text{Slope} = 0.0043\ \frac{P}{A^2},$$

and the intercept of this line with the $E$ axis is

$$\text{Intercept} = 0.63\ \frac{HP}{A^2}.$$

his analysis shows that for any given power $P$ of e sample, the slope of this line is dependent only the effective area of contact ($A$) of the metal vanes ith the ice. This effective area depends, of course, the length of the sample. The intercept of this ne with the relative error axis depends not only pon the area $A$ but also upon the heat capacity, $H$ of the sample-plus-vane system.

For any given sample with a known heat capacity nd length, values of $A$ and $H$ can be calculated, using the dimensions and heat capacity of the corresponding portion of the calorimeter well and its system of vanes. It is believed that a better evaluation of $A$ and $H$ can be obtained by electrical calibration experiments, putting in known quantities of electric heat into the calorimeter over a length equivalent to the radioactive samples to be measured. If the heat is distributed in the electrical experiments the same as in the experiments with the radioactive samples, the value of $A$ obtained from the electrical experiments should also be the same. However, the value of $H$ obtained from the electrical experiments differs from that for the radioactive experiments by the difference in heat capacities of the electric heater and the radioactive samples.

The results of the electric calibration experiments are indicated by the circles in figure 2, which shows the relative error, $E$, plotted against $(Q_1+Q_2)$. The best straight line through these circles is labeled "Electric Experiments" and was determined by the method of least squares to be $E=0.000633+2.992\times 10^{-5}(Q_1+Q_2)$, where $Q_1$ and $Q_2$ are expressed in joules. The electric calibration experiments were made with a power of about 1.4 w to correspond approximately to the initial radioactive power of sample 4, which was the largest of the four samples and therefore had the largest correction for the water layer. The slope of the solid line (electric experiments) indicated that the effective area of contact ($A$) between the ice and the source of heat was about 420 cm². This is roughly equivalent to a 9-cm length of the calorimeter well, as compared to an actual length of the electric heater of about 7 cm.

While the value of $A$ obtained from the electric calibration experiments agreed as well as expected with that estimated from the dimensions, the value of heat capacity $H$ (after correction for the heat capacity of the heater) corresponded to about a 17-cm length of the calorimeter well, which is considerably more than expected. Some of this difference may be due to the assumption in the theory that the temperature gradient in the copper vanes is negligible. If the position of the line had been calculated entirely on the basis of a 9-cm length of the calorimeter well, it would have the same slope as the line given by the electric experiments but would be shifted to decrease $E$ by almost 0.0003. Because it is believed that the electric calibration experiments give more reliable values of the effective $A$ and $H$, the solid line in figure 2 was used as basis for the corrections for the experiments with the radioactive samples. The dashed lines shown in the figure for sample 4 were calculated on this basis, as well as corresponding lines (not shown) for the other samples. Values of apparent calibration factor (which is equivalent to 270.47 $(1+E)$) were read from the dashed lines for the corresponding values of $(Q_1+Q_2)$.

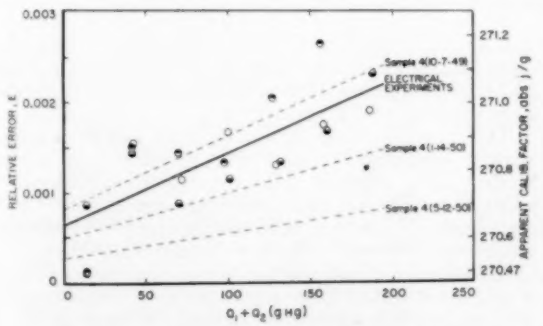


FIGURE 2. *Corrections for water layer in calorimeter.*
Electrical experiments: ◓, 10-11-49; ◒, 10-12-49; ○, 10-14-49.

## 3. Results

The results of the measurements with the four samples are given in table 1. The mean time of experiment is given, so that all experiments in one group can be corrected for the radioactive decay to bring them all to the same time (noon, EST) on the reference date. The mass of mercury was corrected for the effect of heat leak between the calorimeter and its surroundings (this effect is usually only a few milligrams of mercury). The quantities $Q_1$ and $Q_2$ are as previously described. Using the quantity $Q_1+Q_2$, the apparent calibration factor of the ice calorimeter was obtained from figure 2, from the curve for the appropriate sample. The product of this factor and the mass of mercury, divided by the duration of the experiment, gives the power at mean time of experiment. Using an approximate value of the half-life of polonium, this power was converted to power at noon (EST) on the reference date. The deviations from mean power are the deviations of the results of the individual experiments from the mean power of the group of experiments. The values of half-life given in the last column are based on the mean powers and reference dates, and the values indicated in parentheses are the authors' estimated uncertainties of the half-life based on both accidental and systematic errors.

It will be noted that more measurements were made with sample 4 than with the other three samples. This was because sample 4 had the highest power of the four samples, and it was believed that the highest relative calorimetric accuracy could be obtained with this sample, resulting in the best determination of the half-life of polonium. The power of sample 1 was so low that calorimetric errors could account for the low value of half-life calculated. The uncertainty in heat leak of the calorimeter was believed to be about 0.0002 w. This uncertainty, when compared with the power measured for sample 1 on May 14, 1950 (0.05698 w), could explain most of the discrepancy with the results with the other

TABLE 1. *Results of experiments*

| Date of experiment | Mean time of experiment EST | Duration of experiment | Mass of mercury | $O_1$ | $O_2$ | Apparent calorimeter factor $270.47(1+E)$ | Power at mean time of experiment | Power at noon (EST) on reference date | Reference date | Deviations from mean power | Mean power | Half-life |
|---|---|---|---|---|---|---|---|---|---|---|---|---|
| | | | | | | Sample 1 | | | | | | |
| | | *sec* | *g* | *g* Hg | *g* Hg | $jg^{-1}$ | *abs w* | *abs w* | | *percent* | *abs w* | *Days* |
| 10-3-49 | 3:24 p. m. | 3 557.8 | 2.3048 | 0 | 2 | 270.49 | 0.17533 | [a] 0.17451 | | +0.16 | | |
| | 6:36 p. m. | 12 367.2 | 7.9892 | 2 | 10 | 270.49 | .17474 | .17411 | 10- 4-49 | −0.07 | 0.17423 | |
| 10-4-49 | 12:32 p. m. | 9 928.0 | 6.3924 | 10 | 17 | 270.50 | .17417 | .17419 | | −0.02 | | |
| | 3:20 p. m. | 10 126.5 | 6.5205 | 17 | 23 | 270.50 | .17418 | .17430 | | +0.04 | | |
| 5-3-50 | 1:14 p. m. | 20 354.0 | 4.5269 | 24 | 29 | 270.48 | .06016 | .05694 | | +0.07 | | 137.7 [b] (±1.0) |
| 5-4-50 | 1:19 p. m. | 19 440.0 | 4.2913 | 29 | 34 | 270.48 | .05971 | .05686 | | −0.32 | | |
| | 2:16 p. m. | 21 909.5 | 4.6221 | 6 | 5 | 270.48 | .05706 | .05709 | 5-14-50 | +0.19 | 0.05698 | |
| 5-14-50 | 7:14 p. m. | 13 948.0 | 2.9396 | 5 | 8 | 270.48 | .05709 | .05709 | | +0.19 | | |
| | | | | | | Sample 2 | | | | | | |
| | 11:10 a. m. | 6 168.5 | 9.1630 | 23 | 32 | 270.56 | 0.40190 | 0.40183 | | +0.04 | | |
| 10-5-49 | 12:45 p. m. | 5 224.0 | 7.7486 | 32 | 40 | 270.57 | .40133 | .40139 | 10- 5-49 | −0.06 | 0.40165 | |
| | 2:15 p. m. | 5 478.0 | 8.1294 | 40 | 48 | 270.58 | .40154 | .40173 | | +0.02 | | 138.52 [b] (±0.4) |
| 4-27-50 | 1:48 p. m. | 16 514.9 | 8.8470 | 24 | 33 | 270.50 | .14491 | .14425 | 4-28-50 | +0.18 | 0.14399 | |
| 4-28-50 | 1:00 p. m. | 17 966.8 | 9.5623 | 33 | 43 | 270.50 | .14370 | .14373 | | −0.18 | | |
| | | | | | | Sample 3 | | | | | | |
| | 1:24 p. m. | 5 134.4 | 12.2025 | 0 | 12 | 270.58 | 0.64376 | 0.64323 | | +0.02 | | |
| 10-8-49 | 2:45 p. m. | 5 207.5 | 12.3623 | 12 | 24 | 270.61 | .64241 | .64278 | 10- 8-49 | −0.05 | 0.64312 | |
| | 4:06 p. m. | 4 576.2 | 10.8695 | 24 | 35 | 270.63 | .64280 | .64335 | | +0.04 | | |
| 4-19-50 | 1:49 p. m. | 12 692.3 | 11.4817 | 0 | 11 | 270.51 | .24471 | .24358 | | −0.01 | | 138.52 [b] (±0.23) |
| 4-20-50 | 11:35 p. m. | 10 313.6 | 9.2898 | 11 | 20 | 270.52 | .24367 | .24365 | 4-20-50 | +0.02 | 0.24361 | |
| | 2:31 p. m. | 10 808.6 | 9.7279 | 20 | 30 | 270.52 | .24347 | .24360 | | 0.00 | | |
| | | | | | | Sample 4 | | | | | | |
| | 12:55 p. m. | 2 634.7 | 14.0020 | 28 | 42 | 270.84 | 1.43937 | 1.43307 | | −0.01 | | |
| | 1:35 p. m. | 2 766.9 | 14.7066 | 42 | 57 | 270.91 | 1.43994 | 1.43382 | | +0.04 | | |
| 10-6-49 | 1:28 p. m. | 2 622.8 | 13.8785 | 0 | 14 | 270.72 | 1.43251 | 1.43296 | | −0.02 | | |
| | 2:07 p. m. | 2 676.2 | 14.1607 | 14 | 28 | 270.78 | 1.43279 | 1.43345 | | +0.01 | | |
| | 2:57 p. m. | 2 733.6 | 14.4582 | 28 | 42 | 270.84 | 1.43249 | 1.43338 | 10- 7-49 | +0.01 | 1.43327 | |
| | 3:43 p. m. | 2 717.2 | 14.3735 | 42 | 57 | 270.91 | 1.43306 | 1.43423 | | +0.07 | | |
| 10-7-49 | 4:28 p. m. | 2 736.5 | 14.4643 | 57 | 71 | 270.97 | 1.43226 | 1.43361 | | +0.02 | | |
| | 5:14 p. m. | 2 689.3 | 14.1840 | 71 | 86 | 271.03 | 1.42948 | 1.43105 | | −0.15 | | 138.39 [b] (±0.14) |
| | 6:00 p. m. | 2 879.7 | 15.2113 | 86 | 101 | 271.10 | 1.43202 | 1.43382 | | +0.04 | | |
| | 11:00 a. m. | 3 170.1 | 10.2320 | 10 | 20 | 270.64 | 0.87353 | 0.87335 | | +0.05 | | |
| | 11:54 a. m. | 3 345.9 | 10.7884 | 20 | 31 | 270.67 | .87274 | .87272 | | −0.03 | | |
| | 12:50 p. m. | 3 359.8 | 10.8281 | 31 | 42 | 270.70 | .87242 | .87257 | | −0.04 | | |
| 1-14-50 | 1:44 p. m. | 3 067.7 | 9.8837 | 42 | 52 | 270.73 | .87225 | .87256 | 1-14-50 | −0.04 | 0.87294 | |
| | 2:35 p. m. | 3 115.1 | 10.0448 | 52 | 62 | 270.74 | .87302 | .87349 | | +0.06 | | |
| | 3:28 p. m. | 3 178.3 | 10.2384 | 62 | 72 | 270.78 | .87228 | .87292 | | +0.00 | | 138.40 [b] (±0.18) |
| | 10:04 a. m. | 8 282.3 | 14.8070 | 3 | 18 | 270.56 | .48370 | .48350 | | +0.00 | | |
| | 12:25 p. m. | 8 395.9 | 15.0148 | 18 | 33 | 270.58 | .48389 | .48393 | | +0.10 | | |
| | 2:46 p. m. | 8 534.5 | 15.2193 | 33 | 48 | 270.61 | .48257 | .48284 | | −0.12 | | |
| 5-12-50 | 5:00 p. m. | 7 439.2 | 13.2613 | 48 | 61 | 270.63 | .48243 | .48293 | 5-12-50 | −0.10 | 0.48342 | |
| | 6:55 p. m. | 6 260.2 | 11.1775 | 61 | 72 | 270.64 | .48322 | .48391 | | +0.09 | | |
| | 8:43 p. m. | 6 947.3 | 12.3852 | 72 | 85 | 270.66 | .48252 | .48339 | | 0.00 | | |

[a] Experiment weighted one-third because of short duration of experiment.
[b] Figure given for uncertainty based upon authors' estimate of both accidental and systematic errors.

samples having higher power because it would require an increase of only 0.0003 w in the value observed on May 14 to agree with the other samples.

It is interesting to note the corresponding effects of an uncertainty of 0.0003 w on the other samples having higher powers. With samples 2 and 3, this uncertainty in the May values would result in half-life uncertainties of about 0.21 percent (0.29 day) and 0.12 percent (0.17 day), respectively. With sample 4, however, the same power uncertainty in the values on January 14 results in only 0.04 percent (0.06 day) uncertainty in the over-all half-life. The uncertainty in heat leak is probably the largest error in the measurements with samples 1, 2, and 3. With sample 4, however, the heat leak uncertainty is probably comparable with all other errors. In addition, sample 4 was observed at an intermediate date (0.7 half-life) in an effort to detect any change in the decay constant with time.

The measurements with the four samples agree within ±0.1 percent, or 0.0003 w, whichever is the larger. The slightly different half-life values on sample 4 for the two different periods are not significant because the difference is much less than the experimental error. There is no significant evidence, therefore, of a change in the decay constant, such as would occur either if the polonium was contaminated with radioactive impurities having values of half-life different from polonium, or if some secondary chemical or nuclear reaction produced heat that was not

rectly proportional to the radioactive energy of the polonium sample. In addition, the polonium samples used were of a purity that should have precluded the possiblity of appreciable contamination by other radioactive elements. The polonium had been purified both by distillation and by electrodeposition on platinum foils from dilute nitric-acid solution of polonium nitrate. Of course, the stable lead isotope formed from the decay of polonium was present but could not affect the results of this investigation.

The best value of the half-life of polonium was estimated from the two values for sample 4, giving more weight to the earlier value, where the sample had a larger power. On this basis, the authors believe that the best value of the half-life derived from these measurements is 138.39 days. It is believed that the calorimetric uncertainties (based upon both accidental and systematic errors) in the experiments may result in an error in this value of $\pm 0.1$ percent (0.14 day).

The results of these measurements are in agreement with the value reported by Beamer and Easton [1] of 138.3 days $\pm 0.1$ percent, determined calorimetrically by another method.

## 4. References


[1] William H. Beamer and William E. Easton, J. Chem. Phys. **17,** 1298 (1949).

[2] Swietoslawski, Microcalorimetry, p. 66 (Reinhold Publishing Corporation, New York, N. Y., 1946).

[3] Defoe C. Ginnings, Thomas B. Douglas, and Anne F. Ball, J. Research NBS **45,** 23 (1950) RP2110.

[4] D. C. Ginnings and R. J. Corruccini, J. Research NBS **38,** 593 (1947) RP1797.


WASHINGTON, July 15, 1952.

Journal of Research of the National Bureau of Standards Vol. 50, No. 2, February 1953 Research Paper 2393

# Determination of Molecular Weights of Dextrans by Means of Alkaline Copper Reagents[1]

H. S. Isbell, C. F. Snyder, N. B. Holt, and M. R. Dryden

Reducing values were determined for samples of clinical dextrans, gentiobiose, and isomaltose with several alkaline copper reagents. The results for the dextrans were converted to number-average molecular weights on the assumption that equimolecular quantities of dextran, isomaltose, and gentiobiose have approximately the same reducing power. The molecular weights, thus obtained, are in fair agreement with values obtained by the recently developed radioactive cyanide method. The results show that copper-reducing methods are suitable for the determination of the number-average molecular weights of clinical dextrans.

## 1. Principles of the Method

There is widespread interest in degraded dextrans prepared from material formed by the action of *Leuconostoc mesenteroides* and other bacterial agents on sucrose. Various fractions of these carbohydrates are under investigation as blood-plasma extenders. Therefore, simple and reliable methods of analysis of these clinical products are desirable. Dextran is composed of glucose units in 1,6-glycosidic linkage, with occasional branching at carbons 3 or 4 [1, 2, 3, 4].[2] The terminal reducing unit consists of a glucose molecule substituted at carbon 6 with an alpha glucosyl group. Ordinarily, each molecule of clinical dextran has one, and only one, reducing end group. This condition arises from the manufacturing process, which ordinarily involves hydrolytic cleavage of a high-molecular-weight polysaccharide [5]. Each cleavage results in two molecules. One contains the reducing end group originally present; the other contains the reducing end group formed by cleavage of a glycosidic link. Thus there is one reducing group per molecule, and the number-average molecular weight[3] can be calculated from the number of reducing groups per unit weight.

The reducing end groups are largely responsible for the capacity of the polysaccharide to reduce alkaline copper and other reagents. For determination of reducing groups in polysaccharides of relatively low molecular weight, alkaline copper reagents, iron salts, and dinitrosalicylic acid have been most widely used. These reagents do not react stoichiometrically, and factors must be derived for converting the reducing values to molecular weight. For the determination of the molecular weights of starches, Meyer, Noelting, and Bernfeld [6] applied Sumner's dinitrosalicylic acid method and standardized the results with maltose. The reducing end group of dextran differs from that of starch in that it has a 1,6-$\alpha$ glucosyl link in place of a 1,4-$\alpha$-glucosyl link. Isbell, Pigman, and Frush [7] have shown that the position and the configuration of the glucosidic link in a disaccharide influences the molecular reducing power, and that a parallelism exists in the molecular reducing power of substances of the same or similar structure. The reducing power per molecule of a disaccharide having a 1,6-link is substantially higher than that of the corresponding monosaccharide. Presumably the higher reduction arises from cleavage of the disaccharide link in the partially oxidized product during the analysis with alkaline copper reagents. Glycosidic links in polysaccharides near the reducing groups would be broken more readily than links one or more hexose units removed from the reducing end group. For this reason the hexose units more than one unit removed from the reducing end group would not contribute appreciably to the reducing power, and a molecule of dextran should have the same reducing power as a molecule of isomaltose. Thus the molecular weight of a clinical dextran might be calculated from the reducing power of isomaltose (6-$\alpha$-D-glucopyranosyl-D-glucose). Isomaltose has not been crystallized, and the amorphous material available is of doubtful purity. Therefore, for most of the comparisons given in this paper and those given in [8] and [9], the closely related substance, gentiobiose, (6-$\beta$-D-glucopyranosyl-D-glucose) was selected as a reference standard, even though it has the beta linkage rather than the alpha linkage common to dextran and isomaltose.

In the present study copper-reducing values were measured for samples of clinical dextrans and gentiobiose by several methods, and the number-average molecular weights of the dextrans were calculated on the postulate that a molecule of dextran has the same reducing power as a molecule of gentiobiose. Table 1 gives the molecular weights thus obtained, together with those estimated by the recently developed radioactive cyanide method [10]. The results obtained by different copper-reducing methods are in fair agreement with one another and with those obtained by the cyanide method. The results show the practicability of determining number-average molecular weights by copper-reducing methods, but further refinements in the method seemed desirable.

Following the suggestion of one of us [8] that equimolecular quantities of dextran and isomaltose

[1] This work was supported, in part, by the Medical Research and Development Board, Office of The Surgeon General, Department of the Army. It was carried out under the *Plasma Volume Expanders Program of the Subcommittee on Shock*, National Research Council. The project was sponsored by the Office of the Surgeon General, U. S. Department of the Army.

[2] Figures in brackets indicate the literature references at the end of this paper.

[3] The number-average molecular weight, $M_n = \Sigma(n_i M_i)/\Sigma n_i$, where $n_i$ is the number of molecules of molecular weight $M_i$.

TABLE 1. *Comparison of number-average molecular weights of dextrans obtained by various methods, using gentiobiose as a standard*

| Sample | Scales | $d$ [a] | Somogyi $PO_4$ | $d$ [a] | Somogyi $CO_3$ | $d$ [a] | Folin-Wu | $d$ [a] | HCN | $d$ [a] | Mean |
|---|---|---|---|---|---|---|---|---|---|---|---|
| 1 | 45,600 | +3.64 | 44,100 | +0.23 | 40,800 | −7.27 | 43,900 | −0.23 | 45,800 | +4.09 | 44,000 |
| 2 | 42,000 | −2.78 | 45,300 | +4.86 | 40,900 | −5.32 | 46,100 | +6.71 | 41,600 | −3.70 | 43,200 |
| 3 | 40,700 | +1.75 | 40,300 | +0.75 | 40,900 | +2.25 | ..... | ..... | 38,200 | −4.50 | 40,000 |
| 4 | 36,700 | +3.09 | 35,500 | −0.28 | 32,800 | −7.87 | 36,200 | +1.69 | 36,600 | +2.81 | 35,600 |
| 5 | 33,600 | −1.75 | 34,700 | +1.46 | 31,600 | −7.60 | 35,300 | +3.22 | 35,700 | +4.39 | 34,200 |
| 6 | 73,600 | −0.14 | ..... | ..... | 71,700 | −2.71 | 76,400 | +3.66 | 73,000 | −0.95 | 73,700 |
| 7 | 33,800 | +1.20 | 34,900 | +4.49 | 31,400 | −5.99 | ..... | ..... | ..... | ..... | 33,400 |
| 8 | 19,200 | −1.54 | 20,200 | +3.59 | 17,700 | −9.23 | 20,900 | +7.18 | ..... | ..... | 19,500 |
| 9 | 30,500 | −2.24 | 32,000 | +2.56 | 29,700 | −4.81 | 32,500 | +4.17 | ..... | ..... | 31,200 |
| 10 | 33,600 | −4.82 | 36,500 | +3.40 | 35,700 | +1.13 | ..... | ..... | ..... | ..... | 35,300 |
| 11 | 33,600 | −1.47 | 33,900 | −0.59 | 34,700 | +1.76 | ..... | ..... | ..... | ..... | 34,100 |
| Average | | −0.46 | ..... | +2.05 | ..... | −4.15 | ..... | +3.77 | ..... | +0.36 | ..... |

[a] Percentage deviation from arithmetic mean.

have like reducing powers, workers in other laboratories developed analytical procedures based on an isomaltose standard. A group at the Commercial Solvents Corp. applied Somogyi's method [11] to dextran and isomaltose. With a 20-min heating period they found that 1 ml of 0.005 *N* copper reagent is equivalent to 0.222 mg (or 0.000649 millimoles) of isomaltose [12]. Recently, the Northern Regional Research Laboratory, U. S. Department of Agriculture, kindly furnished us a sample of substantially pure but amorphous isomaltose. A study with the Somogyi phosphate method revealed that the reducing power of this sample of isomaltose was only 94 percent that of gentiobiose. A lower reducing power for the disaccharide having the alpha configuration is in accord with the relative reducing power of maltose and cellobiose. Because dextran and isomaltose have the alpha glucoside structure, whereas gentiobiose has the beta structure, isomaltose would be preferred as a reference compound. Nevertheless, one hesitates to standardize a method on an amorphous sugar. For this reason, it seems desirable to select an arbitrary factor until pure crystalline isomaltose is generally available for use in standardization. The average of our values for the reduction equivalents of isomaltose and gentiobiose is 0.00065 millimole of sugar for each milliliter of 0.005 *N* reagent. This is close to that obtained by the group at Commercial Solvents Corp. for isomaltose. Use of this figure gives the following equation for converting copper-reducing values obtained by the Somogyi method to molecular weight: $M_n = w/(V \times 0.00065)$, where $M_n$ is the number-average molecular weight of the dextran, $w$ is the weight of sample in milligrams, and $V$ is the net titration in milliliters of 0.005 *N* solution.

## 2. Experimental Procedures

### 2.1. Preparation of Samples

#### a. Gentiobiose

Gentiobiose methyl alcoholate was prepared by the method described on page 463 of reference 13. The alcoholate was converted to the pure anhydrous beta modification of sugar by dissolution in water, followed by evaporation of the water and alcohol under reduced pressure. The resulting sirup crystallized spontaneously. The material was recrystallized by dissolving in water, concentrating the solution to about 90-percent total solids, adding 5 parts of methyl cellosolve, and seeding with β-D-gentiobiose crystals. The crystals that formed were separated, washed with methyl cellosolve, and dried under reduced pressure at 60° C. At equilibrium $[\alpha]_D^{20}$ was found to be +9.60 (water, C=2)[4] in agreement with the reported value of +9.6.

#### b. Isomaltose

The isomaltose was supplied by Allene Jeanes of the Northern Regional Research Laboratory. It was a carefully purified amorphous sample originally prepared from the octaacetate. It contained by analysis 41.1 percent of carbon and 6.6 percent of hydrogen. The carbon content corresponds to a product containing 97.6 percent of the anhydrous disaccharide. Hence the dry weight of the material used for the determination of reducing power was based on the assumption that the material contained 2.4 percent of moist ·re.

#### c. Dextran samples

The samples of clinical dextran received in powdered form were dissolved in water, filtered, and lyophilized (freeze dried). Dextran received in "saline" solution was purified by two precipitations with methanol. The resulting material was dissolved in water, filtered, and lyophilized. For the analytical measurements lyophilized samples were placed in tared volumetric flasks and dried to constant weight at room temperature under less than 0.1-mm Hg pressure in a desiccator connected with a dry-ice–acetone trap. After the weight of the dry sample had been determined, water was added and the solution was made to volume. For the analyses, suitable quantities of the solution were transferred with a pipette to the reaction tubes or flasks.

### 2.2. Modified Scales Method

The reagents and procedure were the same as those given on page 189 of reference 13, except that a

[4] 2 grams of gentiobiose dissolved in water and made up to 100 ml.

TABLE 2. *Reducing values of gentiobiose by the modified Scales method* [7]

(10-min boiling time)

| Sample | Net titration 0.04 *N* iodine | Sugar/ml of titration | |
|---|---|---|---|
| *mg* | *ml* | *mg* | *Millimoles* |
| 9.93 | 5.98 | 1.661 | 0.00485 |
| 14.98 | 8.94 | 1.676 | .00490 |
| 19.86 | 11.78 | 1.686 | .00493 |
| 24.91 | 14.64 | 1.702 | .00497 |
| 29.96 | 17.39 | 1.723 | .00503 |

10-min boiling time was used in place of 6 min. The reduction values found for gentiobiose are given in table 2.

With samples of gentiobiose the reducing power changed with concentration. Hence a curve was made by plotting the millimoles gentiobiose per milliliter of 0.04 *N* reagent with respect to the net titration in milliliters. Readings from this curve were used as factors to convert the net titrations obtained with dextran samples to gentiobiose equivalents. The following formula was used to convert the results obtained with clinical dextran to molecular weights: $M_n = w/(V \times f)$, where $w$ is the weight of sample in milligrams, $f$ is the millimoles of gentiobiose equivalent to each milliliter of the titration read from the curve, and $V$ is the net titration in milliliters of 0.04 *N* solution. Some results obtained with clinical dextran samples are given in table 3.

TABLE 3. *Number-average molecular weights of clinical dextrans obtained with modified Scales method*

(Boiling time 10-min; total heating period 14 min)

| Dextran sample number | *w*, weight of sample | *V*, net titration 0.04 *N* solution | *f*, millimoles of gentiobiose per milliliter | $M_n$ |
|---|---|---|---|---|
| | *mg* | *ml* | | |
| L-1 | 977.0 | 10.37 | 0.00491 | 19,200 |
| | 978.0 | 10.44 | .00492 | 19,000 |
| B-742 | 1001.8 | 6.10 | .00486 | 33,800 |
| | 982.6 | 6.00 | .00484 | 33,800 |
| R-2 | 983.6 | 6.64 | .00486 | 30,500 |
| | 977.0 | 6.61 | .00486 | 30,400 |
| 84649A | 981.2 | 4.47 | .00483 | 45,400 |
| 84657A | 995.1 | 4.47 | .00483 | 46,100 |
| | 1013.4 | 4.57 | .00483 | 45,900 |
| 84668A | 881.2 | 4.98 | .00484 | 36,600 |
| S-155 | 1026.3 | 6.33 | .00486 | 33,400 |
| | 984.0 | 5.82 | .00485 | 34,900 |
| C8C275 | 1004.4 | 6.19 | .00486 | 33,400 |
| | 980.0 | 6.09 | .00485 | 33,500 |
| C8C281 | 1002.6 | 6.07 | .00485 | 34,000 |
| | 1000.0 | 6.22 | .00486 | 33,100 |
| NBS-C8 | 1032.1 | 5.24 | .00484 | 40,700 |
| | 1033.3 | 5.26 | .00484 | 40,600 |

## 2.3. Somogyi Phosphate Method

The procedure and reagents used were essentially the same as those described by Somogyi [11] but are repeated in part, since the original article gives certain alternative procedures.

The alkaline copper reagent was prepared from 70.6 g of $Na_2HPO_4.12H_2O$, 40 g of Rochelle salt, 100 ml of *N* NaOH solution, and 80 ml of solution containing 8 g of $CuSO_4.5H_2O$, 180 g of $Na_2SO_4$, and water to make 1 liter. For some of the measurements a measured volume of the sugar solution was heated with an equal volume of the copper-phosphate solution. After cooling, a precisely measured amount of a standard potassium iodate solution and an appropriate amount of potassium iodide and sulfuric acid was added, and after complete oxidation of the cuprous copper the residual free iodine was titrated with 0.005 *N* sodium thiosulfate. In other measurements the "combined" copper reagent was used. This reagent is prepared by incorporation of the requisite quantity of potassium iodate in the alkaline copper solution. Two concentrations were used; one contained 2 ml and the other 1 ml of *N* potassium iodate per 100 ml of the combined copper reagent.

The analyses were made in 25×250-mm test tubes in groups of eight. Five-milliliter quantities of the solutions containing from 0.002 to 0.01 millimoles of gentiobiose, isomaltose, or dextran, or 5 ml of water for blank measurements, were transferred to the test tubes. Each sample was mixed with 5 ml of the copper reagent. When the "combined" reagent was employed, its volume was measured precisely. The tubes were closed with funnel-shaped stoppers and placed in a rack suspended in a boiling-water bath. After 25 min the rack and tubes were transferred to a cold-water bath and brought to room temperature. The tubes were then treated separately and successively. In measurements using the unmodified copper reagent a precisely measured volume of 0.01 *N* $KIO_3$ was pipetted into the tube; in those made with the "combined" alkaline copper reagent this step was omitted, since the reagent already contained the necessary potassium iodate. In any case, the sides of the tube were washed down with 1 or 2 ml of 2.5-percent potassium iodide without agitation to minimize oxidation by air. Immediately following the addition of potassium iodide, 1.5 ml of 2 *N* $H_2SO_4$ was added with shaking, so that the contents of the tube were mixed quickly and acidified. When all the cuprous oxide was dissolved the excess iodine was titrated with 0.005 *N* sodium thiosulfate and a starch indicator. The titer of the sample subtracted from the titer of the blank containing a like quantity of potassium iodate is the net titration. This corresponds to the reducing sugar present.

Prior to the selection of a heating period of 25 min, the effect of boiling time on the reaction was studied. The measurements reported in table 4

TABLE 4. *Effect of the length of the heating period on reduction of 2-mg samples of gentiobiose by the Somogyi phosphate method*

[Combined copper-iodate solution]

| Time of boiling | Net titration 0.005N thiosulfate | Milligram of gentiobiose per milliliter of net titration |
|---|---|---|
| *min* | *ml* | |
| 5 | 7.38 | 0.271 |
| 7.5 | 8.24 | .243 |
| 10 | 9.10 | .220 |
| 12.5 | 9.22 | .217 |
| 15 | 9.23 | .217 |
| 20 | 9.38 | .213 |
| 25 | 9.50 | .211 |
| 30 | 9.42 | .212 |

show that the amount of reduction is substantially constant after 20 min.[5]

The results obtained by the Somogyi-phosphate method with gentiobiose and isomaltose are given in tables 5 and 6. The amount of reduction was found to be roughly proportional to the amount of sugar, in the range covered by net titrations from 6 to 13 ml. Smaller samples gave slightly lower factors and larger samples higher factors. For this reason the weights of the dextran samples were adjusted to give titrations of from 6 to 13 ml, and the same factor was used for all samples. The results obtained with clinical dextrans, using a 25-min heating period, are given in table 7. The molecular weights based on the gentiobiose standard were obtained by the formula

$$M_n = \frac{w}{V \times 0.216/342.3} = \frac{w}{V \times 0.000631}$$

in which $M_n$ is the number-average molecular weight, $w$ is the weight of the sample in milligrams, $V$ is the net titration in milliliters of 0.005 $N$ reagent, and 0.000631 is the reduction equivalent of dextran expressed in millimoles per milliliter of reagent. Multiplication of the results by 0.939 gives values based on isomaltose, and multiplication by 0.969 gives values based on an empirical factor that is the mean of the values found for isomaltose and gentiobiose. This empirical factor is in agreement with a value found by Commercial Solvents Corp. for isomaltose.

TABLE 5. *Reduction equivalents by the Somogyi phosphate reagent determined with gentiobiose*

| Sample gentiobiose | Net titration 0.005 $N$ solution | Milligram of sugar per milliliter of titration |
|---|---|---|
| Separate addition of iodate | | |
| *mg* | *ml* | |
| 1.2 | 5.80 | 0.207 |
| 1.4 | 6.66 | .210 |
| 1.8 | 8.47 | .213 |
| 1.8 | 8.49 | .212 |
| 2.2 | 10.28 | .214 |
| 2.2 | 9.55 | .230 |
| 2.2 | 10.25 | .215 |
| 2.6 | 12.09 | .215 |
| 2.6 | 12.06 | .216 |
| 2.6 | 12.06 | .216 |
| 3.0 | 13.60 | .221 |
| 3.0 | 13.70 | .219 |
| 3.0 | 13.67 | .219 |
| Mean | | 0.216 |
| Combined copper and iodate solution | | |
| 1.0 | 4.63 | 0.216 |
| 1.5 | 6.95 | .216 |
| 2.0 | 9.39 | .213 |
| 2.5 | 11.53 | .217 |
| 3.0 | 13.62 | .220 |
| Mean | | 0.216 |

From a somewhat similar study [12] the group at C.S.C. selected a heating period of 20 min.

TABLE 6. *Reduction equivalents of the Somogyi combined copper phosphate-iodate reagent determined with isomaltose*

(25-min boiling time)

| Isomaltose | Net titration 0.0005 $N$ solution | Milligram of isomaltose per milliliter net titration |
|---|---|---|
| *mg* | *ml* | |
| 0.567 | 2.52 | 0.225 |
| 1.133 | 4.89 | .232 |
| 1.700 | 7.17 | .237 |
| 2.267 | 9.92 | .229 |
| 2.834 | 12.55 | .226 |
| Average | | 0.230 |

TABLE 7. *Number-average molecular weights of clinical dextrans determined by the Somogyi phosphate method (gentiobiose standard)*

(Heating time 25 min)

| Dextran sample number | Weight of sample | Titration 0.005 $N$ thiosulfate | $M_n$[a] |
|---|---|---|---|
| | *mg* | *ml* | |
| 84649A | 242.8 | 8.79 | 43,800 |
| | 241.6 | 8.64 | 44,300 |
| 84357A | 252.8 | 8.81 | 45,500 |
| | 256.7 | 9.04 | 45,000 |
| 84668A | 245.2 | 10.95 | 35,500 |
| | 244.5 | 10.92 | 35,500 |
| S-155 | 248.9 | 11.26 | 35,000 |
| | 252.1 | 11.66 | 34,300 |
| B-742 | 251.8 | 11.44 | 34,900 |
| | 253.8 | 11.51 | 34,900 |
| R-2 | 252.9 | 12.46 | 32,300 |
| | 252.0 | 12.54 | 31,800 |
| L-1 | 158.5 | 12.41 | 20,200 |
| | 158.6 | 12.44 | 20,200 |
| CSC275 | 269.8 | 11.67 | 36,600 |
| | 274.6 | 11.95 | 36,400 |
| CSC281 | 266.7 | 12.45 | 33,900 |
| | 263.7 | 12.35 | 33,800 |
| NBS-C8 | 270.0 | 10.69 | 40,000 |
| | 264.9 | 10.37 | 40,500 |
| Polyglucose,[b] P-128-56 | 248.4 | 6.20 | 62,900 |
| | 246.8 | 6.21 | 63,000 |
| 84659-62A | 266.4 | 7.78 | 54,300 |
| | 257.8 | 7.61 | 53,700 |

[a] $M_n = w/(V \times 0.000631)$.
[b] This substance, a polysaccharide prepared by chemical means, is included, even though it is not a true dextran.

## 2.4. Somogyi Carbonate Method [14]

Reagents and procedure were the same as those given in reference 15, except that a 30-min heating time was used.

The procedure was standardized by use of definite amounts of gentiobiose. Because the reduction equivalents, given in table 8, did not show any definite trend with change in concentration, the average reduction equivalent was used rather than a separate factor for each titration value. That is 1 ml of 0.005 $N$ thiosulfate was found, on the average, to be equivalent to 0.214 mg of gentiobiose. Some results obtained with dextran samples are given in table 9. The number-average molecular weights were obtained from the formula $M_n = w/(V \times 0.000625)$, in which $w$ is the weight of the dextran sample in milligrams, and $V$ is the net titration in milliliters of 0.005 $N$ thiosulfate.

TABLE 8. *Somogyi carbonate method*

Reduction equivalents of varying amounts of gentiobiose (30-min heating period)

| Gentiobiose | Net titration 0.005 *N* thiosulfate | Milligram of gentiobiose per milliliter of 0.005 *N* solution |
|---|---|---|
| *mg* | | |
| 1.2434 | 6.03 | 0.206 |
| 2.4868 | 11.43 | .218 |
| 2.4868 | 11.73 | .212 |
| 2.7977 | 12.42 | .225 |
| 3.1085 | 14.21 | .219 |
| 1.1389 | 5.22 | .218 |
| 1.7084 | 8.27 | .207 |
| 2.2778 | 11.02 | .207 |
| 2.8473 | 13.10 | .217 |
| 2.8473 | 13.13 | .217 |
| 1.1389 | 5.25 | .217 |
| 1.2470 | 5.73 | .218 |
| 1.8705 | 9.06 | .206 |
| 2.4940 | 11.73 | .213 |
| Mean | | 0.214 |

TABLE 9. *Number-average molecular weights of clinical dextrans determined by the Somogyi carbonate method [14]*

(Heating time 30 min)

| Dextran sample number | Weight of sample | Titration 0.005 *N* thiosulfate | $M_n$[a] |
|---|---|---|---|
| | *mg* | *ml* | |
| 84649A | 287.5 | 11.27 | 40,800 |
| 84657A | 286.6 | 11.21 | 40,900 |
| 84668A | 310.5 | 15.16 | 32,800 |
| S-155 | 302.0 | 15.90 | 30,400 |
| | 281.5 | 13.72 | 32,800 |
| B-50074 | 274.3 | 6.12 | 71,700 |
| L-1 | 148.1 | 13.40 | 17,700 |
| R-2 | 147.6 | 7.95 | 29,700 |
| B-742 | 288.7 | 14.71 | 31,400 |
| NRC-2 | 99.0 | 12.07 | 13,100 |
| | 99.0 | 12.06 | 13,100 |
| NRC-3 | 197.2 | 7.30 | 43,200 |
| | 204.0 | 7.64 | 42,700 |
| NRC-4 | 186.0 | 4.16 | 71,500 |
| | 202.6 | 4.62 | 70,200 |
| 84657A | 274.5 | 10.45 | 42,000 |
| | 270.4 | 10.30 | 42,000 |
| CSC275 | 276.2 | 12.80 | 35,100 |
| | 266.0 | 11.70 | 36,400 |
| CSC281 | 268.2 | 12.40 | 34,600 |
| | 267.9 | 12.32 | 34,800 |
| NBS-C8 | 268.3 | 10.35 | 41,500 |
| | 270.2 | 10.76 | 40,200 |
| NRC-2[b] | 89.1 | 10.25 | 13,900 |
| | 90.3 | 10.23 | 14,100 |
| NRC-2[c] | 97.1 | 10.95 | 14,200 |
| | 96.5 | 10.78 | 14,300 |

[a] $M_n = w/(V \times 0.000625)$.
[b] Reclaimed from sample NRC-2 after dissolution in water, precipitation with methanol, dissolution again in water, treated with vegetable char, filtered, and the filtrate lyophilized.
[c] Same as NRC-2-A, except no char treatment was used in its preparation.

## 2.5. Folin-Wu Method [16]

The method of Folin and Wu was studied with the view that it might be useful for routine determinations in the hands of laboratory technicians. The procedure was essentially that described on page 198 of reference 17. The color measurements were made with both Klett-Summerson and Lumetron photoelectric colorimeters. As with other microreducing sugar methods, it is essential that the analyst standardize his procedure by measurements of the reducing power of a series of standards covering the range to be used. Table 10 gives some results obtained with anhydrous dextrose and gentiobiose.

TABLE 10. *Percentage of transmission of typical standards for the Folin and Wu method*

(No. 42 blue filter approximate spectral range 400 to 465 mμ) (Percentage of transmission of blank is 100)

| Dextrose | | Gentiobiose | |
|---|---|---|---|
| Milligrams of sugar in 100 milliliters | Transmission | Milligrams of sugar in 100 milliliters | Transmission |
| | *Percent* | | *Percent* |
| 5 | 85.2 | 10.5 | 86.5 |
| 7.5 | 78.5 | 17.1 | 73.4 |
| 10 | 70.3 | 25.0 | 63.7 |
| 15 | 57.2 | 34.2 | 51.0 |
| 20 | 46.5 | 42 | 41.3 |
| 25 | 37.7 | 50 | 35.6 |
| 30 | 31.1 | ... | ... |

In the analysis of dextrans, a standard, ordinarily gentiobiose, was always included in each set of determinations. Thus, the small variation in reducing power from one set to another, as well as from day to day, is compensated for by the application of suitable corrections. The dextrose equivalent or the gentiobiose equivalent for dextran is then obtained by calculation, or by graphic means. It has been our experience that it is desirable to employ standards yielding a transmission reading close to that obtained for the dextran under analysis. Some values obtained by this method are included in table 1.

---

The authors express their appreciation to the National Research Council and to the Office of the Surgeon General for their support and cooperation in this investigation. They are also indebted to the several producers of dextran, and to the staff of the Northern Regional Research Laboratory, U. S. Department of Agriculture, for providing samples of dextran, analytical methods and data. The collaboration of S. G. Weissberg and his associates at the Bureau has been most helpful and is gratefully acknowledged.

## 3. References

[1] H. L. A. Tarr and H. Hibbert, Can. J. Research **5,** 414 (1931).
[2] T. H. Evans and H. Hibbert, (Bacterial Polysaccharides) Advances in Carbohydrate Chemistry, **2,** p. 203, (Academic Press, Inc., New York, N. Y., 1946).
[3] M. Stacey, (The Chemistry of Mucopolysaccharides and Mucoproteins), Advances in Carbohydrate Chemistry, **2,** p. 161, (Academic Press, Inc., New York, N. Y., 1946).
[4] A. Jeanes, Dextran -a selected bibliography, U. S. Department of Agriculture, Northern Regional Research Laboratory, Peoria, Illinois (1950).
[5] A. Grönwall and B. Ingelman, Nature **155,** 45 (1945).
[6] K. H. Meyer, G. Noelting, and P. Bernfeld, Helv. Chim. Acta **31,** 103 (1948).
[7] H. S. Isbell, W. W. Pigman, and H. L. Frush, J. Research NBS **24,** 241 (1940) RP1282.

[8] H. S. Isbell, Report of working conference on dextran, Peoria, Ill., July 9, 1951, sponsored by National Research Council, Subcommittee on Shock and Northern Regional Research Laboratory.
[9] S. G. Weissberg and H. S. Isbell, Molecular properties of plasma substitutes, NBS Report 1160 (Sept. 24, 1951).
[10] H. S. Isbell, Science **113,** 532 (1951).
[11] M. Somogyi, J. Biol. Chem. **160,** 61 (1945).
[12] Memorandum No. B-50, Commercial Solvents Corporation, Terre Haute, Indiana, Determination of number-average molecular weight of dextran by end-group analysis, January 1952.
[13] Polarimetry, saccharimetry and the sugars, NBS Circular C440, p. 463 (1942).
[14] M. Somogyi, J. Biol. Chem. **70,** 599 (1926).
[15] Official Methods of Analysis of the Association of Official Agricultural Chemists, 7th ed., p. 513 (1950).
[16] O. Folin and H. Wu, J. Biol. Chem. **38,** 106 (1919).
[17] War Department Technical Manual, TM 8-227, U. S. Government Printing Office, Washington, D. C. (1946).

WASHINGTON, November 14, 1952.

# An Interferometer Procedure Applied to the Study of the Chemical Durability of Silicates, Enamels, and Metals

Robert G. Pike and Donald Hubbard

The chemical durability of quartz, fused silica, obsidian, flint, opal, and glass were determined by the interferometer method and the results interpreted in the light of the Donnan theory of membrane equilibria. A more sensitive test of the same phenomena is the uneven distribution of migratable ions, as shown by the $Ag^+Br^-$ titration. The tests used are sensitive enough to differentiate between the different types of silica and may be applicable to the study of the chemical weathering characteristics of all natural silicates. Results of preliminary experiments on enamels and metals show that these tests may serve as indicators of the corrosive resistance of these materials under a wide range of conditions

## 1. Introduction

The results reported in earlier publications have demonstrated the utility of the interferometer procedure for determining the chemical durability of glasses, particularly in the study of the voltage anomalies of the glass electrode [1, 2].[1] These results suggested that the same procedure could be used to determine the relative chemical durability of natural minerals and thus throw some further light on the probable mechanism and rate of chemical weathering in nature.

Another investigation has also been described which shows that there is an uneven distribution of migratable ions at a glass-solution interface in accordance with the dictates of the Donnan theory of membrane equilibria [3]. In view of these findings it seemed desirable to determine if the same principles could be applied to some of the natural silicates.

With these objectives in mind, quartz, fused silica, opal, obsidian, flint, and pitchstone were chosen for study. The glasses, Pyrex brand chemical ware 7740 (hereafter referred to as Pyrex) and Corning 015, on which many tests had previously been made, were also included in the study as control and comparative samples.

The results obtained in the first experiments suggested that the interferometer procedure might have even wider applicability. Therefore, the, the method was extended to the study of porcelain enamels and metals.

## 2. Experimental Procedure

### 2.1. Interferometer Method

When available, specimens about ½ by ¾ in. were ground flat on a cast-iron lap with fine alumina powder and polished on a wax wheel with levigated alumina. These specimens were treated for chemical durability by the interferometer procedure [1, 2]. This consists of immersing the sample one-half its depth in a solution of known pH covered with an oil layer to prevent evaporation of the water, and maintained at a temperature of 80° C for definite periods of time. Using the unexposed portion of the sample as a reference plane, the attack on the exposed surface is measured by determining the displacement of the interference fringes with the conventional Pulfrich viewing apparatus, using an unfiltered helium lamp for illumination. Swelling of the surface is plotted in all figures as negative attack. To make the results comparable with previous publications [1, 2, 3, 6] the exposures were made at 80°±0.2° C for 6 hr to Britton-Robinson universal buffer solutions [4] (hereafter called Britton buffers) ranging from pH 2 to pH 11.8, with some exceptions as explained later in the text.

[1] Figures in brackets indicate the literature references at the end of this paper.

### 2.2. Hygroscopicity

The procedure for determining hygroscopicity was that reported in previous publications [6, 2], which consisted of weighing the water sorbed [5] upon exposing about 1.5 g of powdered glass (passed through a U. S. Standard Sieve No. 140) to the high humidity (approximately 98 percent) maintained by a saturated solution of $CaSO_4.2H_2O$. To insure speed in obtaining equilibrium and uniformity throughout the humidity chamber, the walls were lined with a blotter wick, and the atmosphere of the closed system kept circulating with a fan. The samples were exposed for 1- and 2-hr periods at 25° C and the results reported as milligrams of water sorbed per cubic centimeter of sample.

### 2.3. Uneven Distribution of Migratable Ions

For the experiments on the uneven distribution of migratable ions between the outer solution and the silica rich layer of the specimens, samples of approximately 10 g were prepared by being crushed and passed through a No. 50 and retained on a No. 140 U. S. Standard Sieve. They were then leached for various periods of time at pH 4.1 and 80° C with occasional agitation. After rinsing and decanting the samples twice, they were treated by agitation for 5 min in 50 ml of saturated $Ag(NH_3)_2$ Br solution [3]. The samples were then separated by decantation from the liquid phase. The sample and liquid phases were acidified with concentrated $H_2SO_4$ and titrated

potentiometrically for excess $Ag^+$ remaining in the gelatinous silica-rich surface and for the excess $Br^-$ ions appearing in the outer solution [3].

### 2.4. Materials

Flint samples were cut from the black center portion of a nodule from Travis County, Tex. Pitchstone was from Georgetown, Colo. Obsidian was a typical natural black glass. These three materials were obtained through the courtesy of Edward P. Henderson at the United States National Museum. Quartz samples were cut from a near optical grade crystal. Fused silica was commercial optical grade. Opal from Nevada was obtained through Wards Natural Science Establishment. Pyrex was chemical glassware 7740. Enameled metalware samples were regular commercial grade, furnished by the Enamel Metals Section of the National Bureau of Standards. Metal specimens were commercial samples.

## 3. Results and Discussion

### 3.1. Silicates

The extent of surface alteration (swelling or attack) at various pH values has been demonstrated with certain glasses [1, 2, 3]. The swelling has been rationalized in terms of the Donnan theory of membrane equilibria [3], and the attack in terms of rate of solution of silicates. In the figures the amount of swelling is plotted as negative attack. Quartz, flint, obsidian, and fused silica show no detectable swelling or attack at pH values below 9.5. Above this value, the rate of attack increases to ½ fringe at pH 11.8 for fused silica. The difference between the fused silica and crystalline quartz is easily demonstrated (fig. 1 data given in table 1). The fact that obsidian, a natural glass, falls between the two in chemical durability is perhaps surprising but may possibly be a result of a high-alumina content characteristic of obsidian glass. The attack on flint and crystalline quartz was not detectable at pH 11.8 after a 6-hr exposure. However, there is a detectable attack after 24 hr.

A sample of the crystalline quartz was also given an exposure of 2 weeks at 80° C in pH 4.1 and showed a definite swelling at the contact of the solution oil surface. Longer exposure times could be used if a method could be found to prevent diffusion of the water through the oil layer.

In order to show more clearly the relative resistance to attack in strong alkalies, the samples were also treated for 6 hr in 5 percent NaOH at 80° C and the results listed in table 1. (Because of the very low resistance of opal it was treated for only 15 min and the results extrapolated to 6 hr.)

The Corning 015, a glass of poor chemical durability, is included as a means of comparison with previous tests on optical glasses.

The results obtained on opal are the most interesting of the group. Swelling of nearly 1 fringe is obtained at the lower limit of the tests (pH 2) and continues at that rate to about pH 8 and from there to pH 11.8 the swelling rapidly changes to an attack of 3½ fringes. It was noted during the tests that the swelling that took place in the solution disappeared

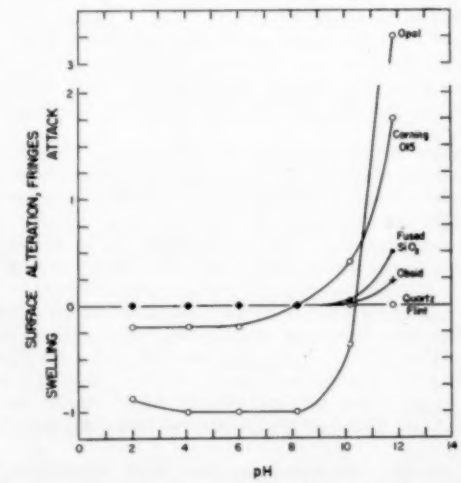


FIGURE 1. *Relative chemical durabilities over the range* pH *2 to* pH *11.8 after exposure for 6 hours at 80° C in Britton buffers.*

TABLE 1. *Chemical durability, hygroscopicity, and interfacial uneven distribution of migratable ions for silicate materials*

| Material | Surface alterations for exposures of 6 hr, 80° C at pH— | | | | | | | Water sorbed in— | | Excess $Ag(NH_3)_2^+$ ions in surface of specimens leached at pH 4.1, 80° C in— | | | | |
|---|---|---|---|---|---|---|---|---|---|---|---|---|---|---|
| | 2 | 4.1 | 6.0 | 8.2 | 10.2 | 11.8 | 5% NaOH | 1 hr | 2 hr | 0 hr | 6 hr | 24 hr | 72 hr | 144 hr |
| | *Fringes* | *Fringes* | *Fringes* | *Fringes* | *Fringes* | *Fringes* | *Fringes* | *mg/cm²* | *mg/cm²* | *M-eq/g* | *M-eq/g* | *M-eq/g* | *M-eq/g* | *M-eq/g* |
| Quartz | ND[a] | ND | ND | ND | ND | ND | ND | 4.2 | 7.9 | <[b]0.1×10⁻⁴ | −0.4×10⁻⁴ | ..... | 0.6×10⁻⁴ | 1.0×10⁻⁴ |
| Flint | ND | ND | ND | ND | ND | ND | 1/10 A[c] | ... | ... | ... | ... | ..... | ..... | ..... |
| Fused $SiO_2$ | ND | ND | ND | ND | D[d], A | ½ A | 1 A | 4.2 | 7.8 | <0.1 | 0.9 | ..... | 1.0 | 1.1 |
| Obsidian | ND | ND | ND | ND | D, A | • ¼−A | 1 A | 8.6 | 14.2 | <.1 | .6 | ..... | 0.9 | 1.5 |
| Pitchstone | .... | .... | .... | .... | ... | ... | 1 A | ... | ... | ... | ... | ..... | ..... | ..... |
| Corning 015 | 1/10−S[f] | 1/10−S | 1/10−S | SC[e] | ¼+A | 2−A | ... | 115 | 230 | 5.8 | 23 | 30.6×10⁻⁴ | 39.3 | 30.2 |
| Pyrex | ND | ND | ND | D, A | ¼−A | 1¾ A | 2½ A | .... | ... | ..... | ..... | ..... | ..... | ..... |
| Opal($SiO_2$.$nH_2O$) | [b] ¾+S | 1 S | 1 S | 1 S | ½−S | 3¼ A | 24 A | 39 | 61 | 32.3 | 132 | ..... | 166 | 167 |

[a] ND, not detectable.
[b] <, less than the smallest titrateable increment.
[c] A, attack.
[d] D, dectable, but not measurable.
[e] ¼−, slightly less than ¼.
[f] S, swelling.
[g] SC, surface cut at the oil-buffer boundary.
[h] ¾+, slightly more than ¾.

as the specimen was exposed to the air. Therefore, additional tests were made, the results of which are shown in figure 2 (data given in table 2), where attack is plotted against the number of hours after removal of the samples from the solution. It can be seen that after a period of 5 hr the initial swelling of more than 1½ fringes has changed to an appreciable attack, which leads to the conclusion that both solution and swelling had occurred during exposure. In figure 1 it can be seen that swelling is more rapid than attack for all values below pH 10.2. This is shown more strikingly in figure 3 (data given in table 3), where surface alteration (attack, swelling) is plotted against time of exposure at pH 4.1. Also shown are the changes in the surface alterations of the same specimens, taken from the buffer and exposed to the atmosphere for varying lengths of time. From this curve it appears that after about 50 hr the amount of swelling approaches a maximum. In other words, the extent of attack is equal to or greater than the extent of swelling. If the swelling as noted in these curves is caused by the uneven distribution of migratable ions, the osmotic pressure should be

TABLE 2. *Surface alteration of the two specimens of opal upon exposure to air after immersion in Britton buffer at* pH *4.1 for 24 hours at 80° C*

| Sample number | Surface alteration in— | | | | | |
|---|---|---|---|---|---|---|
| | 0 hr | 2 hr | 6 hr | 9 hr | 24 hr | 48 hr |
| | *Fringes* | *Fringes* | *Fringes* | *Fringes* | *Fringes* | *Fringes* |
| 1 | 1½ S• | ¾ S | 1/10 A | 1/2—A | ¼+A | 1/2+A |
| 2 | 2—S | ..... | 1/10 A | ..... | 1/2—A | 1/2—A |

• Symbols explained in table 1.

TABLE 3. *Effect of time on the swelling of opal in Britton buffer at* pH *4.1 and 80° C, and the surface alteration after removal from the buffer and exposure in air*

| Hours of exposure in air | Surface alteration after exposure in buffer for— | | | | | |
|---|---|---|---|---|---|---|
| | 2 hr | 4 hr | 6 hr | 12 hr | 24 hr | 48 hr |
| | *Fringes* | *Fringes* | *Fringes* | *Fringes* | *Fringes* | *Fringes* |
| | ¾ S • | 1—S | 1+S | 1½—S | 1½+ S | 1¾ S |
| | Surface alteration after removal from buffer | | | | | |
| 0 | ¾ S | 1—S | 1+S | 1½—S | 1½+S | 1¾ S |
| 2 | ¼ S | ..... | ½—S | ½+S | ¾ S | ½+S |
| 4 | DS | ..... | 1/10 S | ..... | ..... | ..... |
| 6 | ..... | ..... | ..... | ..... | 1/10 A | ..... |
| 8 | DA | ..... | 1/10 A | ..... | ..... | ..... |
| 10 | ..... | ..... | ..... | ..... | ¼ A | ¾—A |
| 12 | ..... | ..... | ..... | 2/10 A | ..... | ..... |
| 20 | DA | ..... | 1/10 A | ..... | ..... | ¾—A |
| 22 | ..... | ..... | ..... | 2/10 A | ¼+A | ..... |
| 36 | ..... | ..... | ..... | ..... | ¼+A | ..... |

• Symbols explained in table 1.

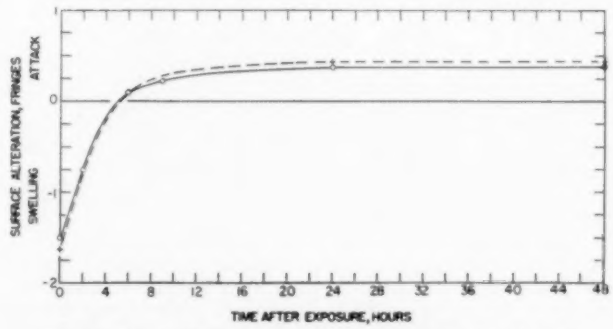


FIGURE 2. *Surface alteration of two specimens of opal in air, after exposure to Britton buffer solution at* pH 4.1 *for 24 hours at 80° C.*

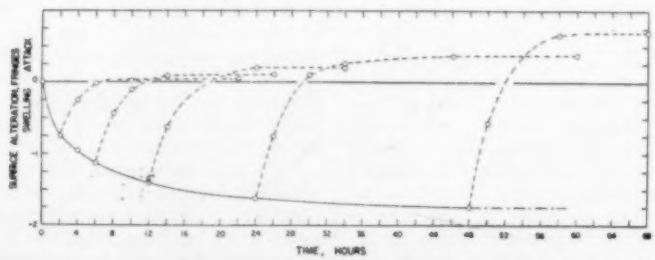


FIGURE 3. *Typical surface alterations of opal with time of exposure in Britton buffer solution at* pH 4.1 *at 80° C followed by exposure in air.*

———— O ————, Surface alteration immed ately after removal from the buffer solution.
..... O ....., Surface alterations after removal from the buffer and exposure to air.

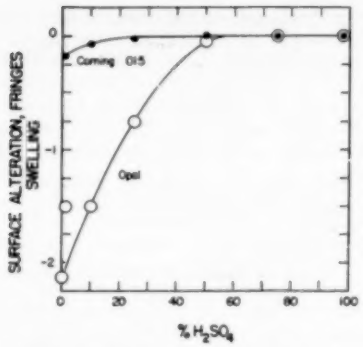


FIGURE 4. *Typical reduction of swelling of opal and Corning 015 by increased concentration of electrolyte, exposed for 6 hours at 80° C.*

TABLE 4. *Surface alteration of opal and Corning 015 glass in sulfuric-acid solutions of various concentrations for 6 hours at 80° C*

| $H_2SO_4$ | Surface alteration | |
|---|---|---|
| | Opal | Corning 015 |
| *Percent* | *Fringes* | *Fringes* |
| 0.1 | 2+S * | 2/10—S |
| 1.0 | 1½ S | 7/10—S |
| 10.0 | 1½ S | 1/10—S |
| 25.0 | ¾ S | DS |
| 50.0 | ND, SC | ND |
| 75.0 | ND, SC | ND |
| 98.0 | ND, SC | ND |

* Symbols explained in table 1.

reduced by high concentrations of electrolytes in accord with the Donnan equation for osmotic pressure [7]. This effect is shown in figure 4 (data given in table 4), where surface alteration of opal and Corning 015 is plotted against concentration of $H_2SO_4$. It can be seen that at 0.1 percent $H_2SO_4$ a swelling of greater than 2 fringes is obtained, and at 65-percent $H_2SO_4$ the amount of swelling has been reduced until it is no longer detectable. It is realized that considering 65-percent $H_2SO_4$ as a high concentration of electrolyte in terms of the Donnan theory of membrane equilibria is questionable and that any one of a number of other explanations could suffice [3].

The hygroscopicity of the samples is plotted in figure 5 (data given in table 1) as water sorbed in $mg/cm^3$ against time in hours. Note that the relative positions of Corning 015 and opal in this figure have been reversed from that in figure 1, indicating that the surface alteration (swelling) of the opal results from some factor other than its hygroscopic property. In other words, hygroscopicity is not a reliable indicator of chemical durability.

In figure 6 (data given in table 1) the excess $Ag(NH_3)_2^+$ ions in milliequivalents per gram (hereafter designated as M-eq/g) appearing in the surface is plotted against time of leaching at pH 4.1 at 80° C. The relative positions of these curves are compatible with those of surface alteration shown in figure 1.

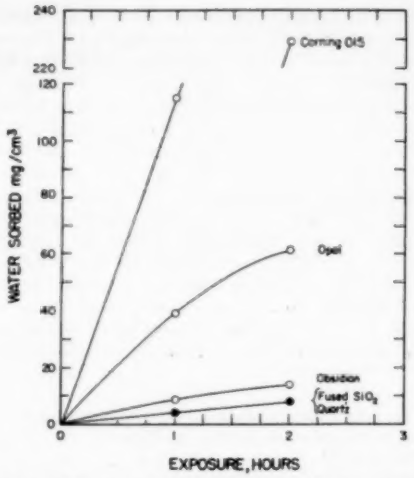


FIGURE 5. *Hygroscopicity (water sorbed) for quartz, fused $SiO_2$, obsidian, opal, and an electrode glass* (Corning 015) *after exposure in an atmosphere of 98-percent relative humidity.*

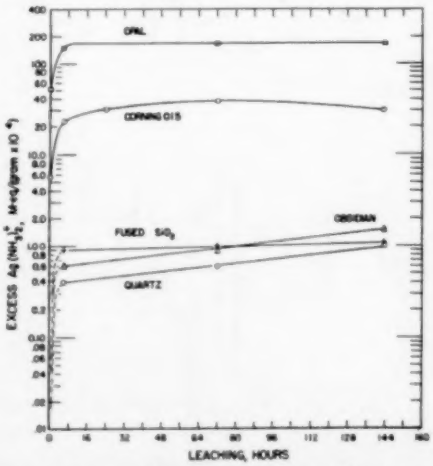


FIGURE 6. *Uneven distribution of migratable ions at the interface between the surface layer and the outer solution after various periods of leaching in Britton buffer at* pH 4.1 *at 80° C using* $Ag(NH_3)_2^+$ *and* $Br^-$ *as the indicator ions.*

This uneven distribution of the migratable ions is caused by the nonmigratable negative charged silicate ions acting as their own semipermeable membrane, and thus causing a definite osmotic pressure across the opal-solution interface.

It is well recognized that chemical attack plays a considerable part in the weathering of rocks and minerals. These tests strongly point out the fact, not always realized, that the weaker acids and bases or even neutral salts may sometimes be a much more destructive force than concentrated solutions. These studies also indicate that another phenomenon, osmosis, plays a very important and persistent role i-

the weathering of numerous rocks and minerals. The interferometer procedure might well be used to study the relative resistance of many of the rock-forming minerals to acids and bases over a much wider time and concentration range than was done here.

### 3.2. Alkali Aggregate Reaction

High-alkali cements are known to react with certain aggregates, particularly opal, used in concrete [8]. This reaction causes a swelling and subsequent deterioration of the concrete structure. Hansen [9] has postulated that the cement paste might act as a semipermeable membrane, which would allow the alkalies to migrate through the concrete and react with the opal. The reaction product would not be capable of diffusing through the hardened cement paste. Thus osmotic pressures would be built up, which could cause disintegration of the concrete. A modification of this hypothesis as advanced by Parsons and Insley [10] suggested that a reaction takes place at the walls of the pores in the concrete to form a membrane impermeable to further migration of alkali silicates. The authors have considered the possibility that the opal grains might act as their own semipermeable membrane. However, the interferometer shows that expansion of the opal itself occurs in the acid and not in the alkaline range. Any expansion in the alkaline range must be because of some reaction products or to osmotic pressures set up through some membrane surrounding the individual opal grain rather than to any Donnan membrane equilibria in the opal itself. Another interpretation of this effect has been advanced by Vivian [11], who believes that alkalies react with opal to form a gel that absorbs water, causing swelling of the gel and subsequent failure of the concrete.

### 3.3. Porcelain Enamels

In figure 7 (data given in table 5) is plotted the chemical durability of three commercial porcelain enamels, a class A acid resistant, a class D acid resistant, and a hot-water tank enamel of a type used in the manufacture of the so-called glass-lined tanks. (Hereafter referred to as glass-lined tank enamel.) [12]. The difference in durability in both the acid and alkaline range can be observed from these curves.

The hygroscopicity of these enamels is shown in figure 8 (data given in table 6) and is seen to be greater than that of Pyrex but much less than that of Corning 015.

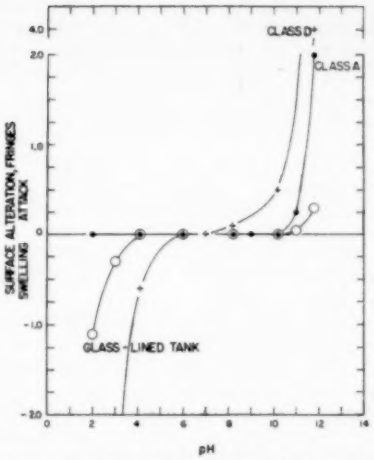


○, Glass-lined tank; ●, class A, and +, class D acid-resistent enamels.

FIGURE 7. *Chemical durability over the range from* pH 2 *to 11.8 of three types of porcelain enamels, after exposure for 6 hours at 80° C in Britton buffers.*

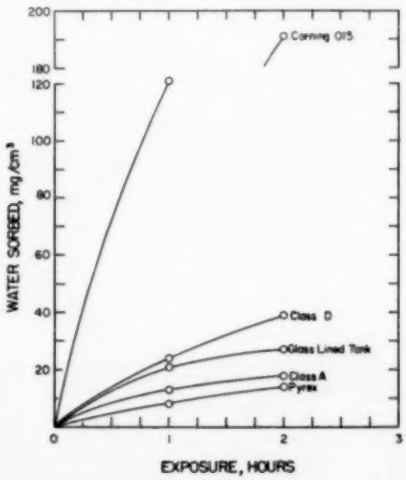


FIGURE 8. *Hygroscopicity (water sorbed) of three typical porcelain enamels compared with two commercial glasses, after exposure to a relative humidity of 98 percent.*

TABLE 5. *Chemical durability of three types of porcelain enamel*

| Enamel | Surface alteration at pH— | | | | | | | | | |
|---|---|---|---|---|---|---|---|---|---|---|
| | 2.0 | 3.0 | 4.1 | 6.0 | 7.0 | 8.2 | 9.0 | 10.2 | 11.0 | 11.8 |
| Acid resistant, class A | *Fringes* • ND | *Fringes* ..... | *Fringes* ND | *Fringes* ND | *Fringes* ..... | *Fringes* ND | *Fringes* ND | *Fringes* ND | *Fringes* ¼ A | *Fringes* 2 A |
| Glass-lined tank | 1+S | ¼+S | ND | ND | ..... | ND | ..... | ND | D A | ¼ A |
| Acid resistant, class D | 144 S | 36 S | ½+S | ND | ND | 1/10 A | ..... | ½ A | ..... | 4 A |

• Symbols explained table 1.

TABLE 6. *Comparison of the hygroscopicities for three types of porcelain enamels and two commercial glasses*

| Specimen | Water sorbed in— | |
|---|---|---|
| | 1 hr | 2 hr |
| Porcelain enamels: | *mg/cm²* | *mg/cm²* |
| Class A, acid resistant | 13 | 18 |
| Glass-lined tank | 21 | 27 |
| Class D, acid resistant | 24 | 39 |
| Glasses: | | |
| Corning 015 | 121 | 191 |
| Pyrex 7740 | 8 | 14 |

The chemical durability of the class A enamel at high concentration of acids is shown in figure 9 (data given in tables 5 and 7), and the repression of swelling of the tank enamel at high concentration of electrolytes is shown in figure 10 (data given in table 8). The uneven distribution of the migratable ions for the class D enamel gave the low value of less than $0.2\times10^{-4}$ M-eq/g with no leach, and the very high value of $415\times10^{-4}$ M-eq/g after 6 hr of leaching at pH 4.1. This value is 46 times greater than for the glass-lined tank enamel and is a very striking example of the sensitivity of this test.

TABLE 7. *Chemical durability of two commercial porcelain enamels in aqueous solutions of* $H_2SO_4$ *and* $CH_3COOH$

| Solution | | | Surface alteration | | | |
|---|---|---|---|---|---|---|
| | | | Class A, acid-resistant | | Glass-lined tank | |
| | $H_2SO_4$ | $CH_3COOH$ | $H_2SO_4$ | $CH_3COOH$ | $H_2SO_4$ | $CH_3COOH$ |
| *Percent* | pH | pH | *Fringes* | *Fringes* | *Fringes* | *Fringes* |
| 0.1 | 1.7 | 2.7 | [a] ND | ND | | |
| 1.0 | 0.75 | 2.5 | ND | ..... | [b] | [b] |
| 10.0 | 0 | ..... | ND | ..... | | |
| 25.0 | −0.62 | ..... | ND | ..... | | |
| 50.0 | −1.49 | 1.3 | ND | ND | ND | ND |
| 75.0 | −2.45 | 0.6 | ND | ND | ND | ND |
| 96.0 | −8.1 | ..... | ND | ..... | ND | ..... |
| 98.0 | ..... | −2.2 | ..... | ND | ..... | ND |

[a] Symbols explained in table 1.

[b] The iron backing of the glass-lined tank enamel was severely attacked at 0.1 to 25 percent $H_2SO_4$ and $CH_3COOH$, $H_2$ was evolved, which chipped and shattered the enamel, thus destroying the specimen.

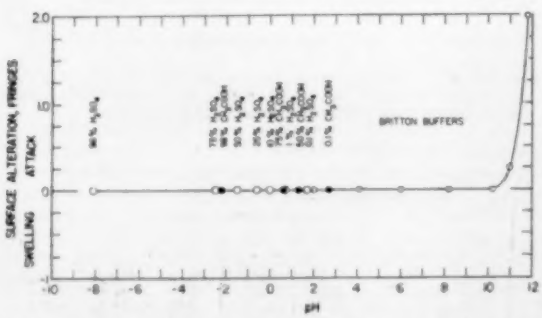


FIGURE 9. *Chemical durability of class A acid-resistant porcelain enamel over the range* pH − 8 *to* pH 12 *after exposure for 6 hours at 80° C.*

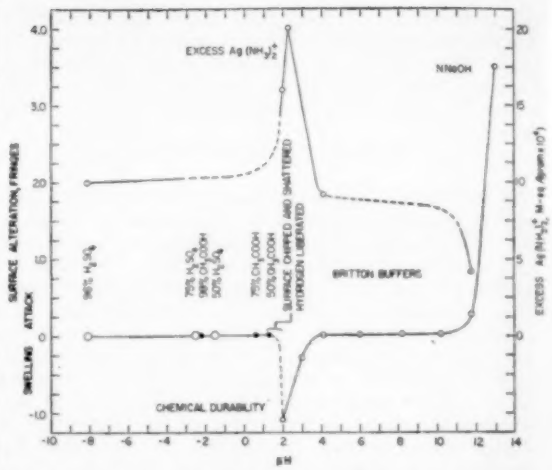


FIGURE 10. *Comparison of the uneven distribution of migratable ions at the enamel-solution interface with the chemical durability of a porcelain enamel used in glass-lined tanks, after exposures for 6 hours at 80° C.*

TABLE 8. *Uneven distribution of* $Ag(NH_3)_2^+$ *at the enamel-solution interface after leaching in various solutions for 6 hours at 80° C*

| Enamel | Treatment | | Excess $Ag(NH_3)_2^+$ |
|---|---|---|---|
| | *pH* | *Solution* | *M-eq/g* |
| Glass-lined tank | ..... | None | [a] $<0.2\times10^{-4}$ |
| | −8.1 | 96% $H_2SO_4$ | 10 |
| | 2.0 | Britton buffer | 16 |
| | 2.3 | $CH_3COOH$ | 20 |
| | 4.1 | Britton buffer | 9 |
| | 11.8 | .....do | 4 |
| Class D acid resistant | ..... | None | <0.2 |
| | 4.1 | Britton buffer | 415 |

[a] Symbols explained in table 1.

Because the composition of the enamels was not known in detail, it is difficult to discuss the mechanism or nature of the attack indicated by the interferometer data. The evidence, however, that porcelain enamel is subject to alkaline attack correlates well with field tests that have been made on enamelware [13]. It appears that the nature of the attack on the enamels is analagous to that on commercial glasses. It would seem, then, that some of the problems of the chemical durability of different enamels could be advantageously studied by these techniques.

### 3.4. Metals

Although the interferometer has been used widely in science and industry, the procedure for measuring the chemical durability has not been applied to the study of the corrosive resistance of metals and alloys to acids and bases of all concentrations. The chemical durability of cold-rolled steel, aluminum, copper,

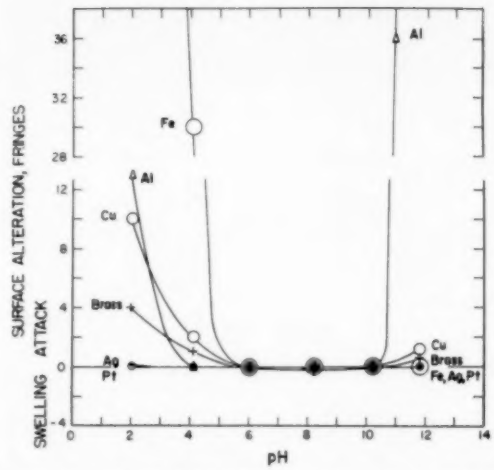


FIGURE 11. *Chemical durability of various metals and alloys after exposure to Britton buffers for 6 hours at 80° C.*

TABLE 9. *Chemical durability of metals exposed to Britton buffers for 6 hours at 80° C*

| Metal | Surface alteration at pH— | | | | | | |
|---|---|---|---|---|---|---|---|
| | 2.0 | 4.1 | 6.0 | 8.2 | 10.2 | 11.0 | 11.8 |
| | *Fringes* | *Fringes* | *Fringes* | *Fringes* | *Fringes* | *Fringes* | *Fringes* |
| Cold-rolled steel | • 360 A | 30 A | ND | ND | ND | ..... | ND |
| Aluminum | 13 A | ND | ND | ND | ND, SC, black | 36 A | 390 A |
| Copper | 10 A | 2 A | ND | ND | ND | ..... | 1+A |
| Brass | 4 A | 1 A | D S | ½a S | ND | ..... | ½ A |
| Silver | ½o+A | ND | ND | ND | ND | ..... | ND |
| Platinum | ND | ND | ND | ND | ND | ..... | ND |

Symbols explained in table 1.

brass, silver, and platinum is shown in figure 11 (data given in table 9). Because of the rapid reaction of some of the samples, exposures as short as 1 min were required, and the results were extrapolated to 6 hr in order to put all the data on a comparable basis. The swelling of brass and the slight attack on silver might be more convincingly demonstrated by increasing the exposure time to 24 hr or more. When aluminum was treated at pH 10.2, a hard black almost nonreflecting coating was formed, although no dimensional change could be detected by the interferometer. In fact, in many cases there was a color change in the treated area but with no detectable dimensional change. Hass [14] states that the oxide film on aluminum may be as thin as 20 A. Because the lower limit of resolution of the interferometer is about 30 A, no swelling could be observed. It is also interesting to note that the points at which surface alteration becomes detectable correspond very closely to the values determined by Wells [15], namely, pH 3.95 and pH 10.94, where aluminum hydroxide becomes soluble in the acid and alkaline regions. In several samples where a slight attack or dull matt swollen surface had resulted, repeated gentle polishing on 4/0 emery paper increased the observable attack in the exposed area to a definite maximum. This indicates that chemical attack had progressed to a considerable depth below the surface. In all cases the maximum attack noted after the emery-paper treatment was reported as the chemical durability.

The results on all metals tested show good corrosive resistance from pH 6 to pH 10. There is, however, a very definite attack on all the metal surfaces except platinum at pH values below this range. Because of the sensitivity of the interferometer measurements, the method offers a means of studying the corrosive resistance of metals and alloys under very diverse conditions.

## 4. References


[1] Donald Hubbard and Edgar H. Hamilton, Studies of the chemical durability of glass by an interferometer method, J. Research NBS **27**, 143 (1941) RP1409.

[2] Donald Hubbard, Mason H. Black, Sylvanus F. Holly, and Gerald F. Rynders, Electrode function (pH response) hygroscopicity and chemical durability of soda-potash-silica glasses, J. Research NBS **46**, 168 (1951) RP2189.

[3] Donald Hubbard and Richard G. Goldman, Heterogeneous equilibria at the glass electrode-solution interface, J. Research NBS **48**, 428 (1952) RP2333.

[4] H. T. S. Britton, Hydrogen ions, I, 3d ed., p. 313 (D. Van Nostrand Co., New York, N. Y., 1943).

[5] James W. McBain, The mechanism of the adsorption (sorption) of hydrogen on carbon, Phil. Mag. **18**, 916 (1909); Z. Physik. Chem. 68, 471 (1909).

[6] Donald Hubbard, Hygroscopicity of optical glasses as an indicator of serviceability, J. Research NBS **36**, 365 (1946) RP1706.

[7] Samuel Glasstone, Textbook of physical chemistry, 2d ed., pp 1259–1262 (D. Van Nostrand Co., Inc., New York, N. Y.)

[8] T. E. Stanton, Expansion of concrete through reaction between cement and aggregate, Proc., Am. Soc. Civil Engrs. **66**, 1781–1811 (1940).

[9] W. C. Hansen, Studies relating to mechanism by which alkali reaction produces expansion in concrete, J. Am. Concrete Inst. Proceedings, **40**, 213–227 (Jan. 1944)

[10] Willard H. Parsons and H. Insley, Aggregate reaction with cement alkalies, J. Am. Concrete Inst. **19**, 625–631 (1948).

[11] H. E. Vivian, Studies in cement aggregate reaction, Part XV Commonwealth Scientific and Industrial Research Organization, Australia, Bul. No. 256, p. 78 (1950).

[12] Test for acid resistance of porcelain enamels, Part 1 (Flatware, Porcelain Enamel Institute, 1346 Conn. Ave. NW, Wash. 6, D. C.)

[13] J. R. Crandall, J. C. Richmond, A. G. Eubanks, and W. N. Harrison Progress report on the correlation of service data with laboratory tests on porcelain enamels, given at ACS meeting Apr. 1952 Pittsburgh, Pa.

[14] G. Hass, Growth and structure of thin oxide layers on aluminum, Optik **1**, 134–43 (1946).

[15] Lansing Wells, Reaction of water on calcium aluminate, BS J. Research **1**, table 15 (1928) RP34.


WASHINGTON, October 10, 1952.

rnal of Research of the National Bureau of Standards Vol. 50, No. 2, February 1953 Research Paper 2395

# Transitions and Phases of Polytetrafluoroethylene (Teflon)[1]

Charles E. Weir

Transitions in polytetrafluoroethylene (Teflon) have been studied as a function of pressure and temperature. A high-pressure transition (5,000 atm) and a lower pressure transition were studied. These are believed to result from three polymorphic forms. The pressure of the high-pressure transition decreases and that of the low-pressure transition increases with increasing temperature. A triple point is indicated at approximately 70° C, and a third equilibrium line is found to proceed to higher pressures with increasing temperature from this point. Experimental errors involved render tests of all thermodynamic conditions at the triple point indeterminate.

## 1. Introduction

In the course of a continuing study of pressure-volume-temperature relationships in high-polymeric materials measurements have been made on polytetrafluoroethylene (Teflon). This report describes the pressure-temperature dependence of the transitions of Teflon. These transitions show a surprisingly complex behavior that is unique among all the polymers studied to date.

The room-temperature transition was discovered by Rigby and Bunn [1] [2] and independently by the author [2] at about the same time. The transition that occurs at about 20° C is a reversible first-order transition producing reversible changes in the X-ray diffraction pattern. The changes in the X-ray pattern have been interpreted as arising from specific changes in the crystal structure of the Teflon [1]. Quinn, Roberts, and Work [3] studied the transition extensively by volumetric methods and observed that the transition was complex, the complexity consisting of a double break in the volume-temperature curve associated with some degree of hysteresis. They evaluated the total volume change (that is, the sum of the two observed discontinuities) as 1.23 percent. Pierce, Bryant, and Whitney [4] have recently studied the X-ray pattern of Teflon over a wide temperature range.

Bridgman [5] and the author [6] have reported first-order transitions in Teflon under high pressures at room temperature. Bridgman reported the transition at 6,500 kg/cm$^2$ as involving a volume change of 2.26 percent, whereas the author found the transition centering about 5,500 atm at 25.5° C, with an associated volume change of 2.35 percent. Differences between these data may well be due to variations in samples.

Finally, Furukawa [7] has measured the specific-heat-temperature properties of Teflon. His data show the double discontinuity referred to, and he evaluated the total latent heat of the two breaks as approximately 8 j/g. It is immediately apparent that this latent heat is not sufficiently large to fit the assumption that the high-pressure and room-temperature transitions are related. The 2:1 ratio of volume changes now tends to confirm this conclusion.

As a result of the present studies it is concluded that Teflon undergoes two separate transitions, one at high and one at lower pressures at temperatures below 70° C. The phase diagram for these transitions indicates at least three forms for the crystalline regions of Teflon. The evidence points to the fact that these are most probably polymorphic forms.

## 2. Experimental Method

The apparatus and experimental procedure have been described in detail previously [8] and will not be discussed fully here. Briefly, an experiment consists in forcing a leakproof piston into the bore of a heavy-walled cylinder containing the specimen and the manganin pressure gage immersed in a suitable pressure transmitting medium, and taking pressure-volume readings. For locating a transition a graph of pressure versus piston position is constructed, the transition appearing as a discontinuity in this curve.

In these experiments the hydraulic press and pressure vessel were enclosed in a thermostatted air bath that could be maintained at elevated or reduced temperatures. Temperatures were measured with a calibrated mercury thermometer set in a well in a massive brass block fastened to and in intimate thermal contact with the pressure vessel. A maximum variation of $\pm 0.35$ deg C was noted on this thermometer at any temperature. However, the enormous heat capacity of the pressure vessel probably reduced the variation in temperature of the specimen to a considerably smaller value.

Inasmuch as the pressure gage was subjected to various temperatures in these experiments, it was calibrated at most temperatures used. Fixed points for calibration were taken from the International Critical Tables [9] but originate from data obtained by Bridgman. The transitions used for calibration were: Water-ice VI at lower temperatures; freezing of chloroform and $CCl_4$ I to II at intermediate temperatures; and urea I to III at higher temperatures. Small inconsistencies noted in these calibrations were not studied, the variations being of such small magnitude that any error resulting was negligible in these experiments. However, subjection of the gage to the elevated temperatures resulted in limiting the measurements to a maximum temperature of approximately 80° C. After continued exposure to this temperature, marked drifting of the resistance of the pressure gage was observed. This drift is probably due to the action of the confining

[1] This paper is a preliminary summary of work on a project sponsored by the Office of Naval Research.

[2] Figures in brackets refer to literature references at the end of this report.

239286—53——3

liquid on the shellac-treated gage coil. A study of the behavior of this or other materials to higher temperatures would require considerable modification of the apparatus to permit the pressure gage to remain at room temperature.

All data in these experiments were measured isothermally. Isobaric measurements were attempted, but the large heat capacity of the apparatus effectively excludes interpretation of this type of data, the actual temperature of the specimen being unknown.

A single specimen of Teflon was used in all measurements. It was obtained from E. I. du Pont de Nemours & Co., Inc., and had a density of 2.219 g/cm³ at 20° C. The initial volume of the specimen was approximately 21 cm³ at 20° C, initial volumes at other temperatures being calculated from the data of Quinn, Roberts, and Work [3], who studied a specimen cut from the same sample.

## 3. Results and Discussion

Typical compression curves of Teflon are shown in figure 1. These measurements were made at the temperatures indicated, but the curves are shown displaced along the vertical or compression axis to reduce overlapping. The numerical compression data for these curves will be given in a subsequent report because they are not of primary interest here.

It is seen in figure 1 that two transitions exist at intermediate temperatures, a high-pressure transition involving approximately a 2-percent change in volume and varying with temperature around 5,000 atm and a low-pressure transition involving a 1-percent volume change at somewhat lower pressure. This low-pressure transition occurs even at 38° C and at lower temperatures, but at pressures below 1,000 atm which is the lower limit for these data. At 81.0° C, however, no corresponding transition can be found.

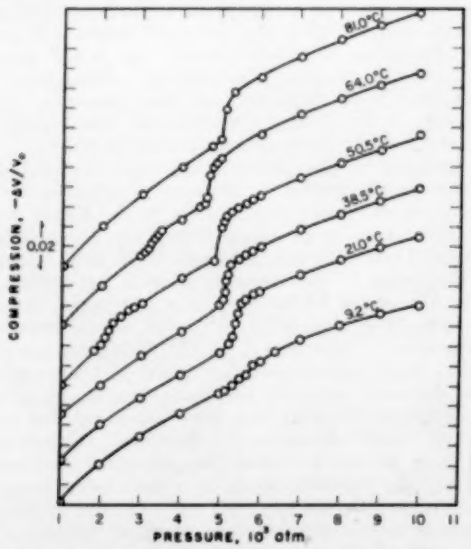


FIGURE 1. *Compression curves of Teflon at various temperatures.*

The following points of interest are to be noted in figure 1: The rounded corners at the transition pressure, combined with the existing curvature arising from pressure dependence of compressibility, render evaluation of $\Delta V$ for the transition rather uncertain. There is little doubt, however, that $\Delta V$ for the high-pressure transition increases, whereas $\Delta V$ for the low-pressure transition decreases with increasing temperature.

Both transitions occur over a small pressure interval rather than at a fixed pressure. Expected small differences in structure of crystalline regions in Teflon would cause this effect as well as the rounding of the corners at the transition.

The behavior at the high-pressure transition with increasing temperature is interesting. At low temperatures this transition is "smeared out" over a rather large pressure interval, as seen in figure 1. With increasing temperature it becomes noticeably sharper, and at temperatures above 60° C the transition may be observed easily, since the piston may be withdrawn 0.040 in., with no change in pressure at the transition point. This type of behavior has been referred to many times by Bridgman [10].

All data have been obtained on *decreasing* pressure, although there is no evidence of a region of indifference [10] in these transitions. On increasing pressure, however, with only the low-pressure phase present, considerable excess pressure must be applied to produce initiation of the transition.

TABLE 1. *Experimental transition data on Teflon*

| Transition | | | | | |
|---|---|---|---|---|---|
| I to II | | II to III | | I to III | |
| $P$ | $t$ | $P$ | $t$ | $P$ | $t$ |
| *atm* | *°C* | *atm* | *°C* | *atm* | *°C* |
| 520 | 29.7 | 5,550 | 8.0 | 4,840 | 75.0 |
| 580 | 31.0 | 5,650 | 9.2 | 5,050 | 81.0 |
| 1,060 | 38.5 | 5,540 | 16.9 | 4,940 | 81.0 |
| 2,130 | 50.5 | 5,350 | 21.0 | | |
| 2,470 | 57.0 | 5,200 | 32.6 | | |
| 3,200 | 64.0 | 5,090 | 38.6 | | |
| 4,000 | 68.5 | 4,910 | 50.5 | | |
| | | 4,740 | 57.0 | | |
| | | 4,560 | 63.0 | | |
| | | 4,630 | 64.0 | | |
| | | 4,590 | 68.2 | | |

The experimental data obtained on these transitions are shown in table 1 and figure 2. The several regions are denoted as corresponding to forms I, II, and III, and the $P,T$ data experimentally obtained on the transitions are those given in table 1.

The equilibrium line II to III is well defined and linear. The least squares equation of this line is found to be

$$P=-17.5t+5761 \qquad (1)$$

for pressures in atmospheres and temperatures in degrees C. The negative slope requires in a transi-

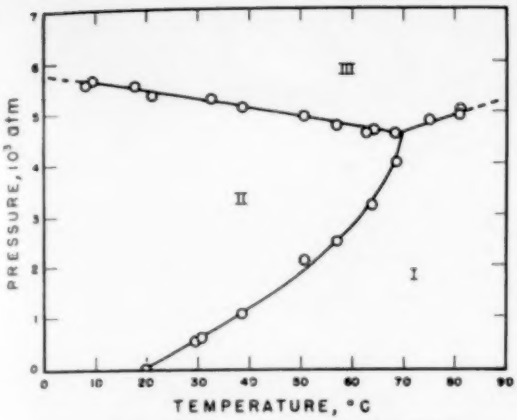


FIGURE 2. *Proposed phase diagram for Teflon.*

tion from II to III, in which the volume decreases, that heat be absorbed. This type of transition, although rare under 1-atm pressure, has been observed many times under elevated pressures [10]. With increasing temperature $\Delta V$ increases rather slowly along the II to III line, and from figure 1 it is obvious that III is considerably less compressible than II. This difference in compressibilities has not been evaluated quantitatively. The I to II equilibrium line is less well established but is certainly nonlinear. Here $\Delta V$ is much smaller and decreases rapidly with increasing temperature. Due to the decrease in $\Delta V$ with temperature, the point shown at 68.5° C is subject to some uncertainty. At low pressures (that is, below 1,000 atm) the experimental points are also subject to some uncertainty, arising from the fact that the apparatus behaves indifferently well at pressures below 700 atm. That the course of the curve is essentially correct at low pressures, however, is shown by the agreement between the latent heat of 1.54 cal/g calculated from the graphical slope at zero pressure and the observed value of 1.91 cal/g measured by Furukawa [7]. The latter value contains the total latent heat of the double transition, as mentioned previously.

No evidence was found for any transition line originating at the second discontinuity noted by Quinn, Roberts, and Work [3] at 30° C. The low pressures required and the small magnitude of the volume change involved would effectively obscure any such observations with the present apparatus. Inasmuch as X-ray studies have apparently disclosed no phenomena at 30° C [1, 4], the behavior of Teflon in the vicinity of 30° C requires further study.

In figure 2 a triple point is shown at approximately 70° C. That such a point exists is strongly indicated by the abrupt change in slope experienced by the II to III transition line in this region. For this reason, it is believed that a true triple point exists and that the phases I, II, and III are truly polymorphic. The alternative choice that the transitions occur in incoherent phases seems rather unlikely. It appears from the measured data that the requirement that $\Delta H=0$ for a closed path enclosing the triple point does not appear to be fulfilled. However, because the $\Delta V$ values cannot be accurately determined and $\Delta V$ for the I to II transition becomes extremely small near this point, the apparent discrepancy may not be real.

The diagram shown in figure 2 cannot represent more than a portion of the behavior of Teflon because X-ray studies have shown melting of crystals at approximately 330° C [1]. At least one additional transition line must therefore appear at higher temperatures [11]. In this connection, it is to be noted that the extrapolation of the II to III transition line cuts the temperature axis at 329° C. Inasmuch as the details of this diagram cannot be further clarified with the present apparatus, it is presented with full recognition of its lack of completeness and the fact that the proposed phases should be verified by X-ray studies.

## 4. References

[1] H. A. Rigby and C. W. Bunn, Nature **164,** 583 (1949).
[2] C. E. Weir, unpublished data.
[3] F. A. Quinn, D. E. Roberts, and R. N. Work, J. Applied Phys. **22,** 1085 (1951).
[4] R. H. H. Pierce, Jr., W. M. D. Bryant, and J. F. Whitney, report to the Division of Polymer Chemistry, American Chemical Society, Buffalo, N. Y., March 1952.
[5] P. W. Bridgman, Proc. Am. Acad. Arts Sci. **76,** 55 (1948).
[6] C. E. Weir, J. Research NBS **46,** 207 (1951) RP2192.
[7] George T. Furukawa, Robert E. McCoskey, Gerard J King, Calorimetric properties of polytetrafluoroethylene (Teflon) from 0° to 365° K, J. Research NBS **49,** 273 (1952) RP2364.
[8] C. E. Weir, J. Research NBS **45,** 468 (1950) RP2160.
[9] International Critical Tables, vol. IV (McGraw-Hill Book Co., Inc., New York, N. Y., 1928).
[10] P. W. Bridgman, The physics of high pressure (G. Bell & Sons Ltd., London, 1949).
[11] P. L. McGeer and H. C. Duus, J. Chem. Physics **20,** 1813 (1952).

WASHINGTON, November 26, 1952.

Journal of Research of the National Bureau of Standards Vol. 50, No. 2, February 1953 Research Paper 2396

# Hydrodynamic Effects of Gales on Lake Erie

Garbis H. Keulegan

The coefficients of wind stress and the sea roughness are derived from records of water levels and wind intensities relating to gales passing over Lake Erie during the past fifty years. The reduction of wind velocities measured at various elevations in four cities on the lake shore to a single "effective wind velocity" over the lake is explained. A theoretical determination of the wind tides agrees well with the observations. The coefficient of wind stress derived from the observations is nearly the same as that obtained by Neumann from observations in the Gulf of Bothnia. Both the coefficient of wind stress and the sea roughness are found to decrease with increasing wind velocities.

## 1. Introduction

For a wind blowing steadily with a uniform intensity over a lake, the relationship between the wind intensity and the frictional stress induced at the water surface may be found by considering the wind tides produced at the ends of the lake. Wind tides are those displacements of the water level from the initial undisturbed level that are due solely to the action of the wind. The relationship involves a characteristic quantity called the coefficient of wind stress. There will be an element of uncertainty in the coefficient derived if the wind stress corresponding to a wind of constant intensity is a function of distance, or fetch, and only the wind tides at the lake ends are known. In such cases the analysis yields average values of the wind stresses, and if it be true that the stress is also a function of fetch, the derived coefficient of wind stress will be different for lakes of different lengths.

Another source of uncertainty in the values of the coefficient of wind stress is in the derivation of the formula which relates the wind stress to the wind tides. In working out the formula, due attention must be given to the nonuniformity of depth of water in the lake and of width of the lake surface, and also to the magnitude of the friction at the bottom of the lake. The turbulence pattern in the waters of a lake under the action of wind is at the present time far from being depicted. The partition of velocities in the drift current at the upper layers and in the returning gravity current in the lower layers, and the magnitudes of the mixing lengths, are questions which have not been studied. Lack of information of this nature prevents one from appraising accurately the the frictional force at the lake bottom. Besides, if the boundary of a lake exhibits very marked irregularities and there are also numerous islands distributed in the regions close to the lake ends, the derivation of the exact wind tide formula is very difficult and in some cases may be impossible. These difficulties are present to some extent in the case of Lake Erie.

A second problem in connection with the action of wind on lakes is the relationship between the effective roughness of the sea and the velocity of the wind. Meteorologists regard the Prandtl law of velocities as representing satisfactorily the state of movement of the wind in the layers of air above the water surface. This law requires a roughness length which is called the roughness of the sea. Once the coefficient of wind stress based on the wind velocities at points of known distance from the surface of the water is known for a given lake, the sea roughness is readily obtained from the value of the coefficient. Since sea roughness is an inferred quantity and is a function of stress, the likelihood exists that the sea roughness is a function of fetch. If the determination of roughness is made on the basis of average stresses at the lake surface, the value of roughness may vary for a given wind velocity for lakes of different lengths.

It is proposed in the present work to obtain the values of the coefficient of wind stress and of the sea roughness for Lake Erie. The determinations are brought about by considering the maximum wind tides observed during the severe westerly gales passing over Lake Erie in the past half century.

## 2. Sources of Original Data

The hydrographic charts of the United States Lake Survey showing the surface changes of Lake Erie during gales constitute the chief source of material for the present investigation. These charts show the water stages at the extremities of the lake, and the values of the hourly movement of wind and its direction for a few stations on the southern coast. Two examples of such charts are given by Freeman [1].

The stations for which charts of water stages are given have been changed from time to time. Buffalo and Amherstburg, or Gibraltar, are the localities near the ends of the lake for which the water stages are given for westerlies during the earlier years. For easterlies the corresponding localities are Toledo and Buffalo. In these charts complete wind data are shown for Toledo, Cleveland, Erie, and Buffalo. In the charts of later years, water stages are shown for Toledo and Buffalo. However, the representation of wind data has not always been complete, and in such instances the missing information has been received from the U. S. Weather Bureau.

It was desired to handle the analysis on the basis of the wind tides observed at Toledo and Buffalo. The data for Toledo, where missing, were deduced from the data for Gibraltar and Amherstburg. This is feasible as in general a correlation exists for the wind tides of nearby localities. The desired correla-

tion factor could be determined, for in some of the charts the simultaneous values of the water stages at Toledo and Amherstburg are given. In this determination use was made also of Blunt's work [2].

In the determinations of the coefficients of wind stress, the observed wind tides must be corrected for barometric pressure changes. Data needed are the hourly values of the barometric pressures at Toledo and Buffalo for the periods of the gales considered. For these the U. S. Weather Bureau has kindly allowed us access to the proper records.

## 3. Determination of Effective Winds

### 3.1. City Wind Velocities at a Common Elevation

The evaluation of the coefficient of wind stress will be made with respect to wind velocities at a height of 25 ft above the water surface of the lake. As these velocities were not observed and the only available velocities are those measured over the cities of Toledo, Cleveland, Erie, and Buffalo, the lake wind velocities will be deduced from the city velocities. The reduction to the desired values will be made in three steps.

As the anemometer heights during a given period have been different in the cities mentioned, or have been changed in a given city from time to time, the first step of the analysis is to reduce all the measured wind velocities to the values appropriate to a common elevation. The elevation selected was 165 ft above the ground.

The region of air above the ground may be conceived to consist of two layers, the boundary layer below and the layer of frictional influence above. The boundary layer is relatively thin, and the movement of air in it is controlled entirely by frictional stress as horizontal pressure gradient and deflecting forces may be neglected. In a vertical traverse the frictional stress is constant, and the direction of the stress vector coincides with the direction of the wind. For this layer, Prandtl [3] gives the law of velocities

$$\frac{u}{u_*}=5.75 \log \frac{z}{\epsilon}, \tag{1}$$

where $z$ is the elevation of a point at which the velocity is $u$, $u_*$ is the shear velocity, and $\epsilon$ is the effective roughness. Denoting the frictional stress at the ground by $\tau_0$ and the density of air by $\rho_a$,

$$u_*=\sqrt{\tau_0/\rho_a}. \tag{2}$$

When the actual roughness is large, the reference level from which to measure the height $z$ is a matter of importance. It may be that in cities with an average height of buildings of $2K$ the reference level can be taken at the distance $K$ from the ground. Then, following Prandtl, the effective roughness $\epsilon_2$ of a city may be taken as

$$\epsilon_2=2K/30. \tag{3}$$

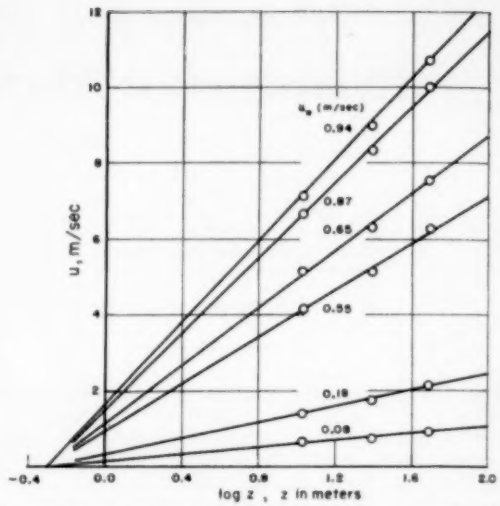


FIGURE 1. *Relation of wind velocity, u, to height over the city of Tokyo, z, from measurements by Siotani and Yamamoto.*

We may now consider, to test the utility of the rules given above, a known case of measured velocities over a large city. In the autumn of 1946 Siotani and Yamamoto [4] obtained the air velocities over the central part of Tokyo at elevations of 60, 55, 45, 35, and 25 m above the ground, using hot-wire anemometers on the tower at the Central Meteorological Observatory. The neighboring buildings being 10 to 20 m in height, $K$ in this case was 7.5 m.

In figure 1 are reproduced some of the velocity values from the original curves of these authors. In the plot $z$ is the height in meters measured from the reference level of 7.5 m above the ground. The straight lines drawn through the points meet at a common point on the abscissa axis, $\log \epsilon_2=-0.3$. Thus the effective city roughness is $\epsilon_2=0.5$ m, a result satisfying the rule implied by eq 3. Denoting by $u_0$, the value of the velocities to be read from the straight lines of the figure for $z=1$, the shear velocity may be computed as $u_*=-(u_0)/(5.75 \log \epsilon_2)$. The shear velocities thus computed are also entered in figure 1. Representing the data in figure 1 in dimensionless form, the results are the three points in figure 2. The distribution of the points confirms the relation given by eq 1, and this fact points to the possibility of applying the rule to cities in general.

Estimating the average height of buildings in American cities as 30 ft, the effective roughness may be taken to be 1 ft. Measuring the elevation of points $z$ from a reference level 15 ft above the ground, denoting the position of an anemometer by $z_a$, the measured velocity by $u_a$, the standard height by $z_2$ (=150 ft), the velocity at this height by $u_{22}$, the roughness of the city by $\epsilon_2$ (=1 ft), the formula to reduce the anemometer velocities to the

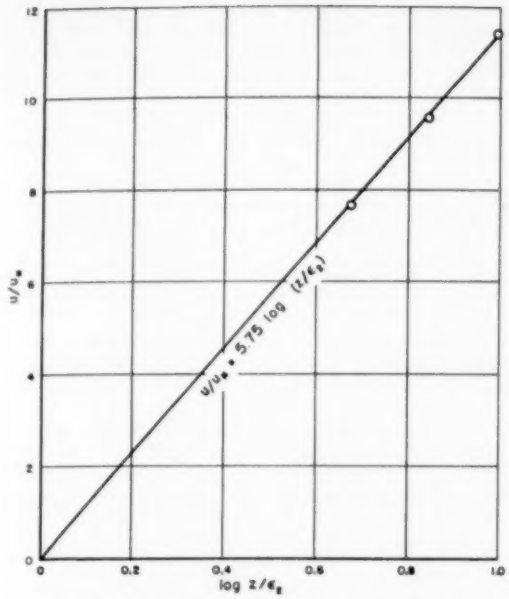


FIGURE 2. *Relation of wind velocities measured over the city of Tokyo to the Prandtl law.*

velocities at standard heights is

$$\frac{u_{22}}{u_a}=\log\frac{z_2}{\epsilon_2}\Big/\log\frac{z_a}{\epsilon_2}. \tag{4}$$

The curve in figure 3 is established through this relation and is used to reduce the anemometer velocities to the velocities corresponding to the standard height $z_2$ (=150 ft). For the purpose of comparison a second curve is shown, evaluated with $\epsilon_2$=2 ft. The disparity between the curves being small, it is seen that errors arising from the uncertainties in the exact value of the city roughness are not very appreciable.

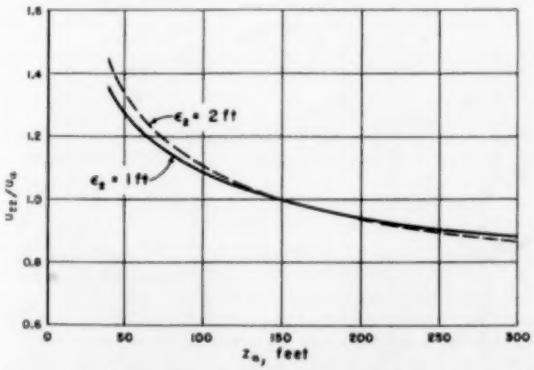


FIGURE 3. *Ratio of wind velocity at a standard height of 150 feet above a city, $u_{22}$, to the wind velocity indicated by an anemometer, $u_a$, as a function of the height of the anemometer, $z_a$, and the roughness of the city, $\epsilon_2$.*

### 3.2. Wind Velocities Over the Lake Surface

The second step is to infer the wind velocities over the lake surface from the wind velocities $u_{22}$ corresponding to the standard height $z_2$ (=150 ft) over the city. To establish the desired values resort is to be made to the characteristic relationships involving the various quantities of the layer of frictional influence. Regarding the hydrodynamics of the layer, the analysis of Rossby [5] proves to be particularly fruitful.

The quantities that will be of value here are the height, $H$, of the boundary layer, the wind velocity, $U_H$, at the upper surface of the boundary layer, the gradient wind, $U_g$, and the angle $\phi_s$ between the direction of the gradient wind and the direction of the wind in the boundary layer. The Rossby relations are

$$U_H=U_g\left(\cos\phi_s-\frac{1}{\sqrt{2}}\sin\phi_s\right), \tag{5}$$

$$H=0.54\,k^2\frac{U_g}{f}\sin\phi_s,\ k=0.065, \tag{6}$$

and

$$\log U_g/f\epsilon=1.694\cot\phi_s-\log\sin\phi_s+1.441. \tag{7}$$

Here $f$ represents the quantity $f=2\Omega\sin\lambda$, $\Omega$ being the angular speed of the earth's rotation, and $\lambda$, the latitude. The roughness of the surface below is $\epsilon$. The importance of the effective roughness, of the ground or of the sea, for the quantities pertaining to the lower layers of the atmosphere can easily be seen.

Once it is assumed that the magnitude and the direction of the gradient wind are the same over the lake water and over the constal regions next to the lake, eq 5, 6, and 7 provide the means by which a relationship may be established connecting the velocity of the wind over the surface of the lake with the velocity of the wind over a city on the borders of the lake.

For a second definition of terms the diagram in figure 4 may be consulted. Assuming a gradient

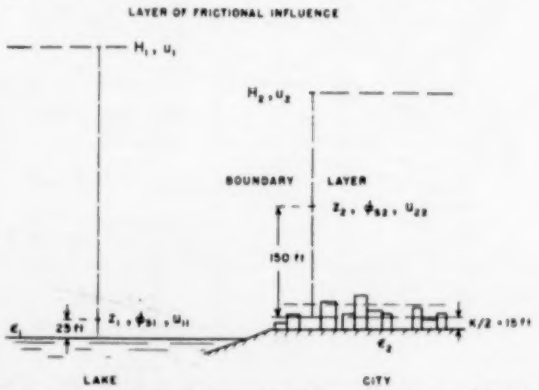


FIGURE 4. *Notation diagram for winds over a lake and a city on its shore.*

wind constant both in intensity and in direction blowing in the higher regions over the lake and over the city, let $H_1$ denote the height of the boundary layer over the lake and $H_2$ that over the city. Let $\epsilon_1$ denote the effective sea roughness and $\epsilon_2$ the roughness of the city. Let $u_1$ denote the wind velocity at the upper surface of the boundary layer over the lake and $u_2$ that over the city. Let $u_{22}$ denote the wind velocity over the city at the standard height $z_2$ (=150 ft) and $u_{11}$ that over the lake at the standard height $z_1$ (=25 ft). Let $\phi_{s2}$ be the angle between the direction of the wind over the city, and the direction of the gradient wind, and $\phi_{s1}$ the corresponding angle over the lake. Then, according to the Prandtl law of velocities given by eq 1, the formula which reduces the wind velocities over the city to those over the lake is

$$\frac{u_{11}}{u_{22}}=\frac{u_1}{u_2}\left[\frac{\log\dfrac{z_1}{\epsilon_1}}{\log\dfrac{H_1}{\epsilon_1}}\Big/\frac{\log\dfrac{z_2}{\epsilon_2}}{\log\dfrac{H_2}{\epsilon_2}}\right], \tag{8}$$

the computations being made through eq 5, 6, and 7. The results are shown in the form of curves in figure 5, with the ratio $u_{11}/u_{22}$ plotted as function of $u_{22}$ for various sea roughnesses. It is seen that the ratio $u_{11}/u_{22}$ for a given wind velocity depends to an appreciable degree on the sea roughness. In using the graphs for the desired reductions of wind velocities for a given storm, it was necessary to assume a value for the sea roughness. The value selected was $\epsilon_1=0.3$ cm. Evaluations from the data of wind tides given later in this paper confirm this chosen value as an average.

It will be remembered that the curves of figure 5 are based on a city roughness of value $\epsilon_2=1$ ft (30.5 cm). Accordingly, the figures show that if the sea roughness be $\epsilon_1=0.3$ cm, the wind velocity observed at the lake surface at a height 25 ft above the water will be about 1.12 times the city wind velocity observed at a point 165 (=150+15) ft above the ground for the higher velocities of the city wind. It will be found, considering the data of figure 3 also, that if the city wind velocity be observed at a height 315 ft above the ground, it gives the wind velocity over the lake. This is in agreement with the findings of Kadel [6] in an investigation of wind observations at Buffalo.

The roughness of the sea being much smaller than the roughness of a city, there is a change in the wind direction in passing from a city over a lake surface. The change is $(\phi_{s2}-\phi_{s1})$, and the estimated values as deduced from the Rossby relations are shown in figure 6. The magnitude of change depends on the wind velocity and the sea roughness. If the sea roughness be chosen as $\epsilon_1=0.3$ cm, the value of the average change is about $(\phi_{s2}-\phi_{s1})=7°$ for the higher wind velocities.

### 3.3. Effective Lake Wind Velocity

The third step is to determine the effective lake wind velocity, which is the velocity of the wind necessary to produce the observed wind tide under the condition that the wind blows with uniform intensity along the axis of the lake. When the actual winds at Toledo, Cleveland, Erie, and Buffalo during a storm are examined, it will be seen that these winds differ from each other in intensity and also in direction. The need for a formula to give the effective wind is readily seen.

The outlines of Lake Erie are shown in figure 7. The direction of a wind blowing from the south is

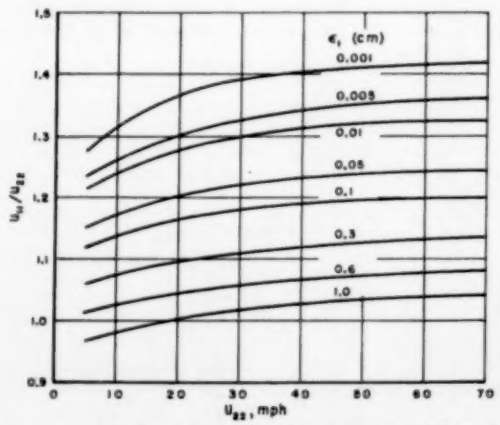


FIGURE 5. *Relation between winds at a standard height of 25 feet over a lake, $u_{11}$, to winds at a standard height of 150 feet over a city, $u_{22}$, for various sea roughnesses.*

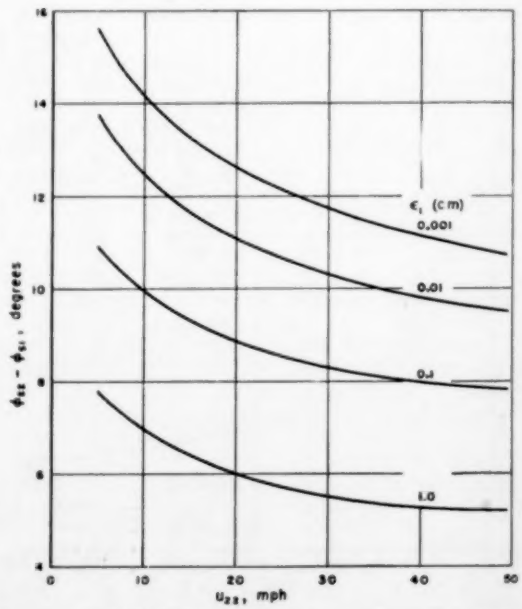


FIGURE 6. *Difference in direction of winds over city and lake as function of wind velocity over the city for various values of the sea roughness.*

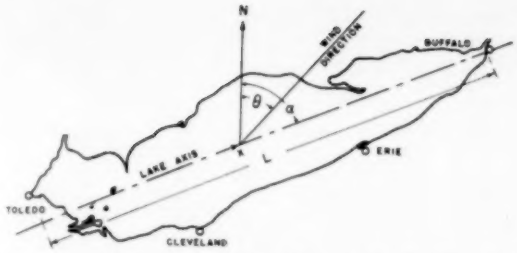


FIGURE 7. *Sketch map of Lake Erie showing locations of cities considered and notation for directions.*

chosen as the reference direction from which to measure wind directions. The lake axis is drawn so that it divides the area of the lake into two equal parts. Its direction is approximately $\alpha=68°$. In the cross section through the point $x$ on the lake axis the velocity of the wind at an elevation of 25 ft above the water surface is $u_{11}$, and its direction is $\theta$, an angle less than 180°. Denoting the effective lake wind by $V$ and the length of the lake axis by $L$,

$$V^2=\frac{1}{L}\int_0^L u_{11}^2 \cos(\theta-\alpha)dx. \tag{9}$$

This formula is applicable when $(\theta-\alpha)$ is small and the resulting wind velocity is large, for then the effect of the earth's rotation may be neglected and it may be imagined that the resultant movement of the water is in the direction of the lake axis. Putting $M=u_{11}/u_{22}$, where $u_{11}/u_{22}$ is determined by eq 8, eq 9 becomes

$$V^2=\frac{1}{L}\int_0^L M^2u_{22}^2 \cos(\theta-\alpha)dx. \tag{10}$$

In this transformation no provision is made for the circumstance that the wind directions are not the same over the lake and over a city on the shore of the lake. Theoretically, in the above, denoting the difference $(\theta-\alpha)$ as $\beta$, the factor $\cos\beta$ must be replaced by $\cos(\beta+\gamma)$ where $\gamma$ is the difference $(\phi_{12}-\phi_{11})$. Now $\cos(\beta+\gamma)=\cos\beta\cos\gamma-\sin\beta\sin\gamma$, where $\gamma$ is a small quantity not exceeding 7°. Also the larger and significant values of wind tide are associated with winds for which the absolute values of $\beta$ are less than $\pi/4$. Therefore it is readily seen that the resulting error is small when $\gamma$ is neglected.

When the exact variation of $u_{11}=Mu_{22}$ as a function of $x$ is not known, the formulation must be based on discrete values of wind velocities. Let $V_T$, $V_C$, $V_E$, and $V_B$ be the wind velocities $u_{22}$ at Toledo, Cleveland, Erie, and Buffalo. The corresponding values of $M$ and $\theta$ are denoted by the same subscripts. Let the lake axis be divided into three segments of equal length. It may be supposed that the winds prevailing over the end segments are deducible from $V_T$ and $V_B$. The middle segment may be divided into two equal parts in which the winds are deducible

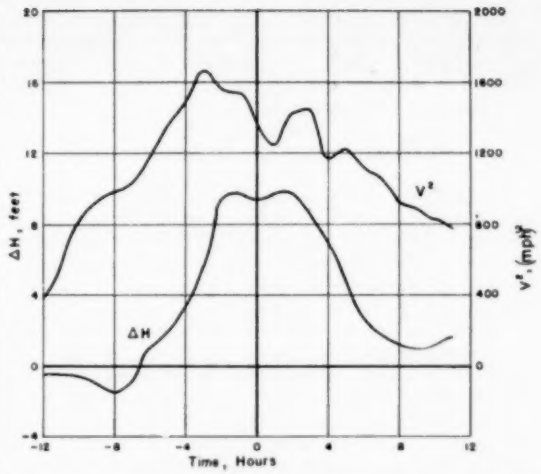


FIGURE 8. *The reduced data for wind tides, $\Delta H$, and effective winds, $V$, for storm of December 31, 1911.*

from $V_C$ and $V_E$. Thus instead of eq 10, we may write

$$V^2=\tfrac{1}{3}[M_T^2V_T^2\cos(\theta_T-\alpha)+M_B^2V_B^2\cos(\theta_B-\alpha)+\tfrac{1}{2}M_C^2V_C^2\cos(\theta_C-\alpha)+\tfrac{1}{2}M_E^2V_E^2\cos(\theta_E-\alpha)].$$

Now for the higher wind velocities, in which we are interested, the variation of $M$ is not large as may be seen from the curves in figure 5. Therefore without significant loss of accuracy, we may write

$$V^2=M^2V_2^2,$$
$$V_2^2=\tfrac{1}{3}[V_T^2\cos(\theta_T-\alpha)+V_B^2\cos(\theta_B-\alpha)+\tfrac{1}{2}V_C^2\cos(\theta_C-\alpha)+\tfrac{1}{2}V_E^2\cos(\theta_E-\alpha)]. \tag{11}$$

In this representation $V_2$ is, in a sense, the effective city wind velocity for the southern coast of the lake over the entire length between the lake extremities. Values of $M$ as a function of $V_2$ are shown in table 1. The table is established on the basis of the curve in figure 5 associated with $\epsilon_1=0.3$ cm, after identifying $u_{22}$ as $V_2$ and $u_{11}$ as $V$.

TABLE 1. *Dependence of the multiplying factor $M$ on the effective city wind velocity $V_2$*

| $V_2^2$ | $M^2$ | $V_2^2$ | $M^2$ |
|---|---|---|---|
| $(mph)^2$ | | $(mph)^2$ | |
| 100 | 1.150 | 1,300 | 1.254 |
| 200 | 1.175 | 1,400 | 1.257 |
| 300 | 1.193 | 1,500 | 1.260 |
| 400 | 1.205 | 1,600 | 1.262 |
| 500 | 1.214 | 1,700 | 1.264 |
| 600 | 1.223 | 1,800 | 1.266 |
| 700 | 1.229 | 1,900 | 1.268 |
| 800 | 1.234 | 2,000 | 1.270 |
| 900 | 1.239 | 2,100 | 1.272 |
| 1,000 | 1.243 | 2,200 | 1.273 |
| 1,100 | 1.247 | 2,300 | 1.274 |
| 1,200 | 1.251 | 2,400 | 1.275 |

The method of velocity reduction explained above was applied to all the wind data of the storms under consideration. The final values of effective wind for the storm of December 31, 1911, are shown in figure 8 as a matter of illustration.

## 4. Determination of Wind Tides

If the nodal point of the displacements of the surface water in Lake Erie during a storm be known and also the level of the undisturbed water prior to the storm, the coefficient of wind stress may be obtained by considering the wind tide at either end of the lake. Practically, however, this method of evaluation has to be avoided as it is difficult to determine the nodal point and the level of the lake with exactness. It is more satisfactory to base the determination of the coefficient on the relative displacement of the water at the lake ends. This relative displacement is called the total wind tide, and is denoted by $\Delta H$. The displacements are observed at Toledo and at Buffalo. In the case of a westerly gale if $h_B$ is the wind tide at Buffalo and $h_T$ is the wind tide at Toledo, the total wind tide is $\Delta H = h_B - h_T$.

This method of total wind tides has another advantage in the case of Lake Erie which may be mentioned very briefly. The particular phases of the storm effects that are specifically useful in determining the coefficient of wind stress are the maxima of the wind tides. Now, because the lake ends differ in shape, the rates of rise and fall of the water levels are different for the two ends. For Buffalo, the top part of the curve of tides is generally pointed; for Toledo, flat. Moreover, the maxima at Buffalo tend to occur earlier than at Toledo. These differences become more pronounced when the maturing storm increases rapidly in intensity. By adopting the total wind tide as the datum to be treated, the effects of these peculiarities of the individual behaviors are somewhat reduced and thus the data become more reliable.

In some of the charts of the westerly gales received from the Lake Survey the displacements of water for the western end of the lake are shown for Gibraltar or Amherstburg. In these cases the wind tide indications shown had to be reduced to the Toledo values. For the reductions it was necessary first to establish the correlation between the displacements at these western localities. This was possible, since in some of the charts the simultaneous values of the displacements are shown. Also Blunt [2] gives values of the maximum displacements for these localities. Introducing all these in figure 9 and drawing a straight line through the plotted points, it is seen that on the average

$$h_T = 1.71 h_A \qquad (12)$$

where $h_A$ is the displacement of water either at Gibraltar or Amherstburg. This is the correlation to be applied.

A final matter to be considered relative to the observed values of the wind tides is the correction for the effect of barometric pressures. Ordinarily, when the gale is moving over the lake area the pressures at the two ends of the lake are unequal. When the gale is a westerly, the greater pressure is at Buffalo. The difference of the atmospheric pressure at Toledo and Buffalo every hour of the storm period may be expressed as a head of water to be subtracted from the observed total wind tide.

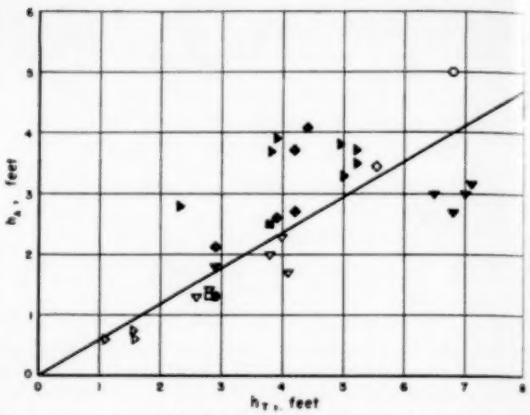


FIGURE 9. *Correlation of wind tides at Toledo, $h_T$, with those at Amherstburg and Gibraltar, $h_A$.*

○, Oct. 14, 1893. ●, Nov. 22, 1893. □, Nov. 28, 1893. ■, Oct. 28, 1895. ◇, Feb. 11, 1896. ◆, Jan. 20, 1907. ▽, Sept. 25, 1941. ▼, Jan. 2, 1942. ▷, Jan. 3, 1942. ▶, Mar. 25, 1947.
Data for years 1893, 1895, 1896 from Blunt.

## 5. Data for Winds and Wind Tides of Lake Erie Storms

The curves of wind intensity and total wind tide for the storm of December 31, 1911, shown in figure 8, are typical of all the storms considered in the present study. Taking the presentation in figure 8 as an example, it may be seen that the entire manifestation of the storm may be broken into three epochs; the epoch of maturing storm, the epoch of relative steadiness, and the epoch of recession. The hydrodynamical behavior of the water in the lake is expected to show marked differences during these epochs. In the initial epoch the wind must blow for some length of time before the response of the water to the action of the wind is completed. The reason for this condition is that any manifestation of wind tide must be associated with the flow of water from one end of the lake to the other. The action of the wind must establish a layer of drift current, the thickness of which must increase with time either under action of molecular viscosity, or turbulent viscosity, or both. As the water is being collected at the leeward end of the lake, a returning gravity current is created which likewise increases in intensity with time. The second epoch represents that steady condition in which the transport of water through the body of the drift current is counterbalanced by the transport of water in the returning gravity current that is maintained by the unchanging surface gradient of the lake waters. The third epoch is associated with decreasing wind intensity. With the

strength of the wind decreasing, the stress of the wind cannot maintain the adverse gradient of the surface water with the result that a surge of water in wave motion with a period equal to the seiche period of the lake is produced. In some records these seiches with periods of 4 hr are clearly seen during the time of the falling storm. The inertia effects are very pronounced in the extreme epochs: in the intermediate epoch they are considerably reduced.

For the determination of the relation between wind velocity and wind stress, only the manifestation of water level changes in the intermediate epoch will be considered. Referring once again to figure 8, the reference time is the instant of maximum wind tide. In each case of the storms considered the reference time is evaluated by taking the average of the times of maximum deflection of water at the two ends of the lake. As the total wind tide of the intermediate epoch we have taken the average value of the wind tide over a duration of 4 hr around the reference time. For the corresponding wind values we have taken the average value over a duration of 5 hr immediately preceding the reference time.

The wind velocities and wind tides thus obtained from each record are entered in table 2 with the dates of the storms indicated. In some of the wind tide charts the storms showed two peaks with an extended flat region between them. The total tides of such regions are also included in the data of table 2, and are identified with asterisks.

TABLE 2. *Wind tides of Lake Erie during westerly gales*

| No. | Date | $V$ | $V^2$ | $\Delta H$ |
|---|---|---|---|---|
| | | *mph* | $(mph)^2$ | *ft* |
| 1 | Nov. 21, 1900 | 50.5 | 2549 | 13.12 |
| 2 | Oct. 20, 1905 | 31.4 | 983 | 6.68 |
| 3 | Oct. 20, 1906 | 38.3 | 1471 | 9.75 |
| 4 | Jan. 20, 1907 | 48.1 | 2312 | 12.04 |
| 5 | Dec. 7, 1909 | 40.1 | 1608 | 10.51 |
| 6 | Dec. 31, 1911 | 38.9 | 1516 | 9.53 |
| 7 | Jan. 31, 1914 | 34.7 | 1207 | 7.95 |
| 8 | Dec. 9, 1917 | 43.2 | 1865 | 10.17 |
| 9* | Dec. 9, 1917 | 33.1 | 1093 | 4.56 |
| 10 | Dec. 10, 1907 | 34.3 | 1176 | 7.62 |
| 11 | Dec. 18, 1921 | 45.1 | 2033 | 12.30 |
| 12 | Dec. 8, 1927 | 47.4 | 2243 | 13.24 |
| 13 | Dec. 9, 1927 | 27.2 | 742 | 4.13 |
| 14* | Dec. 9, 1927 | 26.1 | 684 | 3.44 |
| 15* | Dec. 9, 1927 | 22.1 | 487 | 1.73 |
| 16 | April 1, 1929 | 51.3 | 2634 | 13.31 |
| 17 | Jan. 24, 1939 | 38.8 | 1508 | 9.40 |
| 18 | Sept. 25, 1941 | 35.7 | 1277 | 9.06 |
| 19 | Jan. 2, 1942 | 40.4 | 1632 | 12.53 |
| 20 | Jan. 3, 1942 | 19.5 | 379 | 2.38 |
| 21 | Nov. 22, 1946 | 34.2 | 1171 | 8.36 |
| 22 | Mar. 15, 1947 | 35.7 | 1276 | 8.34 |

The square of the wind velocities, $V^2$, near the lake surface and the corresponding wind tides, $\Delta H$, taken from table 2 are plotted in figure 10. Comparing the position of the plotted points with respect to the full line drawn, it is seen that the data corresponding to high wind velocities show small deviations from the curve, whereas those corresponding to low wind velocities show proportionately larger deviations, and all towards lower values of $\Delta H$. One inference is that the wind stress for low

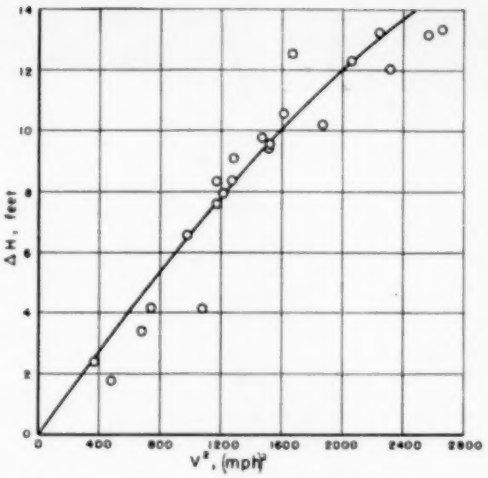


FIGURE 10. *Wind tides in Lake Erie.*
Data for plotted points taken from table 2.

wind velocity is relatively smaller. Unfortunately, the observations for the lower wind velocities are not sufficiently numerous to establish this point beyond doubt.

## 6. Integration of the Wind Tide Equation for Lake Erie

First the wind tide differential equation for a lake of arbitrary shape will be derived. Let positive $x$ be drawn along the direction of the wind, this direction coinciding with the axis of the lake. At the point $x$ the wind tide is $h$, it being the elevation of the raised water surface with respect to the level of the undisturbed water. See figure 11. Corresponding to $h$ at $x$ the surface width of the water is $B$, the cross-sectional area is $A$, and the mean depth is $\overline{H}$. The cross section is normal to the axis of the lake. The velocity of the wind is $V$, and the corresponding wind stress is $\tau_s$. At the bottom the stress induced by the gravity current is $\tau_0$. The density of water is $\rho$ and that of air is $\rho_a$. Two sections $\Delta x$ apart, one at $x$ and the other at $x+\Delta x$, are taken. If the total pressure force on the section at $x$ be denoted by $P$, the pressure force on the section at $x+\Delta x$ will be $P+A\rho g\ (dh/dx)\Delta x$. Hence, the difference of the two pressure forces is $A\rho g\ (dh/dx)\Delta x$. The inertial action of flow in the drift current above and in the gravity current below being ignored, the

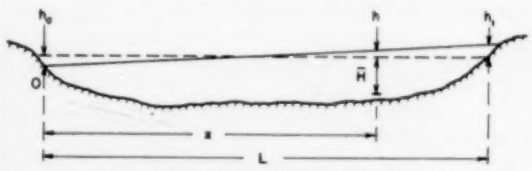


FIGURE 11. *Notation diagram for wind tides.*
$\overline{H}$ is the mean depth in the cross section of the lake at $x$

only remaining counterbalancing forces are the frictional forces amount to $B(\tau_s+\tau_0)\Delta x$. Thus, equating the forces and dividing by $\Delta x$, $A\rho g\ (dh/dx)=B\ (\tau_s+\tau_0)$, and since $A=B\ (\overline{H}+h)$, then

$$\frac{dh}{dx}=\frac{\tau_s+\tau_0}{\rho g(\overline{H}+h)}, \tag{13}$$

which is the wind tide equation for a lake of arbitrary shape. As the volume of water in the lake is not changed, the condition of continuity reduces to

$$\int_0^L Bh\,dx=0, \tag{14}$$

where L is the length of the lake axis.

Equations 13 and 14 may be changed into dimensionless forms. The average section depth may be expressed in terms of the average lake depth $H_0$,

$$H_0=\frac{1}{\overline{B}L}\int_0^L B\overline{H}\,dx. \tag{15}$$

The section surface width may be expressed in terms of the average lake width, $\overline{B}$,

$$\overline{B}=\frac{1}{L}\int^L B\,dx. \tag{16}$$

The distances along the axis may be expressed in terms of the lake length, $L$.

Putting

$$\sigma=\frac{\tau_s+\tau_0}{\rho g H_0}\cdot\frac{L}{H_0}, \tag{17}$$

$$\eta=\frac{h}{H_0}, \tag{18}$$

and

$$\zeta=\frac{x}{L}, \tag{19}$$

eq. 13 and 14 reduce to

$$\frac{d\eta}{d\zeta}=\frac{H_0/\overline{H}}{(1+\eta H_0/\overline{H})}\,\sigma, \tag{20}$$

and

$$\int_0^1 \frac{B}{\overline{B}}\,\eta\,d\zeta=0. \tag{21}$$

It is important to remark that $\sigma$ is the parameter of stress, $\eta$, the parameter of wind tide, $\zeta$, the parameter of distance. In a lake of arbitrary shape $H_0/\overline{H}$ and $B/\overline{B}$ are functions of $\zeta$.

As ordinarily $\eta$ is a small quantity, eq 20 may be written in the form

$$\frac{d\eta}{d\zeta}=\sigma\,\frac{H_0}{\overline{H}}\left(1-\frac{H_0}{\overline{H}}\,\eta\right). \tag{22}$$

The solution of the equation may be expressed in the form

$$\eta=\sigma F_1(\zeta)-\sigma^2 F_2(\zeta), \tag{23}$$

where

$$F_1(\zeta)=C_1+\int_0^\zeta \frac{H_0}{\overline{H}}\,d\zeta, \tag{24}$$

$$F_2(\zeta)=C_2+\int_0^\zeta \left(\frac{H_0}{\overline{H}}\right)^2 F_1(\zeta)\,d\zeta, \tag{25}$$

the quantities $C_1$ and $C_2$ being the constants of integration. Now, from eq 21

$$\int_0^1 \frac{B}{\overline{B}}\,F_1(\zeta)\,d\zeta=0, \tag{26}$$

and

$$\int_0^1 \frac{B}{\overline{B}}\,F_2(\zeta)\,d\zeta=0, \tag{27}$$

and these serve to evaluate the constants $C_1$ and $C_2$.

To carry out the determinations of the functions $F_1$ and $F_2$, it is necessary to obtain the shape quantities $\overline{H}/H_0$ and $B/\overline{B}$ for Lake Erie. These quantities as determined from the Lake Survey Office map of Lake Erie are shown in figures 12 and 13. Using the data from the figures, and following the method of computation shown above, the functions $F_1$ and $F_2$ are determined. These are plotted in figure 14. For the subsequent analysis the end values

$$\left.\begin{aligned} F_1(0)&=-0.641, \quad F_2(0)=0.323,\\ F_1(1)&=\ \ 0.512, \quad F_2(1)=0.118, \end{aligned}\right\} \tag{28}$$

are important.

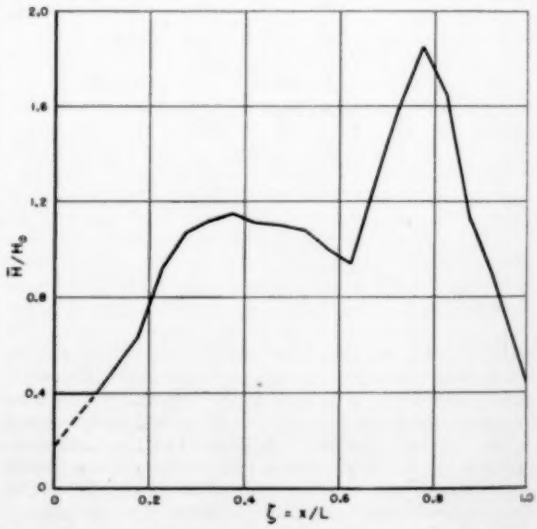


FIGURE 12. *Mean depths of Lake Erie as function of distance from Toledo.*

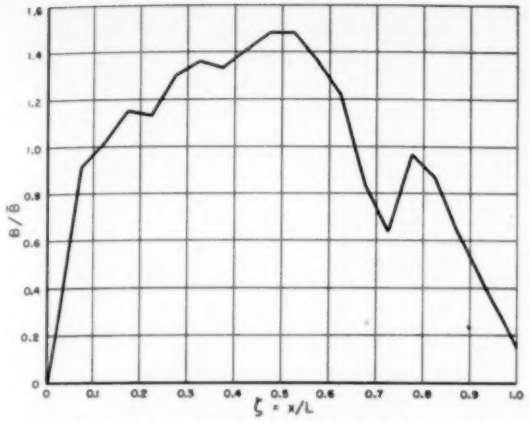


FIGURE 13. *Surface widths of Lake Erie as function of distance from Toledo.*

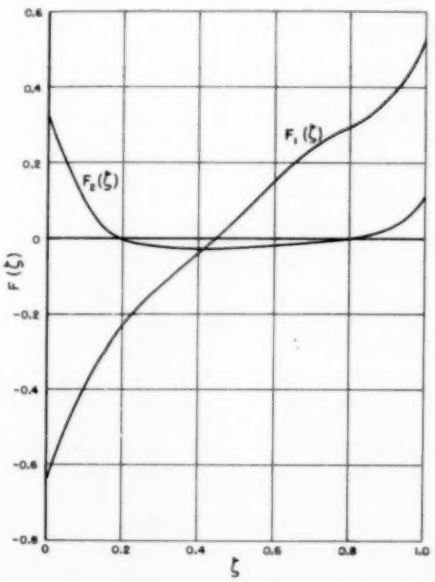


FIGURE 14. *Values of the functions $F_1$ and $F_2$ for Lake Erie.*

At this point, some observed values of the lake-water displacement may be compared with the theoretically determined curve of the analysis above. The most suitable way to represent the curve is to consider the ratio $2h/(h_1-h_0)$, where $h$ is the surface displacement at $x$, and $h_0$ and $h_1$ are the extreme values, as a function of $x/L$. Since $\sigma^2$ is a small quantity, $F_2$ may be neglected and thus,

$$\frac{2h}{h_1-h_0}=\frac{2F_1(\zeta)}{F_1(1)-F_1(0)}. \qquad (29)$$

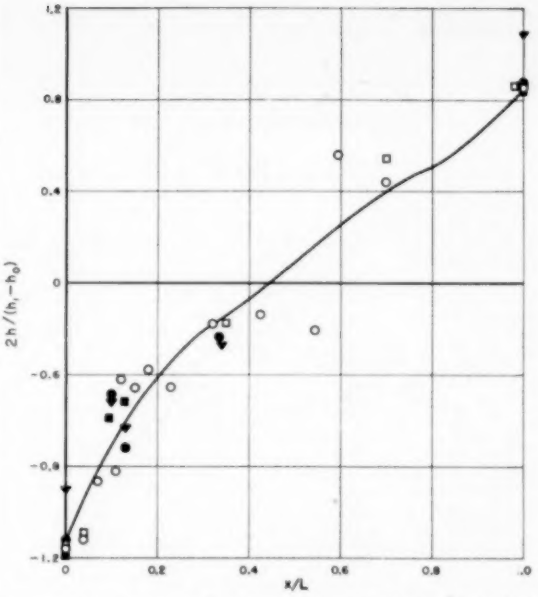


FIGURE 15. *Comparison of computed wind tides for Lake Erie with observations.*

□, Oct. 29, 1892 (Blunt). ○, Oct. 14, 1869 (Blunt). ▼, Sept. 25, 1941. ●, Jan. 2, 1942. ■, Jan. 3, 1942.

The quantity on the right hand, computed with reference to the values in figure 14, is shown in figure 15 by the full curve. The plotted points are from observations of different storms. The points represented by open circles and open squares are taken from data given by Blunt [2]. Apparently there appears to be a fairly good agreement between theoretical and observed values.

## 7. Evaluation of the Coefficient of Wind Stress

Representing the end values of $\eta$ as $\eta_0$ and $\eta_1$, it is seen from eq 21 that $\eta_0=\sigma F_1(0)-\sigma^2F_2(0)$, and $\eta_1=\sigma F_1(1)-\sigma^2F_2(1)$. Hence $(\eta_1-\eta_0)=\Delta\eta=\sigma[F_1(1)-F_1(0)]-\sigma^2[F_2(1)-F_2(0)]$, and introducing the values in eq 28, $\Delta\eta=1.153\ \sigma+0.205\ \sigma^2$, or $\sigma=0.867\ \Delta\eta-0.178\ \sigma^2$. Treating the second term in the right hand member as a small quantity,

$$\sigma=0.867\Delta\eta-0.134\Delta\eta^2.$$

Introducing values of $\sigma$ and $\eta$ from eq 17 and eq 18, and remembering that $\Delta H=h_1-h_0$, we have

$$\frac{\tau_s+\tau_0}{\rho g H_0}\frac{L}{H_0}=0.867\ \frac{\Delta H}{H_0}-0.134\left(\frac{\Delta H}{H_0}\right)^2. \qquad (30)$$

This is the relation that relates the wind stress to the total wind tide for Lake Erie.

Expressing the shear at the lake bottom as a fraction of the wind stress,

$$\tau_0 = n\tau_s, \tag{31}$$

the relation in eq 30 may be written as

$$\tau_s = \frac{1}{1+n}\left[0.867\,\frac{\Delta H}{H_0} - 0.134\left(\frac{\Delta H}{H_0}\right)^2\right]\frac{H_0}{L}\,\rho g H_0. \tag{32}$$

Introducing the definition of the coefficient of wind stress,

$$\tau_s = \chi \rho_a V^2, \tag{33}$$

where $\rho_a$ is the density of air, and $V$ the velocity of the wind, we have from eq 32

$$\chi = \frac{0.867}{1+n}\left[1 - 0.16\,\frac{\Delta H}{H_0}\right]\frac{\Delta H}{H_0}\,\frac{\rho}{\rho_a}\,\frac{gH_0}{V^2}, \tag{34}$$

which is the proper formula to evaluate the coefficient of wind stress from the total wind tide observed at Lake Erie. In the application of the formula the depth of water $H_0$ is taken as 58 ft., the ratio of the density of water to the density of air, $\rho/\rho_a$, as 1,250. The wind velocities $V$ are to be expressed in feet per second and the wind tides $\Delta H$ in feet. It may be supposed that the frictional stress of the lake bottom is about one-tenth of the wind stress. Accordingly, $n$ is 0.10.

Applying the above formula to the set of wind intensities and corresponding wind tides appearing in table 1, a set of values of the wind stress coefficient are obtained which are entered in table 3. The same

TABLE 3. *Coefficient of wind stress deduced from Lake Erie gales*

| No. | $V$ | $\chi \times 10^3$ | No. | $V$ | $\chi \times 10^3$ |
|---|---|---|---|---|---|
| | *mph* | | | *mph* | |
| 1 | 50.5 | 2.13 | 12 | 47.4 | 2.44 |
| 2 | 31.4 | 2.87 | 13 | 27.2 | 2.35 |
| 3 | 36.3 | 2.78 | 14 | 26.1 | 2.15 |
| 4 | 48.1 | 2.17 | 15 | 22.1 | 1.53 |
| 5 | 40.1 | 2.73 | 16 | 51.3 | 2.88 |
| 6 | 38.9 | 2.63 | 17 | 38.8 | 2.64 |
| 7 | 34.7 | 2.76 | 18 | 35.7 | 2.96 |
| 8 | 43.2 | 2.23 | 19 | 40.4 | 3.22 |
| 9 | 33.1 | 1.78 | 20 | 19.5 | 2.68 |
| 10 | 34.3 | 2.71 | 21 | 34.2 | 2.99 |
| 11 | 45.1 | 2.52 | 22 | 35.7 | 2.77 |

data are plotted in figure 16 as full circles. Plotted in the same figure as open circles are the wind stress coefficients which Neumann obtained in an examination of the Pelman observations for the Gulf of Bothnia [7]. Neumann's original values were reduced to correspond to winds 25 ft above the surface of the water.

An examination of figure 16 reveals that in the region of the higher wind velocities the coefficient of wind stress is practically independent of the velocity of the wind. Furthermore, the coefficient of wind stress for the two bodies of water are of like value. The average value of the individual determinations is 0.00254 for Lake Erie, and 0.00236 for the Gulf of

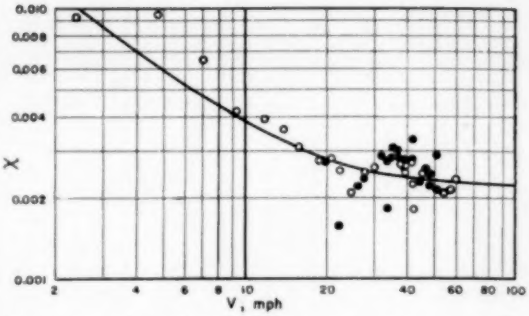


FIGURE 16. *Comparison of coefficients of wind stress in Lake Erie and the Gulf of Bothnia.*
●, Lake Erie. ○, Gulf of Bothnia.

Bothnia. Now, the data from the Gulf of Bothnia for low wind velocities indicate that for this region the coefficient of wind stress is not constant but decreases with increasing wind. At the moment no similar data are at our disposal for Lake Erie and efforts are being made to remedy this gap in our investigation.

## 8. Evaluation of Sea Roughness

We shall adopt for the determination of sea roughness the procedure used by Neumann. Writing eq 33 in the form $(V/V_*)^2 = \chi^{-1}$, substituting in

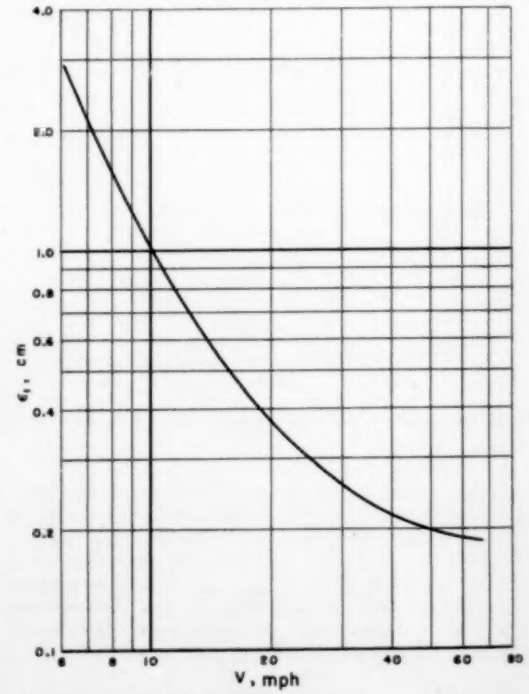


FIGURE 17. *Variation of sea roughness, $\epsilon_1$, with wind velocity, $V$.*

eq 1, and changing $\epsilon$ to $\epsilon_1$, there is obtained

$$\frac{1}{\kappa\sqrt{\chi}}=5.75\log\frac{z_{11}}{\epsilon_1}. \tag{35}$$

which relates the sea roughness $\epsilon_1$ to the elevation $z_{11}$ for which the wind is determined and the coefficient of wind stress $\chi$. In the present case, since $\chi$ is determined from wind velocities prevailing at a height of 25 ft, $z_{11}=25$ ft, or 762 cm. As mentioned above, the average value of the coefficient of wind stress from the Lake Erie data is 0.00254. This yields for the sea roughness the value $\epsilon_1=0.27$ cm. As will be remembered, in the computations required to reduce the city wind velocities to the lake velocities it was necessary to assume the value of the sea roughness beforehand. The assumed value was $\epsilon_1=0.3$ cm, and this selection is now seen to be satisfactory.

The full line drawn through the data points of figure 16 may now be used to investigate the variation of sea roughness with wind velocity. Using values from the curve and the formula above, eq 35, the results of the computations are given in figure 17 in the form of a curve. With increasing wind velocities the magnitude of the roughness decreases. When the higher wind velocities are attained, the roughness approaches a constant value, practically.

We refrain at the present moment from discussing the theoretical significance of the facts that both the coefficient of wind stress and the sea roughness decrease with increasing wind velocities.

## 9. References


[1] John R. Freeman, Regulation of the Great Lakes, Report to Board of Trustees of the Sanitary District of Chicago, p. 201. (1925).

[2] Wm. T. Blunt, Effects of gales on Lake Erie, Report of U. S. Deep Waterways Commission, p. 155 (1897).

[3] L. Prandtl, Meteorologische Anwendung der Strömungslehre, Beitrage zur Physik der freien Atmosphäre, **19,** p. 188. (1932).

[4] M. Siotani and G. Yamamato, Atmospheric turbulence over the large city. J. Meteorl. Soc. Japan, 2d Series, **27,** 111. (1949).

[5] C. G. Rossby and R. B. Montgomery, The layer of frictional influence in wind and ocean currents; Papers in Physical Oceanography and Meteorology, **III,** No. 3, Cambridge, Mass.

[6] Benjamin C. Kadel, Anemometer records on a Buffalo office building compared with those secured near the surface of Lake Erie. Monthly Weather Rev. (April 1917).

[7] Gerhard Neumann, Über den Tangentialdruck des Windes und die Rauhigkeit der Meeresüberfläche, Zeit. für Meteor. Year 2, p. 193 (1948).


Washington, November 3, 1952.

Journal of Research of the National Bureau of Standards Vol. 50, No. 2, February 1953 Research Paper 2397

# Twisted Square Plate Method and Other Methods for Determining the Shear Stress-Strain Relation of Flat Sheet *[1]

Walter Ramberg and James A. Miller

A method is presented for determining the stress-strain relation in shear for isotropic flat sheet. The method requires measurements of deflection or of extreme fiber bending strain in the center portion of a twisted square plate. The octahedral stress derived from the stress-strain curve in shear for a twisted plate of aluminum alloy agreed within about 5 percent with the octahedral stress derived from tensile and compressive tests of the same material. The difference was much greater for specimens of mild steel with a definite yield point. Unfortunately, the method is difficult to perform on thin sheet because of the small size of the specimen. An examination of alternate methods indicates particular promise for the use of an annulus of constant thickness.

## 1. Introduction

There has long been an interest in the stress-strain relations in shear of materials in the form of sheet. The interest has become more pronounced as working stresses and strains have increased and as it has become apparent that the mechanical properties of thin sheet could not be deduced directly from mechanical tests of heavier sections. The most satisfactory method, perhaps the only really satisfactory one, for determining the stress-strain curve of thin material in shear requires the material to be in the form of tubing with circular section. As long as the tube material is isotropic, its stress-strain curve in shear can be computed conveniently from the torque-twist curve of the tube by following the procedure given in [1].[2]

There is no dearth of suggestions for methods of determining the stress-strain curve in shear of flat sheet. Figure 1 indicates 10 suggested methods for stressing thin sheet in shear that have come to the authors' attention. The first two methods deal with tubular specimens.

Method (a) is nothing more than the bending of a strip of the sheet into a tube of large diameter, which is then tested like the conventional long tube for which a satisfactory theory exists [1]. The tube would have to have a large diameter so that the strains introduced in bending the strip would be small compared to the strains to be measured. Difficulties might be experienced with deviations from the theoretical uniform shearing stress caused by variations in clamping forces along the edges of the specimen. Difficulties might be experienced also with the discontinuity at the joint and with the transmission of sufficient torque to obtain stresses in the plastic range.

Method (b) was suggested to one of the authors by J. M. Frankland of Chance Vought Aircraft. Four strips of the sheets are assembled into a tube of square section. The strips will be subjected to a uniform shearing stress by equal and opposite torques applied to the ends, if the torsional rigidity of the joints along the four corners is negligible compared with the torsional rigidity of the tube as a whole. It is probable that this corner effect is not negligible for tubes that are sufficiently thick-walled to transmit, without buckling, torques that extend the shearing stresses into the plastic range.

Several methods have been suggested for stressing a specimen of sheet in shear by forces acting in the plane of the sheet.

Method (c) is the well-known square-picture-frame method, in which a square specimen is held between four pairs of rigid clamping bars with pin joints at the corners. The specimen will be placed in a state of uniform shear by equal and opposite forces acting at opposite corners of the frame, provided that the sheet is perfectly flat, the clamping bars are infinitely rigid, the edge effect due to deviations from ideal clamping does not extend into the middle portion of the sheet, and the pin joints are frictionless.

Method (d) tries to get around the difficulties with the edge effect in method (c) by making the specimen long so that the shearing stress is practically uniform along the middle portion of the specimen. However, an end effect will remain because the shearing stress reduces to zero at the corners. This end effect may be evaluated by making tests of the same material in picture frames of different lengths. The procedure would be costly and time consuming.

Method (e) was used by Coker and Filon [2] and Bollenrath [3] to stress thin sheet in shear. The loads are applied symmetrically to subject each one of the two "bays" of the specimen to a state of stress in which the shearing stress along the center line of each bay varies from zero at the ends to a nearly constant value near the middle. As in method (d), the end effect may be eliminated by testing specimens of different lengths.

Method (f), suggested by W. R. Osgood, subjects a single strip to a state of stress which approximates

*This paper is based on work sponsored by the National Advisory Committee for Aeronautics and the Mechanics Branch, Office of Naval Research, U. S. Department of the Navy.

[1] The major portion of this paper was presented before the First U. S. National Congress of Applied Mechanics in Chicago on June 11 to 16, 1951. It was published in the Proceedings of that Congress under the title "Determination of Stress-Strain Curve in Shear by Twisting Square Plate."

[2] Figures in brackets indicate the literature references at the end of this paper.

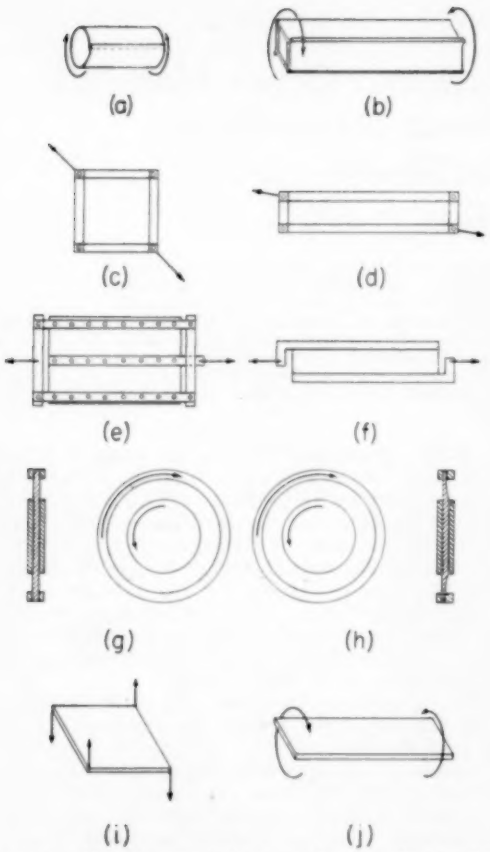


FIGURE 1. *Methods suggested for stressing thin sheet in shear.*

that in each bay of the specimen for method (e).

Method (g) avoids end effects by testing the sheet in the form of an "endless strip" or annulus. Equal and opposite torques are applied at the inner and outer edges of the annulus. The method has the advantage that, except near the periphery and the inner circle, the shearing stresses would be known accurately, for isotropic sheet, in the plastic as well as in the elastic range. There are some disadvantages, however. The shearing stress varies inversely as the square of the radius of the circle along which it acts. Hence there will be a nonlinear strain variation along the gage length of any finite gage mounted at 45° to the tangential direction. As a result, the average strain along the gage will differ from the strain at the midpoint of the gage, unless the annulus is large enough to make the nonlinear variations negligible. If the annulus is large enough, it may be difficult to apply sufficient torque to stress the material into the plastic range. The testing machine would require heads that are rotatable about their axis only, to prevent bending of the specimen by rotation about other axes. The method would give only an average stress-strain curve for anisotropic sheet.

Method (h) eliminates some of the difficulties of method (g). The annulus is machined into a disk that varies in thickness inversely as the square of the radius. The material in the annulus will be subjected in that case to a uniform shearing stress by equal and opposite torques applied at the inner and outer edge. The disk must be sufficiently thick near the periphery to develop strains in the plastic range before buckling occurs and the variation in thickness with radius must be small enough at the radius where the strains are measured to assure a practically uniform shearing stress throughout the thickness. A practical difficulty is that of machining the specimen accurately to the desired thickness variation without changing the properties of the material by the machining operation.

The methods so far mentioned subject the sheet to a shearing stress that is substantially uniform throughout the thickness of the sheet. In the remaining two methods the shearing stress is varied in the thickness direction from one extreme to an opposite extreme.

In method (i) a state of shear is produced in a square plate by twisting the plate into an anticlastic surface by equal and opposite tranverse forces applied to adjacent corners. The state of shear will be uniform for planes at a fixed distance from the median plane which will undergo zero shearing stress. The upper and lower faces of the plate will be under equal and opposite shearing stress. Objections might be raised against this method in so far as it neglects deviations from uniform shear due to various causes, such as having large transverse stresses near the corners and no shearing stresses along the edges. These objections will be discussed in detail in the body of the paper. Experimental difficulties may arise in applying the corner loads to the specimen without interfering with strain and deflection measurements on the faces of the plate.

Method (j), suggested by A. H. Stang, uses a much simpler scheme for producing a state of stress similar to that in method (i). A specimen in the shape of a long strip is placed in a state of shear by applying equal and opposite torques to the ends of the strip. Shearing strains can be measured with strain gages or they can be obtained from the twist per unit length of the strip. However, if the strip is made long enough to eliminate end effects, it is likely to deflect laterally. This will superimpose bending stresses on the torsional stresses. The same objections might be raised in this case as in case (i) with regard to edge effects. The shearing stress at the extreme fiber will be practically constant in the center portion, far from the edges of the strip, but it will decrease rapidly to zero as the edges are approached. The value of the extreme fiber shearing stress near the center of the strip will depend on this edge effect. It can be computed exactly in the elastic range, but no exact solution is known for the plastic range.

Consideration of the above 10 methods suggests that at least three of them, the square-picture-frame method (e), the annulus of constant thickness method

(g), and the twisted-square-plate method (i), should be tried out experimentally.

An experimental study of method (c), the square picture frame, was conducted by Wm. R. Osgood about 5 years ago. Method (c) was selected because it appeared to have particular promise and because it had been used in the aircraft industry to estimate shear properties of sheet. A fixture had been developed at the El Segundo Plant of the Douglas Aircraft Co. to make such tests. A duplicate of this fixture was obtained, and tests were made at the National Bureau of Standards for the National Advisory Committee for Aeronautics on several 4.5×4.5×0.063 in. 24S–T aluminum alloy plates. The results were disappointing. They were reported to the NACA, but were not published. The strains were far from uniform even in the center portion of the plate farthest from the edges. The extreme fiber strains in this optimum region deviated up to 10 percent from the average strain. The deviations persisted even after an attempt had been made to improve the conditions of clamping along the edges by remachining parts of the clamping fixture.

Two years after completion of the work for the NACA, it was decided to try method (i), the twisted square plate, since Nadai had shown in 1915 [4] that this method provided a simple means for determining the shear modulus of sheet material. More recently the test has been extended to orthotropic materials at the Forest Products Laboratory [5] to determine the shear moduli of wood.

## 2. Nomenclature

The following nomenclature is used in the paper:

$a$ = half-span for deflection measurements.
$b$ = width of specimen.
$E$ = modulus of elasticity in tension or compression.
$G$ = modulus of elasticity in shear.
$h$ = thickness of specimen.
$m$ = moment per unit length.
$M$ = bending moment.
$M_t$ = twisting moment.
$P$ = load at each corner of plate.
$R$ = radius of curvature along diagonals of plate.
$u$, $v$, $w$ = displacements parallel to $x$-, $y$- and $z$-axes, respectively.
$x$, $y$ = axes parallel to diagonals of plate, also planes normal to the corresponding axes.
$x'$, $y'$ = axes parallel to edges of plate, also planes normal to the corresponding axes.
$z$ = axis parallel to thickness of plate, also plane normal to $z$-axis.
$\gamma$ = shearing strain.
$\gamma_o$ = octahedral strain.
$\epsilon$ = normal strain.
$\nu$ = Poisson's ratio.
$\sigma$ = normal stress.
$\tau$ = shearing stress.
$\tau_o$ = octahedral stress.

## 3. Principle

### 3.1. Elastic case

An elastic square plate will be in a state of pure shear, in which the shearing stress is proportional to the distance from the neutral surface of the plate when the plate is bent into an anticlastic surface with equal and opposite principal curvatures. The bending of the plate into such an anticlastic surface produces equal and opposite extreme fiberbending stresses along the two principal axes. Nadai has shown that this remarkably simple state of stress may be realized by applying equal and opposite tranverse forces to adjacent corners of the plate.

Nadai's proof [4] makes use of Saint-Venant's principle of the equivalence of equipollent loads. Nadai notes that for a load $P$ at each corner, each edge of the plate is loaded by equal and opposite forces $P/2$ acting at two corners (fig. 2). The load along the edge will remain unchanged upon applying balancing forces $\pm P/2$ at frequent intervals along the edge, as indicated in fig. 2. Any element of length of edge $\Delta x'$ between two adjacent equal and opposite forces $P/2$ will then be subjected to a twisting moment $(P/2)\Delta x'$. According to Saint-Venant's principle, this edge load is equivalent to any edge load which results in a constant twisting moment per unit length

$$m_{x'y'} = \frac{1}{\Delta x'} \frac{P}{2} \Delta x' = \frac{P}{2}, \tag{1}$$

uniformly distributed along the edge of the plate. The stress distribution, in regions of the plate sufficiently far from the edge to satisfy Saint-Venant's principle, will then be that corresponding to uniform twisting moments $+m_{x'y'}, -m_{x'y'}$ in the $x'$, $y'$ planes, normal to the $x'$, $y'$ axes, respectively. The twisting moments $\pm m_{x'y'}$ are associated with principal bending moments $m_x$, $m_y$ on the $y$, $x$ planes normal to the diagonals of the plate. Equilibrium of moments acting on the edges of a triangular element of the plate (fig. 3) bounded by planes parallel to the $x$, $y$, and $y'$ planes shows that

$$m_x = m_y = -m_{x'y'} = -P/2. \tag{2}$$

The plate is bent into an anticlastic surface by equal and opposite bending moments per unit length $P/2$ acting on the $y$, $x$ planes normal to the diagonals of the plate. The surface will have its planes of prin-

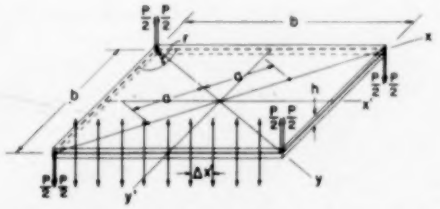


FIGURE 2. *Twisting of square plate by forces on corners.*

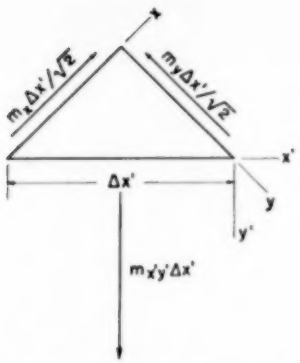


FIGURE 3. *Edge moments acting on element of twisted square plate.*

cipal curvature normal to the diagonals of the plate. If $R$ is the radius of curvature along the diagonals, the deflection relative to a plane tangent to the center of the plate is given by

$$w=\frac{x^2-y^2}{2R}. \tag{3}$$

The distribution of strain and of stress throughout the plate may be computed on the assumption of the Kirchhoff plate theory that plane sections remain plane. The normal strains $\epsilon_x$, $\epsilon_y$ must then increase linearly with distance from the neutral fiber

$$\epsilon_x=\frac{2z}{h}\,\epsilon_1 \quad \epsilon_y=\frac{2z}{h}\,\epsilon_2, \tag{4}$$

where $\epsilon_1$, $\epsilon_2$ are the principal extreme fiber strains; $z$, the distance from neutral fiber; and $h$, the thickness of plate. The maximum shearing strain on the $z$ plane is

$$\gamma=\gamma_{x'y'}=\epsilon_x-\epsilon_y=\frac{2z}{h}\,\gamma_1, \tag{5}$$

where $\gamma_1$ is the shearing strain at the extreme fiber $\gamma_1=\epsilon_1-\epsilon_2$. Because of the antisymmetry of the deformation $\epsilon_1=-\epsilon_2$, so that

$$\gamma_1=2\epsilon_1. \tag{6}$$

The shearing stress corresponding to the strain $\gamma$ is given by

$$\tau=G\gamma \tag{7}$$

nside the elastic range. The twisting moment per unit length is given by

$$m_{x'y'}=\int_{-h/2}^{h/2}\tau z\,dz. \tag{8}$$

Substituting (1), (7), (5), and (6) in this equation gives

$$\frac{P}{2}=\frac{1}{3}\,\epsilon_1 G h^2. \tag{9}$$

From which

$$G=\frac{3}{2h^2}\,\frac{P}{\epsilon_1}. \tag{10}$$

Hence the shear modulus can be computed from the slope $P/\epsilon_1$ of a plot of load against extreme fiber strain by substituting $P/\epsilon_1$ in (10).

The shear modulus may be determined also from the deflection $w_a$ of the center of the plate relative to a line connecting points a distance $a$ from the center along one of the diagonals, figure 2. If plane sections are assumed to remain plane, the curvature $1/R$ along the diagonal $x$ is given by the familiar formula

$$\frac{1}{R}=\frac{d^2w}{dx^2}=\frac{\epsilon_1}{h/2}, \tag{11}$$

where $w$=normal deflection. Substituting (11) in (9) gives

$$w_a=\frac{\epsilon_1 a^2}{h}=\frac{3}{2}\,\frac{a^2}{h^3}\,\frac{P}{G}, \tag{12}$$

so that

$$G=\frac{3}{2}\,\frac{a^2}{h^3}\,\frac{P}{w_a}, \tag{13}$$

which gives the desired relation between shear modulus and center deflection under a given load.

### 3.2. Extension into plastic range

Equations (1) to (6) apply beyond the elastic range as long as plane sections remain plane. Equation (8) for the relation between twisting moment and shearing stress applies beyond the elastic range also. We may replace $z$ in the integral of that equation by $\gamma$, using eq (5) so that eq (8) becomes

$$m_{x'y'}=\frac{P}{2}=\frac{h^2}{2\gamma_1^2}\int_0^{\gamma_1}\tau\gamma\,d\gamma. \tag{14}$$

The change in load $dP$ corresponding to a small change in extreme fiber shearing strain $d\gamma_1$ is obtained by differentiating this equation in respect to $\gamma_1$ with the result

$$\frac{dP}{d\gamma_1}=-\frac{2h^2}{\gamma_1^3}\int_0^{\gamma_1}\tau\gamma\,d\gamma+\frac{h^2}{\gamma_1^2}\,\tau_1\gamma_1=\frac{1}{\gamma_1}\,(-2P+h^2\tau_1), \tag{15}$$

where $\tau_1$ is the extreme fiber shearing stress. Solving this equation for $\tau_1$ gives

$$\tau_1=\frac{1}{h^2}\left[\gamma_1\,\frac{dP}{d\gamma_1}+2P\right]. \tag{16}$$

The extreme fiber shearing strain can be computed simply from measured values of extreme fiber bending strain $\epsilon_1$ or from measured values of deflection $w_a$ by making use of eq (6) and (12)

$$\gamma_1=2\epsilon_1=\frac{2hw_a}{a^2}. \tag{17}$$

The stress-strain curve in shear can be derived, therefore, from measurements of $P(\epsilon_1)$ or $P(w_a)$ by using (17) to compute the shearing strain $\gamma_1$, plotting $P(\gamma_1)$, and computing $\tau_1$ from the ordinates and slope of $P(\gamma_1)$ in accordance with eq (16).

It is interesting to note that eq (16) is of the same form as the equation

$$\sigma_1 = \frac{2}{bh^2}\left[\epsilon_1 \frac{dM}{d\epsilon_1} + 2M\right], \tag{18}$$

which is derived by Nadai [6] to compute the stress-strain curve $\sigma_1(\epsilon_1)$ from the bending moment-strain curve $M(\epsilon_1)$ for a rectangular beam of width, $b$, and height, $h$, in pure bending; $\epsilon_1$ is the extreme fiber bending strain produced by the bending moment, $M$. The identity in form of eq (16) and (18) might be expected because the square plate is bent plastically into an anticlastic surface by equal and opposite bending moments per unit length about axes at right angles to each other.

## 4. Design of Specimen

In designing the specimen, consideration must be given to practical deviations from the theoretical behavior because the theory neglects edge effects, membrane stresses, and deformation by transverse shearing forces. These effects must be considered in some detail in order to dimension the specimen so that the deviations from ideal behavior can be either neglected or taken into account.

The edge effect will be considered first. In the theory, the concentrated forces at the corners are replaced by twisting moments uniformly distributed along each edge, which are applied by horizontal shearing forces rather than the vertical forces shown in figure 2. It follows that the theoretical solution will hold only for regions of the plate at a sufficient distance from the edges, to make Saint-Venant's principle applicable. Dimensional reasoning indicates that the "sufficient distance" should be proportional to the thickness, $h$. The factor of proportionality may be estimated roughly by examining cases for which solutions have been obtained from the theory of elasticity.

The plane stress solution for a bar of constant width $h$ compressed by a concentrated load at the center of the free ends is given in [7]. This shows that the maximum compressive stress, which becomes infinite directly under the load, differs less than 3 percent from the average stress at a distance $h$ from the end. Seewald's plane stress analysis of the local stresses near a concentrated transverse load acting at the center of a slender beam of rectangular section with simple supports at the ends [8] shows that these stresses become negligible compared to the extreme fiber bending stresses derived from simple beam theory at a distance from the load greater than the depth of beam.

This suggests that the errors resulting from the application of Saint-Venant's principle will be small in regions of the plate at a distance from the edge

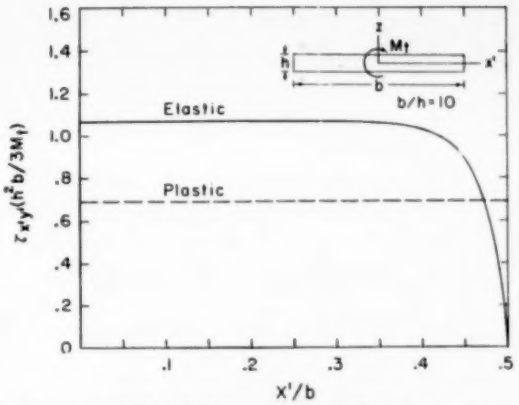


FIGURE 4. *Distribution of extreme fiber shear stress* $(\tau_{x'y'})_{max}$ *along surface of strip with* $b/h=10$.

which is greater than $h$. This condition is easily satisfied for a plate that is thin in relation to its lateral dimensions. Unfortunately, it will be shown below that a very thin plate is not acceptable because it will develop appreciable membrane stresses under the loads required to produce yielding in shear. The membrane stresses are negligible only if the plate has a width not exceeding a few times the thickness. In such a plate, it is probable that the deviations from the assumed stress distribution at the edges will have an appreciable effect upon the magnitude of the stresses in the central portion of the specimen.

A correction for the edge effect in the twisted square plate was suggested to the authors by their associate, Samuel Levy. He pointed out that the twisting of an elastic square plate can be considered as a special case of torsion of a rectangular plate considered by Kelvin and Tait [9]. The elastic stress distribution at crosssections of a long rectangular plate far from the ends is given in [10]. The extreme fiber shearing stress is plotted in figure 4 for the case $b/h=10$ which was chosen, after a preliminary analysis, as a practical compromise for the twisted plate. Kelvin and Tait [11] showed that the shearing stresses $\tau_{z'y'}$ parallel to the plane of the strip resist only one-half of the external twisting moment $M_t=Pb$ transmitted by each transverse section of the strip. The other half is resisted by the transverse shearing stresses $\tau_{y'z}$ acting on the section.

A redistribution of stresses will take place as the strip is twisted beyond the elastic range. The nature of this redistribution becomes clear by considering the extreme case of stress in a twisted strip of perfectly plastic material when all the material has yielded. This case was solved by Nadai [12] with the sand heap analogy. The resultant stress distributions are shown dotted in figures 4 and 5. Integration of the stresses for the perfectly plastic state shows that, in the plastic as well as the elastic range, $M_t/2$ is resisted by the shearing stresses $\tau_{x'y'}$ parallel to the surface of the strip and $M_t/2$ by the

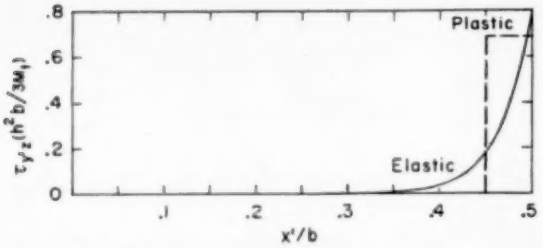


FIGURE 5. *Distribution of transverse shear stress* $(\tau_{y'z})_{max}$ *along x'-axis of strip with section* $b/h=10$.

shearing stresses $\tau_{y'z}$ normal to the surface of the strip.

The shear stress distribution of figures 4 and 5 and the condition that one-half of the twisting moment $M_t$ is resisted by $\tau_{x'y'}$ and the other by $\tau_{y'z}$ show that the stresses across transverse sections of the strip can be approximated by application of equal and opposite concentrated forces near the ends of the section and a uniformly distributed twisting moment along the entire section.

This distribution of equivalent external forces coincides with that shown in figure 2 as acting on the edge $y'=b/2$ of the square twisted plate provided that the corner forces $P$ are moved in from the corners by a small distance to make $P/2$ act at the same point as the resultant of the transverse shearing stresses $\tau_{y'z}$ which are shown in figure 5 for points along the $x'$-axis. It may be concluded that the distribution of forces acting on two edges of the square plate in figure 2 nearly balances the shearing stresses acting across any transverse section of a long strip of width, $b$, and thickness, $h$, which is twisted by a torque $M=Pb$ applied to the ends. The square plate can be regarded, therefore, as a portion of such a long twisted strip with a distribution of shearing stress across the section $y'=0$ which approximates that in the transverse sections of the strip. Consequently, the extreme fiber shearing-stress distributions indicated in figure 4 would also apply to the square plate. The shearing stress in the central portion would be greater than that computed from eq (16) because of the above-mentioned edge effect. In the elastic case, this increase would be about 7 percent for $b/h=10$, according to figure 4.

In general, we find from [10] that the extreme fiber shearing stress in the central portion of the longer sides of a rectangular section can be expressed by

$$\tau_{1c}=\frac{\tau_1}{3k_2}, \tag{19}$$

where $k_2$ is a factor depending on $b/h$. For values of $b/h>5$, the relationship reduces to

$$\frac{\tau_{1c}}{\tau_1}=\frac{1}{1-0.63h/b}. \tag{20}$$

In the limiting case of a perfectly plastic material which has yielded throughout the section, we have from the sand-heap analogy [12]

$$\frac{\tau_{1c}}{\tau_1}=\frac{1}{1-0.333h/b}. \tag{21}$$

For $b/h=10$, we obtain from (20) and (21)

$$\left.\begin{aligned}\tau_{1c}&=1.067\tau_1 \quad \text{elastic case}\\ \tau_{1c}&=1.034\tau_1 \quad \text{plastic case}\end{aligned}\right\}. \tag{22}$$

The actual correction for edge effect beyond the elastic range should lie somewhere between the limits given by eq (20) and (21). It should be closer to (20) as long as the plastic yielding is localized in the outer fibers of the plate.

The effect of membrane stresses will be considered next. The stiffening effect of membrane stresses is noticeable experimentally during twisting of a thin square plate as the transverse displacements $w(x,y)$ become comparable to the thickness of the plate. Figure 6, taken from Figure 11 of [13] shows the effect for a $7.2\times7.2\times0.126$-in. plate of 24S-T aluminum alloy. The two straight lines in the figure are the strains $\epsilon_1$ along the diagonals computed from eq (9) for the linear elastic case. It is seen that the measured load $P$ agrees closely with the calculated values at very small strains, but that it deviates increasingly with increasing strains. The deviation is close to 30 percent for a strain $\epsilon_1=0.0008$.

The effect is analyzed in the appendix for the elastic range on the assumption that the transverse deflection of the plate continues to be given by eq (3). Equation (67) in the appendix shows that

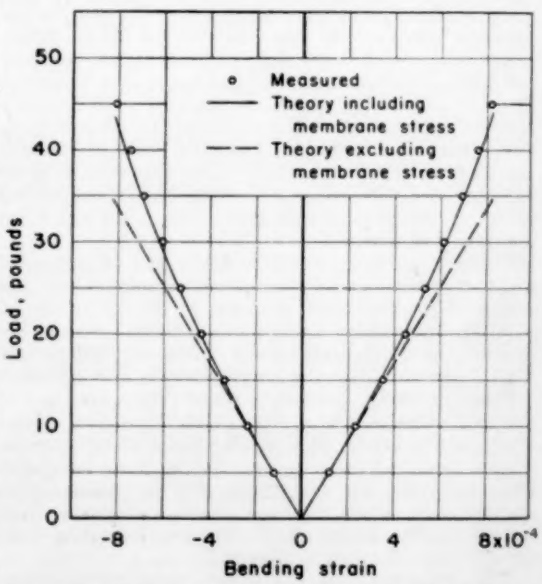


FIGURE 6. *Extreme fiber bending strains at center and along diagonals of* $7.2\times7.2\times0.126$ *in. plate of aluminum alloy* 24S–T *twisted by transverse forces P applied at the corners.*

the relative error in extreme fiber bending strain $\epsilon_1$ caused by the stiffening effect, is equal to

$$\frac{\Delta\epsilon_1}{\epsilon_1}=0.03666\left(\frac{b}{h}\right)^4\epsilon_1^2. \tag{23}$$

The error goes up with the square of the extreme fiber strain $\epsilon_1$ and with the fourth power of the width/thickness ratio, $b/h$. It may be made small by making $b/h$ small.

Lastly, consideration will be given to the transverse shearing stress. The effect of transverse shearing stress will be negligible as long as this stress is very small compared to the extreme fiber shearing stress parallel to the plane of the plate. The average transverse shearing stress $\tau_r$ on a section of a cylinder at a radius, $r$, from one of the corners of the plate (fig. 2) is

$$\tau_r=\frac{P}{\pi rh/2}. \tag{24}$$

The extreme fiber shearing stress in the elastic range is from (7), (6), and (9)

$$\tau_1=G\gamma_1=2G\epsilon_1=3P/h^2. \tag{25}$$

The ratio of the average transverse shearing stress to the extreme fiber shearing stress in the elastic range becomes

$$\frac{\tau_r}{\tau_1}=\frac{2}{3\pi}\frac{h}{r}=0.2\frac{h}{r}. \tag{26}$$

This requires $h/r$ to be small, that is, the effect becomes negligible as the plate is made very thin.

Equations (20), (23), and (26) were used to estimate the deviations from ideal behavior caused by edge effect, membrane strain, and transverse shear for square plates with width/thickness ratios $b/h=5$, 10, 20. The results, rounded off to the nearest percent, are given in table 1.

TABLE 1.

| | $b/h$ | | |
|---|---|---|---|
| | 5 | 10 | 20 |
| Edge effect $(\tau_{1e}/\tau_1)-1$ | 0.13 | 0.07 | 0.03 |
| Membrane stiffening effect $\Delta\epsilon_1/\epsilon_1$ | .09 | .02 | .38 |
| Transverse shear effect $\tau_r/\tau_1$ | .20 | .10 | .05 |

In table 1 $(\tau_{1e}/\tau_1)-1$ is taken as the correction according to eq (20) for the elastic case. The extreme fiber shearing strain $\gamma_1=2\epsilon_1$ is assumed as 0.016 to place it well beyond the elastic range. The membrane stiffening effect was computed from eq (23) for the elastic range, since the stiffening will be relatively insensitive to the yielding that takes place near the extreme fibers of the twisted plate. The average transverse shearing stress was computed for a radius $r=b/5$ from the corner leaving the inner portion of the plate $0.2<r/b<0.7$ available for strain and displacement measurements.

Table 1 indicates that a plate with $b/h=10$ provides a fair compromise between the three different disturbing effects that were considered.

## 5. Tests

### 5.1. Test procedure

Specimens were made from aluminum alloy 75S–T6 sheet nominally 0.125 in. thick for which the tensile and compressive stress-strain curves had been obtained both parallel and perpendicular to the direction of rolling [14]. This material was selected because of its approximately isotropic properties. The specimens were taken from near the center of the sheet, where there was little variation in thickness. The specimen selected for trying out the procedure was 0.1324 in. thick and 1.25 in. square. This gave a width/thickness ratio $b/h=9.44$, which approximates the value $b/h=10$ suggested in the previous section. The specimen was large enough to provide space for mounting a deflectometer and for attaching strain gages at several locations. It had additional material at each corner, as shown in figure 7, to reduce the concentration of transverse shearing stress at the corners. A conical seat was machined at each corner of the square, a pair on one side at the ends of a diagonal and a pair on the other side at the ends of the other diagonal.

The specimen S, figure 8, was loaded through 1/8-in. steel balls in the conical seats at the corners with a beam-and-poise screw-type testing machine of 50,000-lb capacity used in the 5,000–lb range. In this manner of loading, the load acted along vertical lines through the centers of the balls, which were almost a thickness of the sheet from the neutral surface. This resulted in the moment becoming larger instead of less as the specimen twisted. This effect is opposite in sign to the stiffening effect of membrane stresses previously mentioned. Two corners of the specimen rested upon balls. One of these was seated in a block of steel resting on the upper head of the testing machine, and the other was seated in the block A, figure 8, which was free to move on

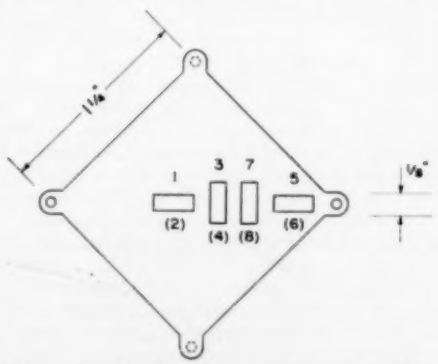


FIGURE 7. *Location of wire strain gages on plate.*

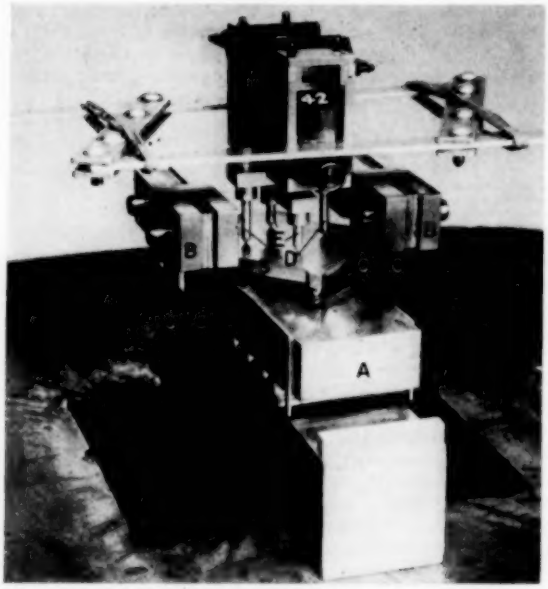


FIGURE 8. *Plate under load with deflectometer in position for measuring deflections along principal diagonals.*

rollers in the direction of the diagonal. The other two corners were loaded by means of a hanger connected to the loading head of the machine by a rod having a ball-and-socket joint at each end. The upper cross pieces, B, in which the balls were seated are shown in figure 8. They were connected to a common piece below the head by steel tapes, C. The ball joints at each end of the rod and the pin joints at each end of the tapes had the effect of equalizing the load on the corners of the plate.

SR–4 type A–7 strain gages were mounted on the specimen in pairs on opposite sides of the specimen. The gages were connected with an SR–4 model K portable strain indicator through a multiple-pole mercury-contact switch. A gage cemented to a piece of the sheet material was used as a temperature compensating gage. Since each portion of the specimen was subject to both tensile and compressive strains at right angles to each other, the gage-factor setting was taken as the axial sensitivity of the gage computed from the gage factor provided by the manufacturer and the data on axial and transverse sensitivities for gages of this type [15]. Strain readings were estimated to 0.1 division (0.000001). A correction was applied to compensate for the strain sensitive wire being farther from the neutral surface of the specimen than the surface of the sheet; each strain was multiplied by the ratio of the thickness of the specimen to the sum of the thicknesses of the specimen and the gage.

A deflectometer using two Tuckerman optical strain gages with 0.4-in. lozenges, figure 8, was used to measure deflections relative to the center of the plate. The Tuckerman strain gages were mounted so that their knife edges were connected to a pair of legs, D, placed along one diagonal of the plate, while their lozenges were connected to a pair of shorter legs, E, placed along the other diagonal. One of the gages was cemented to the cross piece holding the two longer legs. The knife edge of the other gage was mounted on a ¼-in. tube which was inserted in the cross piece midway between the two legs. The lozenges were actuated by a ¼-in. rod, which was screwed into the cross piece holding the two shorter legs and which was reduced at the lower end to pass through the tube with ample clearance. The lozenges were set near their lower limits of travel so that the vertical component of the clamping force would assist in maintaining contact of the two shorter legs with the specimen. The deflectometer was mounted on the specimen symmetrically with respect to the center with the point of one of each pair of legs in a small punch mark on each diagonal and the other in a scratch along the diagonal. The span was about 0.7 in. The deflectometer measured the sum of the deflections at the center with respect to each pair of points or twice such a deflection, since the loading was equal and opposite at each pair of corners. With this deflectometer, deflections could be read to the nearest 0.000002 in.

### 5.2. Test Results

#### a. Elastic Range

Wire strain gages were cemented on the specimen at locations 1 and 3, and 2 and 4, respectively opposite them on the other side; figure 7. The specimen and deflectometer were set up as shown in figure 8, and the specimen was loaded in the elastic range. The value of the shear modulus is from (6), (12)

$$G=\frac{\tau_{1c}}{\gamma_1}=\frac{\tau_{1c}}{2\epsilon_1}=\frac{\tau_{1c}a^2}{2w_ah}, \tag{27}$$

where $\tau_{1c}$ is the shearing stress after correction for edge effect. Within the elastic range, from (20) and (25),

$$\tau_{1c}=\frac{3P}{h^2(1-0.63h/b)} \tag{28}$$

or with $b/h=9.44$,

$$\tau_{1c}=3.21P/h^2. \tag{29}$$

Substitution of $\tau_{1c}$ in (27) gives the shear modulus in terms of either measured extreme fiber strain $\epsilon_1$, or measured center deflection $w_a$. Table 2 shows the values thus obtained from the initial linear portion of plots of deflectometer readings and wire strain-gage readings as a function of load $P$.

The last value of $G$ in table 2 was computed from

$$G=\frac{E}{2(1+\nu)}, \tag{30}$$

by substituting for the Young's modulus an average

TABLE 2. *Shear-modulus values measured at central portion of square plate*

| Obtained from— | $G$ |
|---|---|
| | *lb/in.²* |
| Deflectometer | $3.82\times10^6$ |
| Strain gage 1 | 3.87 |
| Strain gage 2 | 3.82 |
| Strain gage 3 | 3.84 |
| Strain gage 4 | 3.88 |
| Equation (30) | 3.90 |

value $E=10.37\times10^6$ lb/in.² obtained from tensile and compressive tests of the aluminum alloy 75S–T6 sheet, and for Poisson's ratio $\nu=0.33$, the nominal value for this alloy.

Table 2 shows that the experimental values of shear modulus agreed within 1.5 percent. The average for the wire gages was about 0.7 percent greater than the value obtained from the deflection data and about 1.2 percent less than the value computed from eq (30). A lower value from the deflection data would be expected because of the effect of transverse shear.

The deflectometer was removed, and gages 5 and 7, figure 7, and gages 6 and 8, respectively opposite them, were cemented to the specimen. The loading was repeated in the elastic range. The results are given in table 3.

TABLE 3. *Shear modulus values measured in outer portion of square plate*

| Obtained from gages | $G$ |
|---|---|
| | *lb/in.²* |
| 5 | $3.53\times10^6$ |
| 6 | 3.46 |
| 7 | 4.04 |
| 8 | 3.98 |

The results show greater strains at locations 5 and 6 than at any other location. This indicates a deviation from the uniform state of stress, which becomes serious in the corner portions of the plate.

### b. Plastic range

The specimen was loaded until a shear strain of about 2 percent was reached at the extreme fiber. Deflections were measured with the deflectometer and strain with the four central wire gages. The shear stress was partially corrected for edge effect by substitution of $\tau_1$, eq (16), in eq (20). Equation (20) was used beyond the elastic range to avoid discontinuity at the end of the elastic range. It should be an adequate approximation in the important region near the knee of the stress-strain curve because only a small proportion of the material would be in the plastic range.

The stress-strain data are plotted in figure 9. The values of $G$ determined both from the strain data and deflection data were a little over 2 percent higher than in the first test, the average value for the four wire gages being almost 1 percent above the value computed from (30). No explanation could be found for this small deviation.

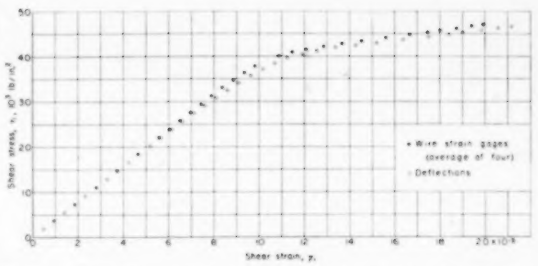


FIGURE 9. *Stress-strain curve in shear, aluminum alloy 75S–T6 sheet.*

### c. Comparison with stress-strain curves under axial load

It is interesting to compare the stress-strain curve in shear with that under axial load. Such a comparison can be made by deriving the octahedral stress-strain curve in each case [16]. The octahedral stress-strain curves for both states of stress should coincide if the maximum shear strain $\gamma_o$ on the octahedral plane (the plane defined as having a normal which makes equal angles with the three axes of principal stress) is a single-valued function of the maximum shearing stress $\tau_o$ on the octahedral plane, regardless of the direction and proportion of the principal stresses.

The octahedral stress-strain curve $\tau_o(\gamma_o)$ was computed from an average axial stress-strain curve $\sigma(\epsilon)$ by substitution in the following formulas [16]:

$$\tau_o=\frac{\sqrt{2}}{3}\sigma; \quad \gamma_o=\frac{\tau_o}{G}+\sqrt{2}\left(\epsilon-\frac{\sigma}{E}\right) \tag{31}$$

The axial stress $\sigma$ was obtained from tensile and compressive stress-strain curves of the material parallel to and perpendicular to the direction of rolling [14] as the average of the tensile and compressive stresses corresponding to a given axial strain $\epsilon$. The value of $G$ used, $3.93\times10^6$ lb/in.², was the average determined from the strain data in this test. The value of $E$ used, $10.37\times10^6$ lb/in.², was the average obtained from tensile and compressive tests on the sheet. The stress-strain curve in shear determined from the strain data, figure 9, was converted similarly into an octahedral stress-strain curve by substitution in

$$\tau_o=\sqrt{\frac{2}{3}}\tau_1; \quad \gamma_o=\frac{\tau_o}{G}+\sqrt{\frac{2}{3}}\left(\gamma_1-\frac{\tau_1}{G}\right) \tag{32}$$

The resulting curves of octahedral stress versus total strain $\gamma_o$ and versus permanent strain $\gamma_o-\tau_o/G$ are plotted in figure 10. It will be noted that the two stress-strain curves are in good agreement except for deviations up to 5 percent near the knee and at shearing strains exceeding 0.009.

In this connection, mention should be made of the much larger discrepancies found in exploratory twisting tests of a $0.125\times0.625\times0.625$-in. plate of SAE 1025 steel. These tests were made to extend the above comparison to a material with a pro-

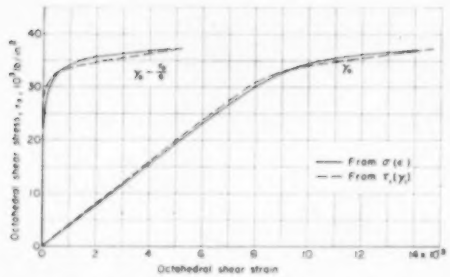


FIGURE 10. *Octahedral stress-strain curve, aluminum alloy 75S–T6 sheet.*

nounced yield point. The shear modulus was found to be in good agreement with the value computed from Young's modulus and Poisson's ratio. However, the octahedral stress corresponding to the yield point obtained from the twisting test was 38 percent greater than that obtained from the average of the yield points of tensile and compressive specimens of the material. Twisting tests of long strips of width/thickness ratios equal to 5 and 10 gave octahedral stresses corresponding to the yield point respectively 17 and 26 percent greater than for the average of the tensile and compressive tests. A twisting test of a long round specimen 0.59 in. in diameter, on the other hand, showed a corresponding octahedral stress 15 percent lower.

## 6. Conclusion

The stress-strain curve in shear up to strains of the order of 0.01 can be obtained for isotropic flat sheet from measurements of deflection or of extreme fiber bending strain in the center portion of a twisted square plate, provided that a correction is made for the edge effect. The shear moduli obtained from the twisting test of a 0.13×1.25×1.25-in. square plate of 75S–T aluminum alloy agreed within 2 percent with the value calculated from the average of the tensile and compressive moduli and an accepted value of Poisson's ratio. The octahedral stress derived from the stress-strain curve in shear for the twisted plate agreed within about 3 percent with the octahedral stress derived from tensile and compressive tests of the same material except near the knee, where the systematic deviations were as high as 5 percent. Much greater deviations were found in exploratory tests of mild steel.

Unfortunately, the method is difficult to perform on sheet material because the specimen must be small in size. Alternative methods should be investigated. An examination of other methods indicates that the annulus of constant thickness method can be used for determining the stress-strain curve in shear, even in the presence of a large radial variation in shear stress. Preparations are under way for carrying out such tests at the National Bureau of Standards.

## 7. Appendix

### 7.1. Membrane stresses in elastic range

The membrane stresses in a twisted square plate can be estimated from the equations for the state of strain in a flat plate with large deflections. These are given by Love [17] as

$$\left.\begin{aligned} \epsilon_x &= \frac{\partial u}{\partial x}+\frac{1}{2}\left(\frac{\partial w}{\partial x}\right)^2 \\ \epsilon_y &= \frac{\partial v}{\partial y}+\frac{1}{2}\left(\frac{\partial w}{\partial y}\right)^2 \\ \gamma_{xy} &= \frac{\partial v}{\partial x}+\frac{\partial u}{\partial y}+\frac{\partial w}{\partial x}\frac{\partial w}{\partial y} \end{aligned}\right\}. \tag{33}$$

It is assumed that the plate of figure 2 is bent into an anticlastic surface so that the transverse deflection is given by

$$w=\frac{x^2-y^2}{2R}, \tag{34}$$

just as in the case of small deflections, eq (3).

The curvature is from (11)

$$\frac{1}{R}=\frac{2\epsilon_1}{h}. \tag{35}$$

The magnitude of the membrane strain depends on the displacements $u$, $v$ parallel to the $x$, $y$ axes as well as on $w$.

The displacement $u$ in the $x$-direction can be approximated by a polynomial of the form

$$u=\sum_{i,j} c_{ij}x^i y^j, \tag{36}$$

where $i$, $j$ are positive integers. The coefficients $c_{ij}$ of many of the terms in the series must be equal to zero in order to satisfy the following conditions of symmetry and antisymmetry in the plate, figure 2:

$$\left.\begin{aligned} u(x,y) &= u(x,-y) \\ u(x,y) &= -u(-x,y) \end{aligned}\right\}. \tag{37}$$

These conditions are satisfied if $i$, $j$ are confined to

$$\left.\begin{aligned} i &= 1,3,5\ldots \\ j &= 0,2,4\ldots \end{aligned}\right\}. \tag{38}$$

The displacement $v$ at the point $(y, x)$ must be equal to the displacement $u$ at the point $(x, y)$, so that

$$v=\sum_{i,j} c_{ij}y^i x^j. \tag{39}$$

Up to and including terms of the fifth power, the series (36) and (39) become

$$\left.\begin{aligned} u &= c_{10}x + c_{12}xy^2 + c_{30}x^3 + c_{14}xy^4 + c_{32}x^3y^2 + c_{50}x^5 \\ v &= c_{10}y + c_{12}x^2y + c_{30}y^3 + c_{14}x^4y + c_{32}x^2y^3 + c_{50}y^5 \end{aligned}\right\} \quad (40)$$

To satisfy the conditions that the membrane stresses $\sigma_{x'}$, $\tau_{x'y'}$ be zero along the edge

$$y = \frac{b}{\sqrt{2}} - x \quad (41)$$

of the plate, and that the strain energy stored in the form of membrane stress must be a minimum, the six unknowns $c_{10}$, $c_{12}$, $c_{30}$, $c_{14}$, $c_{32}$, and $c_{50}$ were determined as follows.

Equilibrium of forces on an element of the plate bounded by the edge and by planes $y$=const., $x$=const. shows that the membrane stresses along the edge are related to the membrane stresses $\sigma_x$, $\sigma_y$, $\tau_{xy}$ by

$$\left.\begin{aligned} \sigma_{x'} &= \frac{\sigma_x + \sigma_y}{2} + \tau_{xy} \\ \tau_{x'y'} &= \frac{\sigma_x - \sigma_y}{2} \end{aligned}\right\} \quad (42)$$

The stresses $\sigma_x$, $\sigma_y$, $\tau_{xy}$ must be adjusted to make $\sigma_{x'}$ and $\tau_{x'y'}$ in (42) equal to zero. The membrane stresses are related to the membrane strains $\epsilon_x$, $\epsilon_y$, $\gamma_{xy}$ by Hooke's Law

$$\left.\begin{aligned} \sigma_x &= \frac{E}{1-\nu^2}(\epsilon_x + \nu\epsilon_y), \quad \sigma_y = \frac{E}{1-\nu^2}(\epsilon_y + \nu\epsilon_x) \\ \tau_{xy} &= \frac{E}{2(1+\nu)}\gamma_{xy} \end{aligned}\right\} \quad (43)$$

where $E$, $\nu$ are Young's modulus and Poisson's ratio, respectively.

The membrane strains may be computed from the displacements, using eq (33). Carrying out the computations and using the following notation for convenience

$$\left.\begin{aligned} &\xi = \frac{x}{b}; \quad \eta = \frac{y}{b}; \quad \rho = \frac{b}{R} \\ &c_0 = c_{10}; \quad c_2 = c_{12}b^2; \quad c_3 = 3c_{30}b^2 + \frac{b^2}{2R^2} \\ &c_4 = c_{14}b^4; \quad c_5 = c_{50}b^4; \quad c_6 = c_{32}b^4 \end{aligned}\right\} \quad (44)$$

lead to

$$\left.\begin{aligned} \epsilon_x &= c_0 + c_2\eta^2 + c_3\xi^2 + c_4\eta^4 + 3c_6\xi^2\eta^2 + 5c_5\xi^4 \\ \epsilon_y &= c_0 + c_2\xi^2 + c_3\eta^2 + c_4\xi^4 + 3c_6\xi^2\eta^2 + 5c_5\eta^4 \\ \gamma_{xy} &= [4c_2 - \rho^2 + (4c_4 + 2c_6)(\xi^2 + \eta^2)]\xi\eta \end{aligned}\right\} \quad (45)$$

Substituting (45) in (43) and (43), in (42) and using the notation

$$\alpha = \frac{1-\nu}{1+\nu} \quad (46)$$

gives, for the normal and shearing stresses acting on the edges,

$$\left.\begin{aligned} \sigma_{x'} &= \frac{E}{2(1-\nu)}\{2c_0 + (c_2 + c_3)(\xi^2 + \eta^2) + \\ &\quad (c_4 + 5c_5)(\xi^4 + \eta^4) + 6c_6\xi^2\eta^2 + \alpha\xi\eta[4c_2 - \rho^2 + \\ &\quad (4c_4 + 2c_6)(\xi^2 + \eta^2)]\} \\ \tau_{x'y'} &= \frac{E}{2(1+\nu)}(\xi^2 - \eta^2)[(c_3 - c_2) + (5c_5 - c_6)(\xi^2 + \eta^2)] \end{aligned}\right\} \quad (47)$$

The shearing stresses $\tau_{x'y'}$ will be zero for all points $\xi$, $\eta$ along the edge of the plate only if the expression in the square brackets is equal to zero. This requires that

$$c_3 = c_2; \quad 5c_5 = c_6. \quad (48)$$

The normal stress $\sigma_{x'}$ along the edge can be expressed as a polynomial of the fourth order in $\xi$ by noting from (41) that, for points along the edge of the plate,

$$\eta = \frac{1}{\sqrt{2}} - \xi. \quad (49)$$

Collecting terms by powers of $\xi$ and substituting (48) leads to

$$\begin{aligned} \frac{2(1-\nu)}{E}\sigma_{x'} = {} & 2c_0 + c_3 + \frac{5}{2}c_5 + \frac{\xi}{\sqrt{2}}[-4c_3 - 20c_5 + \\ & \alpha(4c_3 + 10c_5 + c_6 - \rho^2)] + \xi^2[4c_3 + 30c_5 + \\ & 3c_6 + \alpha(-4c_3 - 30c_5 - 3c_6 + \rho^2)] + \\ & \sqrt{2}\xi^3[-20c_5 - 6c_6 + \alpha(4c_6 + 40c_5)] + \\ & \xi^4[20c_5 + 6c_6 + \alpha(-4c_6 - 40c_5)] = 0 \end{aligned} \quad (50)$$

The stress $\sigma_{x'}$ will be zero for all points $\xi$ along the edge only if each one of the five brackets on the right is equal to zero. Examination of these brackets shows that only three of them are independent of each other. One may solve the resulting three equations for any three of the coefficients $c_0$, $c_3$, $c_5$, $c_6$ in terms of the remaining coefficient.

Solving in terms of $c_0$ and assuming for Poisson's ratio the typical value $\nu$=1/3 and hence from (46) $\alpha$=1/2, one obtains from (50)

$$c_3 = -3c_0 + \rho^2/8; \quad c_5 = \frac{2}{5}c_0 - \frac{1}{20}\rho^2; \quad c_6 = 0. \quad (51)$$

Substitution of (51) and (48) in (45) shows that the

strains reduce to

$$\left.\begin{aligned}\epsilon_x=\epsilon_y&=c_0+c_3(\xi^2+\eta^2)+5c_5(\xi^4+\eta^4)\\ \gamma_{xy}&=[4c_3-\rho^2+20c_5(\xi^2+\eta^2)]\xi\eta\end{aligned}\right\} \tag{52}$$

It remains to compute the constant $c_0$ by minimizing the membrane strain energy stored in the plate. The membrane strain energy per unit volume, $V_0=\frac{1}{2}(\sigma_x\epsilon_x+\sigma_y\epsilon_y+\tau_{xy}\gamma_{xy})$ is with (43) and (52), assuming $\nu=1/3$

$$V_0=\frac{3}{16}E(8\epsilon_x^2+\gamma_{xy}^2). \tag{53}$$

The elastic membrane strain energy $V_m$ stored in the plate is obtained by integrating (53) over the volume of the plate

$$\begin{aligned}V_m&=4\int_{x=0}^{b/\sqrt{2}}\int_{y=0}^{(b/\sqrt{2})-x}V_0h\,dy\,dx\\ &=4hb^2\int_{\xi=0}^{1/\sqrt{2}}\int_{\eta=0}^{(1/\sqrt{2})-\xi}V_0\,d\eta\,d\xi.\end{aligned} \tag{54}$$

Substitution of (52) in (53), of the resulting expression in (54), and integration leads to

$$\begin{aligned}V_m=\frac{3Ehb^2}{4}\Big[&2c_0^2+\frac{2}{3}c_0c_3+\frac{1}{15}(c_3^2+10c_0c_5)+\\ &\frac{1}{1440}(32c_3^2-8c_3\rho^2+\rho^4)+\frac{1}{168}(36c_3c_5-c_5\rho^2)+\frac{13}{84}c_5^2\Big]\end{aligned} \tag{55}$$

The membrane energy $V_m$ is minimized by computing

$$\frac{\partial V_m}{\partial c_0}=0, \tag{56}$$

and substituting (51) to obtain an equation having $c_0$ as the only unknown. Solving for $c_0$ gives

$$c_0=-\frac{3}{146}\rho_2=-0.0205\rho^2. \tag{57}$$

The membrane strains and stresses throughout the plate are then obtained by substituting (57) in (51) and the resulting constants in eq (47) and (52) and the latter then in (43).

The stresses can be plotted in dimensionless form by multiplying them by $h^2/b^2\gamma_1\tau_1$, where $b/h$ is the width/thickness ratio for the plate and $\gamma_1,\tau_1$ are the extreme fiber shearing strain and stress due to bending. These are from (6), (7), and (11)

$$\gamma_1=\frac{h}{R},\quad \tau_1=G\frac{h}{R}. \tag{58}$$

The results of such computations are plotted in figure 11 as solid lines. The plots show that the membrane stress at the center of the plate consists of a uniform compressive stress

$$\sigma_{x'}=\sigma_{y'}=0.082\frac{b^2}{h^2}\gamma_1\tau_1. \tag{59}$$

The membrane stresses are largest at the center of the edge of the plate. The membrane normal stresses at this point are

$$\sigma_{y'}=0.136\frac{b^2}{h^2}\gamma_1\tau_1;\quad \sigma_{x'}=0. \tag{60}$$

A check on this solution seemed advisable since it did not satisfy the conditions of equilibrium at all points of the plate; it would be necessary to apply a system of body forces per unit volume with components $X$, $Y$ in the $x$, $y$ directions in order to maintain equilibrium in all plate elements. The equilibrium conditions would be satisfied more nearly if $c_0$ is chosen to minimize the average value of $X^2+Y^2$ for the entire plate instead of minimizing the strain energy. This leads to

$$c_0=-0.0187\rho^2, \tag{61}$$

which is about 10 percent below the previous value. The membrane stresses corresponding to this value of $c_0$ are shown as dotted lines in figure 11. They differ less than 10 percent from the stresses previously obtained.

A second check on the adequacy of the theory was obtained by computing from it the nonlinear relation between load $P$ and extreme fiber bending strain $\epsilon_1$ and comparing it with the experimental values given in figure 6. The relation between $P$ and $\epsilon_1$ for the elastic range was obtained by equating the increments of work done by the corner loads $dW_P$ and the

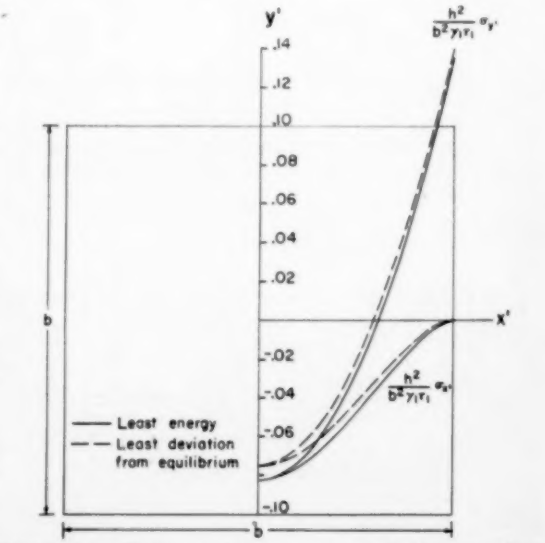


FIGURE 11. *Elastic membrane stresses in twisted square plate.*

resulting increase in strain energy $dV$ consisting of the increment $dV_b$ stored in the form of bending strains and the increment $dV_m$ stored in the form of membrane strains

$$dW_P = dV_b + dV_m. \tag{62}$$

Each one of the three terms in this equation can be regarded as a function of the curvature ratio $\rho = b/R$. It can be shown easily that the work done by the corner forces $P$ corresponding to an increment of curvature ratio $d\rho$ is

$$dW_P = Pbd\rho. \tag{63}$$

The increase in bending strain energy can be derived from the bending strain, eq (4) as

$$dV_b = \frac{Eh^3}{8}\rho d\rho. \tag{64}$$

The increment in membrane strain energy is obtained from (55) after substituting (57) and (51). This leads to

$$dV_m = 0.001146\, Ehb^2\rho^3 d\rho. \tag{65}$$

Substituting (63) to (65) in (62), solving for $P$, and replacing $\rho$ by

$$\rho = \frac{b}{R} = 2\frac{b}{h}\epsilon_1, \tag{66}$$

gives the desired relation for $P(\epsilon_1)$,

$$P = \frac{Eh^2}{4}\epsilon_1\left[1 + 0.03666\left(\frac{b}{h}\right)^4\epsilon_1^2\right]. \tag{67}$$

This reduces to eq (9) for small values of $\epsilon_1$ with $\nu = 1/3$. Substitution of $E = 10.4 \times 10^6$ lb/in.$^2$, $h = 0.126$ in., $b = 7.2$ in. for the plate of figure 6 leads to the solid line shown in that figure. The observed points come close to this curve, thereby providing a second check on the adequacy of this approximate theory for computing membrane stresses in the elastic range.

## 8. References


[1] Ambrose H. Stang, Walter Ramberg, and Goldie Back, Torsion tests of tubes, NACA Report 601, p. 4–5, (1937).

[2] E. G. Coker and L. N. G. Filon, Photo-elasticity, p. 603 (Cambridge University Press, London, 1931).

[3] F. Bollenrath, Ausbeulerscheinungen an ebenen auf Schub beanspruchten Platten, Dissertation, Technische Hochschule, Aachen (1928).

[4] A. Nadai, Die Formaenderungen und die Spannungen von rechteckigen elastischen Platten, Forsch Gebiete Ingenieurw, Heft 170, 171, p. 16–28 (Springer, Berlin, 1915).

[5] H. W. March, E. W. Kuenzi and W. J. Kommers, Method of measuring the shearing moduli in wood, Forest Products Laboratory War Series Progress Report 1301 (June 1942).

[6] A. Nadai, Theory of flow and fracture of solids, **1** p. 359 (McGraw-Hill Book Co., Inc., New York, N. Y., 1950).

[7] S. Timoshenko and J. N. Goodier, Theory of elasticity, p. 52 (McGraw-Hill Book Co., Inc., New York, N. Y., 1951).

[8] S. Timoshenko and J. N. Goodier, Theory of elasticity, p. 102–106 (McGraw-Hill Book Co., Inc., New York, N. Y., 1951).

[9] Lord Kelvin and P. G. Tait, Natural philosophy, part 2, **2**, 203 (Cambridge University Press, London, 1895).

[10] S. Timoshenko and J. N. Goodier, Theory of elasticity p. 275–278 (McGraw Hill Book Co., Inc., New York, N. Y., 1951).

[11] Lord Kelvin and P. G. Tait, Natural philosophy, part 2, **2**, 267–268 (Cambridge University Press, London, 1895).

[12] A. Nadai, Theory of flow and fracture of solids, **1**, p. 499 (McGraw-Hill Book Co., Inc., New York, N. Y., 1950).

[13] A. E. McPherson, Device for measuring principal curvatures and principal strains on a nearly plane surface, NACA TN1137 (February 1947).

[14] James A. Miller, Stress-strain and elongation graphs for aluminum-alloy 758–T6 sheet, NACA TN2085 (April 1950).

[15] William R. Campbell, Performance tests of wire strain gages, IV–Axial and transverse sensitivities, NACA TN 1042 (June 1946).

[16] A. Nadai, Theory of flow and fracture of solids, **1**, p. 103, 115 (McGraw-Hill Book Co., Inc., New York, N. Y., 1950).

[17] A. E. H. Love, The mathematical theory of elasticity, 4th ed., p. 557 (Cambridge University Press, London, 1934).


WASHINGTON, June 1951.

Journal of Research of the National Bureau of Standards Vol. 50, No. 2, February 1953 Research Paper 2398

# Stress-Strain Relation in Shear From Twisting Test of Annulus[1, 2]

Walter Ramberg and James A. Miller

It is shown that the stress-strain relation in shear of isotropic thin sheet can be determined from a test of an annular specimen. The annulus must be clamped uniformly along the inner and the outer edge, and the relative twist of two circles concentric with the edges must be measured. The shear strain at the inner circle can be computed from the shear strain at the outer circle and the slope of the torque-twist curve. Tests were made on 0.032-inch aluminum alloy 758–T6 sheet well beyond the elastic range to a shearing stress of 48,000 lb/in.$^2$ EPON adhesive VI was used to bond the sheet to a clamping ring at the outer edge of the annulus and between the sheet and the end of a cylinder through which the torque was applied.

## 1. Introduction

The stress-strain relation in shear of thin sheet metal is of practical importance for estimating the strength of shear webs. It is of theoretical importance in studying the plastic behavior of metals under combined stress.

Many methods have been suggested for determining the stress-strain curve in shear of thin sheet [1], [3] and at least two of them have been tried. Good results have been obtained so far only from twisting tests of square plates of aluminum alloy [1]. Unfortunately the twisting test of a square plate makes severe demands on the skill and patience of the test engineer. Furthermore, the specimen becomes too small for precision in the measurement of strain and in the application of the twisting loads for sheet less than 0.1 in. thick. Hence it seemed desirable to try out some of the other methods that have been proposed. One of the most promising among these is the twisting test of an annulus of constant thickness. This method was accordingly investigated at the National Bureau of Standards as part of a program supported by the Office of Naval Research, United States Department of the Navy.

## 2. Theory of Twisting Test of Annulus of Constant Thickness

Consider an annulus of constant thickness $h$, twisted by a torque $M_t$, which applies a constant shearing force per unit length along the inner edge $r=a$, figure 1, and along the outer edge $r=b$. If the material is isotropic, the shearing stress at any radius $r$ is given by

$$\tau=\frac{M_t}{2\pi r^2 h}. \tag{1}$$

The shearing strain at any point can be derived from the radial displacement $u$ and the circumferential displacement $v$ by substitution in the equation for plane strain in polar coordinates $r$, $\theta$ [2, p. 66]:

$$\gamma=\frac{\partial v}{\partial r}+\frac{\partial u}{r\partial\theta}-\frac{v}{r}. \tag{2}$$

In an isotropic annulus the displacements $u$, $v$ caused by twisting are independent of $\theta$, so that (2) reduces to

$$\gamma=\frac{dv}{dr}-\frac{v}{r}=r\frac{d}{dr}\left(\frac{v}{r}\right). \tag{3}$$

Integration of this expression leads to a formula for the circumferential displacement $\delta$ of a point on an outer circle with radius $r_2$ relative to a platform resting on an inner circle with radius $r_1$, figure 1. We note from figure 1 that this displacement is

$$\delta=v_2-v_1\frac{r_2}{r_1}=r_2\left(\frac{v_2}{r_2}-\frac{v_1}{r_1}\right) \tag{4}$$

Dividing $\gamma$ by $r$ in (3) and integrating gives

$$\int_{r_1}^{r_2}\frac{\gamma}{r}dr=\frac{v_2}{r_2}-\frac{v_1}{r_1}, \tag{5}$$

so that

$$\frac{\delta}{r_2}=\int_{r_1}^{r_2}\frac{\gamma}{r}dr. \tag{6}$$

From this an equation for the shearing strain $\gamma_1$ at the circle $r=r_1$ can be obtained as follows. We can replace $r$ as the independent variable in the integral by $\tau$, by taking the logarithms of the two sides in eq (1)

$$\log\tau=\log\frac{M_t}{2\pi h}-2\log r, \tag{7}$$

and then differentiating for a given plate under given twisting moment ($M_t$, $h$ constant):

$$\frac{d\tau}{\tau}=-2\frac{dr}{r}. \tag{8}$$

[1] This paper is based on work sponsored by the Mechanics Branch, Office of Naval Research, U. S. Department of the Navy.
[2] Presented at the Eighth International Congress on Theoretical and Applied Mechanics in Istanbul, Turkey, August 20-28, 1952.
[3] Figures in brackets indicate the literature references at the end of this paper.

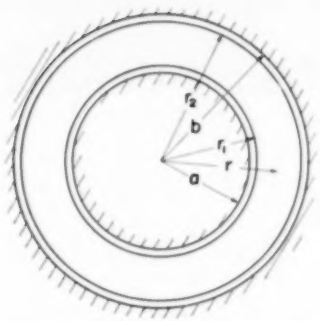


FIGURE 1. *Diagrammatic sketch of annulus.*

*a*, inner radius; *b*, outer radius; $r_1$, radius of inner gage circle; $r_2$, radius of outer gage circle.

Inserting (8) in (6) gives

$$\delta = -\frac{r_2}{2}\int_{\tau_1}^{\tau_2}\frac{\gamma}{\tau}\,d\tau, \tag{9}$$

where $\tau_1$, $\tau_2$ are the shearing stresses at radii $r_1$, $r_2$, respectively. Differentiating with respect to $M_t$ gives [3, p. 29]

$$\frac{d\delta}{dM_t} = -\frac{r_2}{2}\left[\int_{\tau_1}^{\tau_2}\frac{d}{dM_t}\left(\frac{\gamma}{\tau}\right)d\tau + \frac{d\tau_2}{dM_t}\left(\frac{\gamma_2}{\tau_2}\right) - \frac{d\tau_1}{dM_t}\left(\frac{\gamma_1}{\tau_1}\right)\right]. \tag{10}$$

Since the ratio of $\gamma$ to $\tau$ does not depend on the parameter $M_t$, $d(\gamma/\tau)/dM_t = 0$, and consequently the integral on the right-hand side is equal to zero. The derivatives $d\tau_2/dM_t$ and $d\tau_1/dM_t$ are obtained directly from (1), noting that $r$ is equal to $r_1$, $r_2$, respectively. This leads to

$$\frac{d\delta}{dM_t} = \frac{r_2}{4\pi h}\left(\frac{\gamma_1}{\tau_1 r_1^2} - \frac{\gamma_2}{\tau_2 r_2^2}\right). \tag{11}$$

This equation can be solved for the shearing strain $\gamma_1$ at the inner circle

$$\gamma_1 = \gamma_2 + \frac{2}{r_2}M_t\frac{d\delta}{dM_t}. \tag{12}$$

Equation (12) makes possible a step-by-step construction of the stress-strain curve in shear, provided that the measurements are started within the elastic range. The shear modulus $G$ may be determined from a single measurement of $\delta$ in that range by noting that inside the elastic range

$$\frac{\gamma_2}{\tau_2} = \frac{\gamma_1}{\tau_1} = \frac{1}{G}. \tag{13}$$

Inserting in (11) and solving for $G$:

$$G = \frac{r_2}{4\pi h}\left(\frac{1}{r_1^2} - \frac{1}{r_2^2}\right)\Big/\frac{d\delta}{dM_t}. \tag{14}$$

## 3. Procedure for Twisting Test

### 3.1. Dimensions of Specimen

The dimensions of the specimen must be chosen to satisfy several opposing requirements.

The required external torque must be readily attainable. If $M_t$ is the maximum torque that can be applied and $\tau_a$ the shearing stress at the inner edge $r=a$ of the annulus, we have from (1)

$$a = \sqrt{\frac{M_t}{2\pi\tau_a h}}. \tag{15}$$

The torque must be applied uniformly to the edges of the specimen. This makes it inadvisable to use clamps consisting of heavy clamping rings held together by individual bolts. In such a clamping arrangement one would expect higher shearing stresses to be transmitted near the bolts, where the clamping pressures are high, than at locations relatively far from the bolts. It would be better to cut a circular disk with a radius well in excess of *b* from the material and then apply the torque to one or both faces of this disk through adhesive layers, as indicated in figure 2. The torque $M_t$ is then limited by the shear stress $\tau_a$ transmitted through the adhesive at the inner edge $r=a$ of the annulus.

The magnitude of $\tau_a$ can be computed from the torque $M_t$ on the assumption that each adhesive layer behaves like an elastic lamination of constant thickness connecting two rigid bodies that are rotated relative to each other. The shearing stress is then proportional to the distance $r$ from the axis of twist. If there is only one layer, the torque is equal to

$$M_t = \int_0^a r\,2\pi r\tau\,dr = 2\pi\int_0^a r^2\tau_a\frac{r}{a}\,dr = \frac{\pi}{2}a^3\tau_a. \tag{16}$$

The torque $M_t$ produces a shearing stress $\tau_a$ at the inner radius of the annulus given by (1)

$$\tau_a = \frac{M_t}{2\pi a^2 h}. \tag{17}$$

With (16) this leads to the condition

$$2\pi a^2 h\tau_a \le \frac{\pi}{2}a^3\tau_a, \tag{18}$$

or

$$a/h \ge 4\tau_a/\tau_a. \tag{19}$$

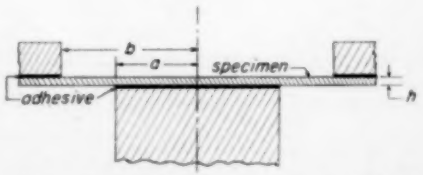


FIGURE 2. *Cross-sectional view of annulus and grips.*

The sheet in the annulus must be stable against buckling into a pattern of shear wrinkles up to the highest torque applied. The authors have not found a solution for the buckling stress of an annulus. However, an approximation to this buckling stress is obtained from Southwell and Skan's solution for the infinitely long elastic strip with clamped edges [4]; with $\nu=0.3$ this reduces to

$$\tau_{cr}=21.1\frac{Gh^2}{(b-a)^2}, \tag{20}$$

The modulus of elasticity in shear, $G$, must be replaced by a reduced modulus $\overline{G}$, where $\overline{G}$ will be somewhere between $G$ and the tangent modulus at $\tau_{cr}$, since buckling must not take place until the material at $r=r_1$ has been stressed well into the plastic range. This leads to the condition

$$\overline{\tau}<21.1\frac{\overline{G}h^2}{(b-a)^2}, \tag{21}$$

where $\overline{\tau}$ denotes the shearing stress at the mean radius $c=(a+b)/2$, of the annulus. Condition (21) sets an upper limit to the width $(b-a)$.

A lower limit is set by the condition that $(b-a)$ must be sufficient to accomodate the device for measuring relative displacement.

Another condition that must be satisfied is that the tensile strain in a radial direction is negligible. From figure 3 we see that this radial strain is in first approximation

$$\epsilon_r=\frac{\overline{A'B'}-\overline{AB}}{\overline{AB}}=\frac{\overline{A'B'}}{\overline{AB}}-1=\frac{\sqrt{(b-a)^2+(v_b-v_a)^2}}{(b-a)}-1 \tag{22}$$

or with

$$\frac{v_b-v_a}{b-a}=\overline{\gamma} \tag{23}$$

$$\epsilon_r=\sqrt{1+\overline{\gamma}^2}-1=\frac{\overline{\gamma}^2}{2}-\cdots. \tag{24}$$

This must be small compared to the normal strain of the order $\overline{\gamma}/2$ along lines at 45° to the radial direction, that is,

$$\frac{\epsilon_r}{\overline{\gamma}/2}\ll 1. \tag{25}$$

From (24)

$$\frac{\epsilon_r}{\overline{\gamma}/2}=\overline{\gamma}-\cdots, \tag{26}$$

which is small compared to one in the range in which we are interested.

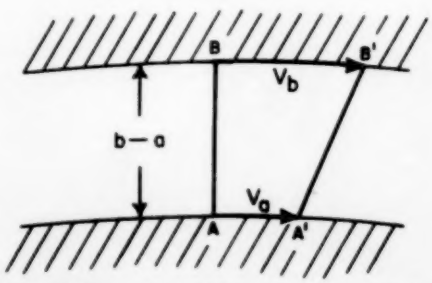


FIGURE 3. *Diagramatic sketch for estimating radial strain due to relative circumferential displacement of inner and outer edges of the annulus.*

Let us apply these equations to the specific case of high-strength aluminum-alloy sheet with a yield strength in shear, $\tau_1$, of the order of 45,000 lb/in.$^2$ (tensile yield strength about 78,000 lb/in.$^2$) to be tested in a torsion machine with a capacity of 27,000 lb-in. Let us assume that a bonding material with a shear strength $\tau_a=4{,}500$ lb/in.$^2$ can be used for applying the torque to the specimen, and that a displacement measuring device with a width of 1 in. can be constructed to measure $\delta$, so that $b-a\geq 1$ in. Let us assume also that the stress at the inner edge exceeds the yield strength in shear by 20 percent $\tau_a=1.2\tau_1=54{,}000$ lb/in.$^2$ Substituting these quantities in (17) and (19) gives $a\leq 0.282/\sqrt{h}$ and $a\geq 48h$, respectively, or, $48h\leq a\leq 0.282/\sqrt{h}$. We obtain an upper limit for the thickness $h$, $h\leq 0.0326$ in., by going to the case in which $a$ is equal to its lower and its upper limit. The corresponding radius of the inner clamp is $a=0.282/\sqrt{0.0326}=1.56$ in. The outer and the mean radius become $b=a+1=2.56$ in; $c=2.06$ in. The shearing stress at the mean radius is from (1) $\overline{\tau}=\tau_a(a^2/c^2)=31{,}000$ lb/in.$^2$

This calculation indicates that the annulus must have a thickness of less than 0.0326 in. for high-strength aluminum-alloy sheet with a yield strength in shear of the order of 45,000 lb/in.$^2$

A lower limit for the thickness may be obtained by solving (21) for $h$. Since much of the material in the annulus will be in the elastic range, it seems reasonable to assume 3,000,000 lb/in.$^2$ (about three-fourths the modulus of elasticity in shear) as an average value of $\overline{G}$. Then from (21)

$$h>(b-a)\sqrt{\overline{\tau}/21.1\overline{G}}=0.0221 \text{ in.}$$

We conclude that the thickness should be between 0.022 and 0.033 in. for this alloy tested under the assumed conditions.

### 3.2. Method of Applying Torque

Advice regarding the bonding medium for transmitting torque to the specimen was obtained from experts in the field, and it was decided to try cements of the Epoxy type upon recommendation of N. J. DeLollis of the National Bureau of Standards and D. M. Alstadt of the Lord Manufacturing Co., Erie, Pa.

The shear strength of the cement was determined from torsion tests of specimens made by joining in a butt joint two pieces of aluminum-alloy rod 1.5 in. in diameter. Similar specimens were made from aluminum-alloy tubing 1.5 in. in diameter and 0.094 in. thick. The surfaces were cleaned with a degreasing solvent and Deoxidine. The bonding

medium was EPON adhesive VI with 6 parts by weight of accelerator A to 100 parts of the adhesive. As soon as the adhesive was applied to one piece, the two pieces were pressed together until the thickness of adhesive was from 0.005 to 0.01 in. The pieces were held in position by clamps while the adhesive was cured for 45 min. at from 200° to 220° F. The excess adhesive was removed from the outer surface of each specimen.

The maximum shear strength $\tau_s$, computed from these tests by substituting the torque at failure in (16) for the rod and in an analogous equation for the tube, was between 6,200 and 6,800 lb/in.$^2$ for the tubular specimens and between 6,000 and 6,700 lb/in.$^2$ for the cylindrical specimens.

Attempts to develop shear strength of this order in transmitting torque to a specimen of 0.032-in. aluminum-alloy sheet bonded to a 3-in. aluminum-alloy cylinder were unsuccessful. This may have been due in part to stress concentration in the adhesive at the inner edge of the annulus. This stress concentration was relieved somewhat by machining a circumferential notch in the cylinder 0.01 in. from the bond and by bonding disks (A and B, fig. 4) of 0.020-in. aluminum-alloy sheet to the specimen.

The radii of A and B were 0.06 and 0.03 in., respectively, greater than the radius of cylinder C. The cylinder, the disks, the specimen S, and the ring R were held coaxially by the pin P and the jig J while the adhesive was being pressed out to a thickness of about 0.01 in. and during the curing of the adhesive. The jig was also used for locating the bolt holes in the ring and for holding the ring while it was being machined. The bond between the cylinder and disk B did not fail until the value of $\tau_s$ reached 4,670 lb/in.$^2$ No difficulty was experienced with the bond between the specimen, which had a diameter of 6.5 in., and ring R, the inside diameter of which was 5 in.

Two torsion-testing machines were available for the tests, a Riehle testing machine of 60,000-lb-in. capacity and an Amsler testing machine of 150-kg-m (13,000-lb-in.) capacity. In the Riehle machine the torque was transmitted to the weighing beam through a series of knife edges and linkages, which provided a very flexible mounting for one head of the machine. The specimen was first set up in this machine because of its greater capacity but was moved to the Amsler machine when it was found that good alinement could not be maintained. The alinement of the weighing head of the Amsler machine is maintained by ball bearings. The 13,000-lb-in. capacity, measured by rotation of the pendulum, was insufficient for the specimen. To increase the capacity, the weighing system was changed to the simple lever and scale type, utilizing the pendulum only for attaching the arm A, figure 5. The effective length of the lever was 48 in., and the scale was the spring balance B, having a capacity of 600 lb. During the test the pendulum was maintained in the zero position so that its moment would not affect the torque measurement. The specimen assembly was mounted in the testing machine by bolting the ring to the plate H, figure 6, attached to the dynamometer head of the machine. The holes in the plate had been located by the jig J, shown in figure 4. The cylinder was centered in the loading head of the machine.

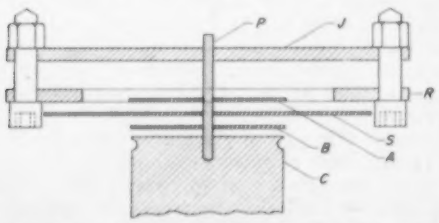


FIGURE 4. *Expanded cross-sectional view of specimen S, disks A and B, cylinder C and ring R, positioned by jig J, and centered with pin P for bonding.*

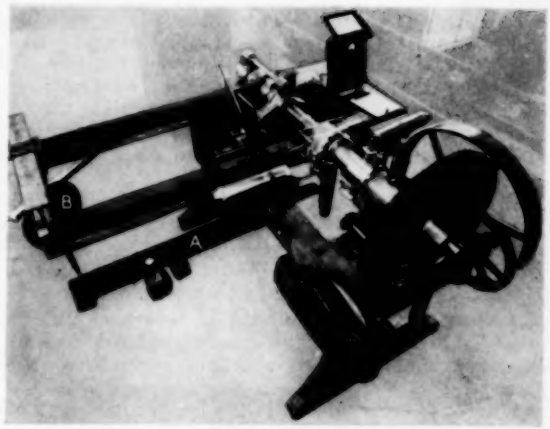


FIGURE 5. *Modified Amsler torsion machine.*

### 3.3. Method of Measuring Deformation

The device for measuring deformation of the specimen is shown in position in figure 7. The

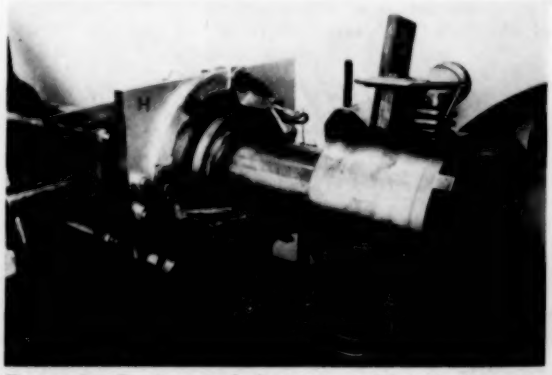


FIGURE 6. *Specimen ready for test in modified Amsler torsion machine.*

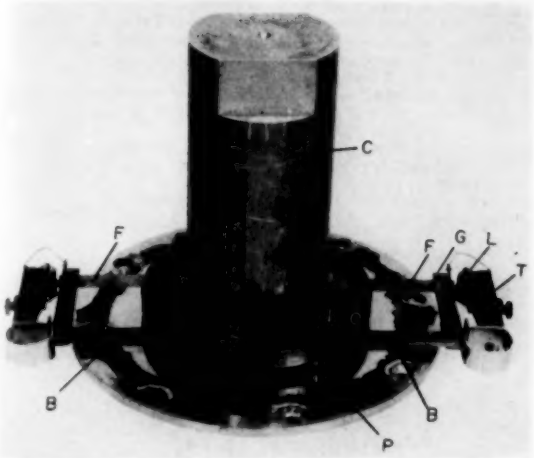


FIGURE 7. *Gage for measuring relative circumferential displacement.*

purpose of the device is to measure the relative rotation between two circles concentric with the axis of the cylinder C having radii $r_2$ and $r_1$ of 2.375 and 1.625 in., respectively. These circles are defined by conical points, such as P, 120° apart, mounted on the rings O and I, respectively. The relative rotation is measured by measuring the relative tangential motion between the two rings. To increase the sensitivity and reduce any errors due to bending of the specimen, the motion between the ends of the arms B and F is measured. Due account is taken of the radius at which the motion is measured. Each arm B is attached rigidly to the outer ring O and provides physical support to the body of a Tuckerman optical strain gage T. Each arm F, attached to the inner ring I, is flexible in the direction of the axis of the specimen and rigid in the direction of rotation. The rotating lozenge L of each gage is held against the outer end of an arm F by a pair of hairpin springs, one attached to each end of a rod through a hole in F and to a knob on each side of the gage. Guides G were rigidly attached to each arm B to limit the motion of the end of arm F to a plane perpendicular to the axis of the gage lozenge. The circumferential displacement $\delta$ of the circle with radius $r_1$ with respect to the circle with radius $r_2$ is given by

$$\delta = \epsilon \frac{r_2}{r_L},$$

where $\epsilon$ is the average displacement measured by the gages, and $r_L$ is the average of the radii to the points of contact of gage lozenges with the arms F.

## 4. Results

A disk of 0.032-in. 75S–T6 aluminum-alloy sheet was prepared and tested in shear as described above.

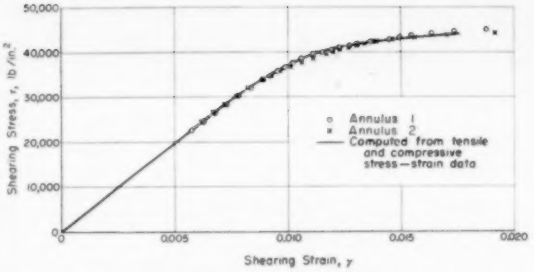


FIGURE 8. *Stress-strain curve in shear for a sheet of 75S–T6 aluminum alloy 0.032 in. thick.*

The test portion of the disk consisted of an annulus with inner and outer radii of 1.56 and 2.5 in., respectively. The test was carried to a shearing stress of 48,000 lb/in.$^2$ and a shearing strain of more than 0.05 at the inner gage ring before the adhesive at the inner edge of the annulus broke at a shear stress in the adhesive, as computed from (16), of 4,670 lb/in.$^2$. A second annulus reached a shearing stress of over 45,000 lb/in.$^2$. The data for both annuli up to a strain of about 0.019 are plotted in figure 8, together with a stress-strain curve in shear computed from an average stress-strain curve obtained from tests of tensile and compressive specimens from the same sheet. This curve was computed, in accordance with octahedral shear theory [5] from

$$\tau = \sigma/\sqrt{3} \qquad \text{and} \qquad \gamma = \sqrt{3}\left(\epsilon - \frac{17}{150}\frac{\sigma}{E}\right),$$

where $\sigma$ is the average of the stresses corresponding to the strain $\epsilon$ obtained in tensile and compression tests of specimens in the direction of rolling and across the direction of rolling of the sheet, and $E$ is the average of the moduli of elasticity in tension and compression. The shear data are in good agreement with the derived curve. The modulus of elasticity in shear for each specimen differed by less than 1 percent from that computed from $E$ and the nominal value of Poisson's ratio (0.33) for this alloy.

## 5. Conclusions

The twisting test of an annulus appears feasible for determining the stress-strain relation in shear of isotropic sheet metal in thicknesses below those which can be tested by twisting a square plate of the material. Special precautions must be taken to obtain a good bond for transmitting the shearing stresses to the specimen and to have good alinement between the two heads of the torsion-testing machine.

Using this method, the stress-strain curve in shear was determined for 0.032-in. aluminum alloy 75S–T6 sheet up to a strain of 0.05, which is far beyond the elastic range. The stress-strain curve thus obtained was in good agreement with one derived from the stress-strain curve of the same material in tension and compression, on the assumption that the octahedral shear stress in the metal was a function of the octahedral shear strain only.

The authors acknowledge the assistance of members of the Engineering Mechanics Section, in particular that of A. E. McPherson, D. F. Hoeschele, Jr., H. L. Byers, Jr., and R. H. Harwell, Jr.

## 6. References

[1] Walter Ramberg and James A. Miller, Twisted square plate method and other methods for determining the shear stress-strain relation of flat sheet, J. Research NBS **50,** (1953) RP2397.

[2] S. Timoshenko and J. N. Goodier, Theory of elasticit (McGraw-Hill Book Co., Inc., New York, N. Y., 1951)

[3] Philipp Frank and Richard von Mises, Die Differential und Integralgleichungen der Mechanik und Physi (Vieweg, Braunschweig, 1930).

[4] R. B. Southwell and S. W. Skan, On the stability unde shearing forces of a flat elastic strip, Proc. Roy. Soc London **105,** 582–607 (1924).

[5] A. Nadai, Theory of flow and fracture of solids, **1,** 103 115 (McGraw-Hill Book Co., Inc., New York, N. Y. 1950).

Washington, July 17, 1952.